Gas phase photocatalytic water splitting in silicon based µ-reactors

Dionigi, Fabio; Chorkendorff, Ib; Dahl, Søren; Vesborg, Peter Christian Kjærgaard

Publication date:
2012

Document Version
Publisher's PDF, also known as Version of record

Center for Individual Nanoparticle Functionality

DTU

Gas phase photocatalytic water splitting in silicon based μ-reactors

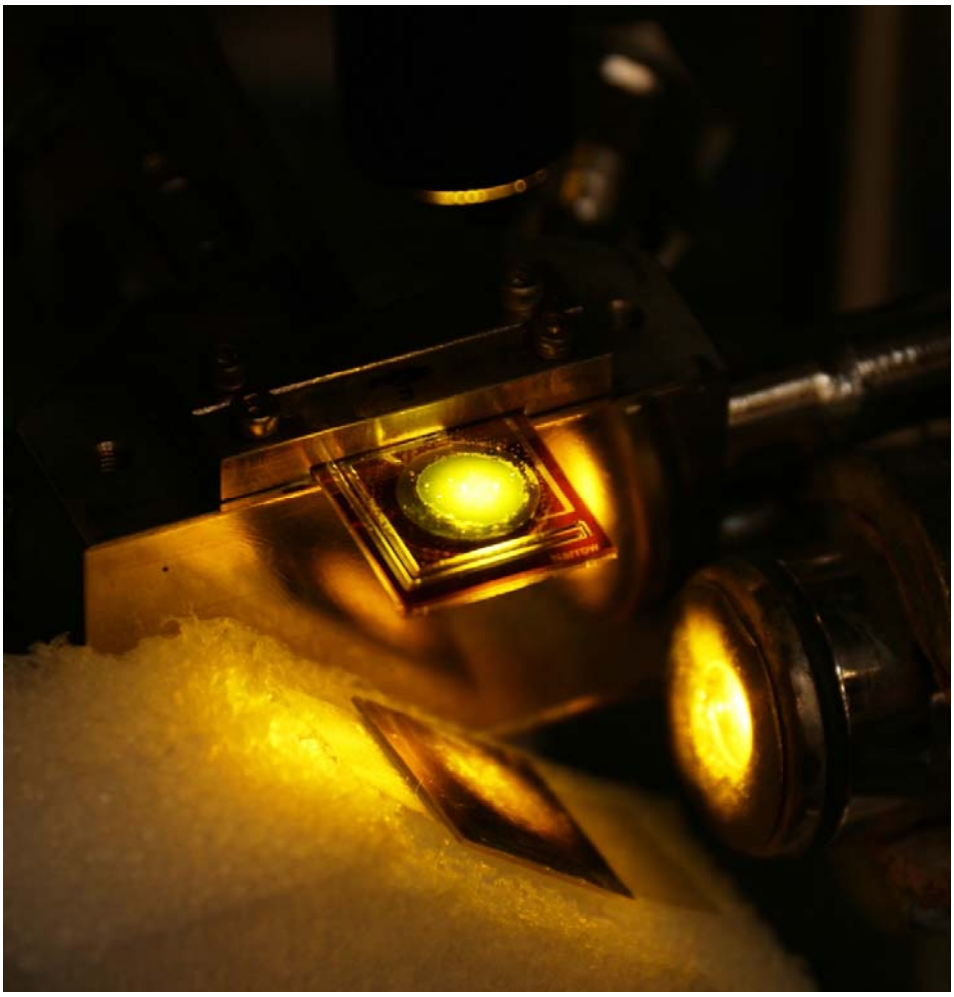

Fabio Dionigi
Center for Individual Nanoparticle Functionality
Catalysis for Sustainable Energy
Technical University of Denmark

Gas phase photocatalytic water splitting in silicon based μ-reactors

Ph.D. Dissertation by

Fabio Dionigi

October 2012

Center for Individual Nanoparticle Functionality

Technical University of Denmark

Front page picture:
Photograph of a transparent Pyrex μ-reactor mounted in the setup for photocatalytic experiments. A Xe-lamp equipped with a 515 nm cutoff filter illuminates from the top the reactor loaded with TiO_2. Part of the light is transmitted to the 45˚ tilted silver mirror below the reactor and reflected to the detector on the right. Photograph by M.G. Nielsen.

Preface and Acknowledgements

This thesis is submitted in candidacy for the Ph.D. degree from the Technical University of Denmark (DTU). The work presented has been carried out from November 2009 to October 2012 at the Center for Individual Nanoparticle Functionality (CINF) in the Department of Physics under the supervision of Professor Ib Chorkendorff, Professor Søren Dahl and Assistant Professor Peter C. K. Vesborg. CINF is funded by The Danish National Research Foundation which is acknowledged for their support.
My PhD project is part of the "Catalysis for Sustainable Energy program" (CASE) research initiative, which is funded by the Danish Ministry of Science, Technology and Innovation that is also acknowledged for their support.

I would like to thank my supervisors for offering me the possibility to start an interesting PhD project and live this exciting experience in Denmark in an excellent Center and University. Thanks to their careful and friendly supervision, ideas and comments I could learn a lot in these years. It has been a pleasure working with you.
A special thanks to all the colleagues from CINF, CAMD and CEN for brilliant work collaborations and pleasant chats at the Friday bar. Thanks to David to have shared the flat with me and support me during the writing. I would like to thanks all the members of the photocatalysis group and the μ-reactor group, Professor Ole Hansen and Thomas Pedersen for the good ideas and the productive collaboration. A special thank to Peter C. K. Vesborg for his motivating interest in my project and precious advice and Morten G. Nielsen for the work together at the photo μ-reactor setup and the stimulating discussions and support.
I would like to thank Su-Il In for introducing me with the μ-reactor setup and all the helps during the first months of my Ph.D.
I would also like to thank Dan Shacham and Peter Christensen for helping me building the setup, Anders Poulsen for his help in the electronics components and Robert Jensen for the support with the Volvo UHV chamber. A special thanks to Birgitte So-Young Ahn that helped me in finding a nice apartment when I came to Denmark. I would like to thank also to Stavroula Goula Nielsen and Tine Klitmoeller for their help with the planning of the Ph.D.

I would like to thank also Porfessor Kazunari Domen, Professor Kazuhiko Maeda, Professor Jun Kubota, Professor Masao Katayama, Yanbo Li and all the rest of the group for making my visit to their laboratory in Tokyo very pleasant and for the productive collaboration. A special thanks also to Anders Bo Laursen who shared with me this exciting experience and to my supervisor Søren Dahl and Ib Chorkendorff that offer me this opportunity.

I would also like to thank my family, all the friends and Gaia that have been supporting me during these years. Their visits and their mails made me very happy.

Fabio Dionigi,
Kgs. Lyngby, October 2012

Abstract

The work presented in this thesis is focused on the photocatalytic water splitting reaction. In particular the overall reaction for production of both hydrogen and oxygen has been investigated using water vapor and several light sources. The enormous amount of energy irradiated by the sun and the consequences of its efficient storage are the main motivations behind this research. Indeed, the achievement of solar-driven water splitting could represent a big step for humanity towards a sustainable society based on renewable energy.
The energy problem associated with the increasing world population is discussed in the beginning of this thesis followed by an introduction to the basics of photocatalysis. The experimental setup used in this study and the silicon based µ-reactor technology is described afterwards. Almost the entire work presented in the thesis has been done loading the catalysts in these µ-reactors and analyzing the products of the reaction with a quadrupole mass spectrometer (QMS).

Several catalysts have been tested for photocatalytic water splitting: GaN:ZnO, $SrTiO_3$, TiO_2, $NaTaO_3$…, most of them in the form of nanopowder and loaded with cocatalyst nanoparticles. In particular, as an introduction to the water splitting experiments, the results obtained with $SrTiO_2$ and TiO_2 are presented. These semiconductors are well known examples of materials active under UV illumination. However to achieve high efficiency of solar energy conversion the catalysts needs to be active for longer wavelength. GaN:ZnO is one of the few photocatalysts that is able to achieve overall water splitting with visible light. Therefore the reaction has been studied focusing on this material. GaN:ZnO loaded with $Rh_{2-y}Cr_yO_3$ showed high activity and hydrogen and oxygen could even be detected under illumination with a solar light simulator (A.M. 1.5). The dependence of the activity as a function of light intensity showed a linear behavior for the initial rate and has been studied in comparison with the water consumption rate that can be also detected using our µ-reactor. The effects of the temperature of the reactor and the partial pressure of water are also presented and explained in terms of relative humidity. This has been found to be a key parameter for the gas phase water splitting reaction. The results of this study have been combined in simple expression for the rate of photocatalytic hydrogen production.

Hydrogen oxidation experiments have been performed in order to study the water splitting back reaction and explain the high activity of the $Rh_{2-y}Cr_yO_3$/GaN:ZnO. The water formation rate at room temperature was measured with the QMS introducing in the reactor a stoichiometric mixture of hydrogen and oxygen. GaN:ZnO without cocatalyst and loaded with Rh, Pt, Cr_2O_3/Rh, Cr_2O_3/Pt, and Rh–Cr mixed oxide was used for this study and the results are compared with their photocatalytic activities. The water splitting back reaction has been tested both in the dark and under illumination and the results clearly show how the water formation is suppressed for the GaN:ZnO loaded with Cr_2O_3/Rh, Cr_2O_3/Pt, and $Rh_{2-y}Cr_yO_3$ and at the same time the activity is strongly increased respect to Pt/GaN:ZnO and Rh/GaN:ZnO.

The last chapter discusses the efforts that have been done to achieve the goal of obtaining in situ supplementary information to the products detection using µ-reactors. In particular a new kind of µ-reactor that has a Pyrex lid on both sides is presented. With

this reactor is possible to measure the absorbance of the materials deposited inside the μ-reactor and to combine optical measurements and spectroscopy with the detection of activity with the QMS. Finally an attempt to combine the μ-reactor with surface science techniques working under UHV is presented. The strategy is based on replacing the standard μ -reactor with an open μ-reactor that can be closed by pressure. The design and realization of the setup and the preliminary problems encountered are described.

Resumé

Arbejdet præsenteret i denne afhandling er fokuseret på den fotokatalytiske vandspaltningsreaktion. I særdeleshed har den samlede reaktion til fremstilling af hydrogen og oxygen været undersøgt under anvendelse af vanddamp og flere forskellige lyskilder. Den enorme mængde af energi der udsendes af solen, og relevansen af en effektiv udnyttelse og opbevaring af denne, er de vigtigste motivationer bag denne forskning. Realiseringen af sol-dreven vandspaltning kunne medføre et stort skridt for menneskeheden i retning af at opnå et bæredygtigt samfund baseret på vedvarende energi.
Energi-problemerne vedhæftet den voksende verdensbefolkning diskuteres i begyndelsen af denne afhandling, efterfulgt af en introduktion til de grundlæggende principper bag fotokatalyse.
Forsøgsopstillingen anvendt i denne undersøgelse, og den siliciumbaserede μ-reaktorteknologi er beskrevet efterfølgende. Næsten hele arbejdet præsenteret i afhandlingen er udført ved at lægge katalysatormaterialet i disse μ-reaktorer og analysere produkterne fra reaktionen med et kvadrupol massespektrometer (QMS).

Adskillige katalysatorer er blevet testet for fotokatalytisk vandspaltning: GaN:ZnO, $SrTiO_3$, TiO_2, $NaTaO_3$ ..., de fleste af dem i form af nanopulvere dækket med cokatalysator nanopartikler. Som en introduktion til vandspaltningseksperimenterne, præsenteres de opnåede resultater med $SrTiO_3$ og TiO_2. Disse halvledere er velkendte eksempler på aktive materialer under UV-belysning. For effektivt at omdanne solenergi, kræves det dog at katalysatorerne er aktive ved længere bølgelængder af lys. GaN:ZnO er en af de få photokatalysatorer der er kan opnå overordnet vandspaltning med synligt lys. Derfor er reaktionen blevet undersøgt med fokus på dette materiale. GaN:ZnO dekoreret med $Rh_{2-y}Cr_yO_3$ viste høj aktivitet, og brint og ilt kunne detekteres selv under belysning med en sollys-simulator (AM 1,5). Afhængigheden af aktiviteten som en funktion af lysintensitet viste en lineær adfærd for den indledende hastighed, og er blevet sammenholdt med vand-omsætningen, som også kan detekteres ved hjælp af vores μ-reaktorer. Aktivitetens afhængighed af reaktorens temperatur og partialtrykket af vand er også vist, og forklaret på baggrund af relativ fugtighed. Dette har vist sig at være af afgørende betydning for gasfase vandspaltningsreaktion. Resultaterne af denne undersøgelse er blevet kombineret i enkle udtryk for hastigheden af fotokatalytisk brintproduktion.

Brint- oxidationsforsøg er blevet udført for at undersøge vandspaltningens modsatrettede reaktion, og forklare den høje aktivitet af $Rh_{2-y}Cr_yO_3$/GaN:ZnO. Vandets dannelsesrate ved stuetemperatur blev målt med et QMS, mens en støkiometrisk blanding af brint og ilt blev indført i reaktoren. GaN:ZnO uden cokatalysator og dækket med Rh, Pt, Cr_2O_3/Rh, Cr_2O_3/Pt, og Rh-Cr blandet oxid blev anvendt til denne undersøgelse, og resultaterne er sammenholdt med deres fotokatalytiske aktiviteter. Vandspaltningens modsatrettede reaktion er blevet testet både i mørke og under belysning, og resultaterne viser tydeligt hvordan vandudviklingen undertrykkes for GaN:ZnO dækket med Cr_2O_3/Rh, Cr_2O_3/Pt og $Rh_{2-y}Cr_yO_3$,og at aktiviteten samtidig er stærkt forøget i forhold til Pt/GaN:ZnO og Rh/GaN:ZnO.

Det sidste kapitel omhandler de bestræbelser der er gjort for at nå målet om in situ

supplerende information til de detekterede produkter ved hjælp af μ-reaktorer. I denne sammenhæng præsenteres en ny form for μ-reaktor med Pyrex låg på begge sider. Med denne reaktor er det muligt at måle absorbansen af materialet indeni μ-reaktoren, og kombinere optiske målinger og spektroskopi med målinger af aktiviteten med QMS'et. Afslutningsvis præsenteres et forsøg på at kombinere μ-reaktor med overfladeanalyseteknikker som kræver UHV. Strategien for dette er baseret på en udskiftning af standard μ-reaktoren med en åben version, der kan forsegles med tryk. Design og realisering af det eksperimentelle udstyr, samt foreløbige problemer er beskrevet.

List of included papers

Photocatalysis

- **Dionigi F.**, Vesborg P. C. K., Pedersen T., Hansen O., Dahl S., Xiong A., Maeda K., Domen K. and Chorkendorff I., "*Suppression of the water splitting back reaction on GaN:ZnO photocatalysts loaded with core/shell cocatalysts, investigated using a μ-reactor*", JOURNAL OF CATALYSIS, 292 26 (2012).
- **Dionigi F.**, Vesborg P. C. K., Pedersen T., Hansen O., Dahl S., Xiong A., Maeda K., Domen K. and Chorkendorff I., "*Gas phase photocatalytic water splitting with $Rh_{2-y}Cr_yO_3$/GaN:ZnO in μ-reactors*", ENERGY ENVIRON. SCI. 4 2937 (2011).
- **Dionigi F.**, Vesborg P. C. K., Pedersen T., Hansen O., Dahl S. and Chorkendorff I.*,"A transparent Pyrex μ-reactor for combined in-situ optical characterization and photocatalytic reactivity measurements"*, in preparation (not included).

Others

- Laursen A.B., Varela A.S., **Dionigi F.**, Fanchiu H., Miller C., Trinhammer O.L., Rossmeisl J. and Dahl S., "*Electrochemical Hydrogen Evolution: Sabatier's Principle and the Volcano Plot*", J. CHEM. EDU., accepted (2012).

Table of Contents

"AFTER a long silence, for which I shall offer no apology, I have the pleasure of communicating to you, and through you to the Royal Society, some striking results I have obtained in pursuing my experiments on electricity excited by the mere mutual contact of different kinds of metal..."

A. Volta, in a letter to Sir Joseph Banks published in Philosophical Transactions, 1800.

"Within six weeks of Volta's report, two English scientists, William Nicholson and Anthony Carlisle, used a chemical battery to discover electrolysis (the process in which an electric current produces a chemical reaction) and initiate the science of electrochemistry. In their experiment the two employed a voltaic pile to liberate hydrogen and oxygen from water."

Encyclopædia Britannica, 2012.

Chapter 1

Introduction and Background

1.1 Introduction

This thesis is an investigation of the photocatalytic water splitting reaction, which is considered a potential route for solar energy conversion and hydrogen production. The overall reaction has been studied using water vapor and nanoparticulates photocatalysts loaded with cocatalysts. The photoelectrochemical water splitting approach in which the reaction occurs on electrodes made of photocatalytic materials is not treated in this thesis.

In this chapter a brief introduction to the energy problem and the photocatalytic water splitting approach is presented followed by a short outline of the dissertation. This chapter is intended for a reader not familiar with photocatalytic water splitting.

1.2 Energy consumption

The dramatic increase in world population in the last centuries raises the question of how long the resources of our planet will last. The world population is estimated to be 7.023 billion by the United States Census Bureau (30/06/2012) [1] and according to the World Population Prospect of the United Nations it is expected to increase even more (Fig. 1.1).

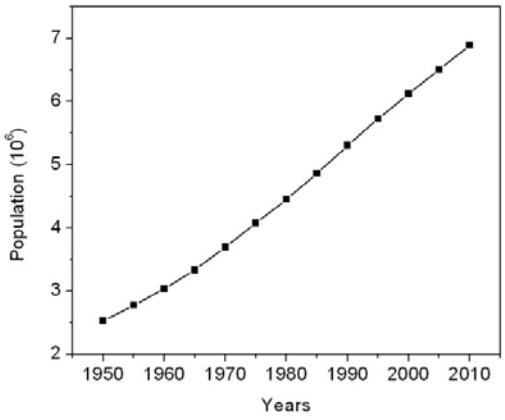

Fig. 1.1 World population based on the data from the U.N. Population Division. (http://esa.un.org/unpd/wpp/unpp/panel_population.htm).

At the same time also the world energy consumption (Fig. 1.2), mostly based on fossil fuels as oil, coal and gas is increasing [2]. These resources are created by a geological slow process and therefore their amount is limited. Being a finite resource, it is logical to expect to reach a maximum and decline in the production in the future [3].

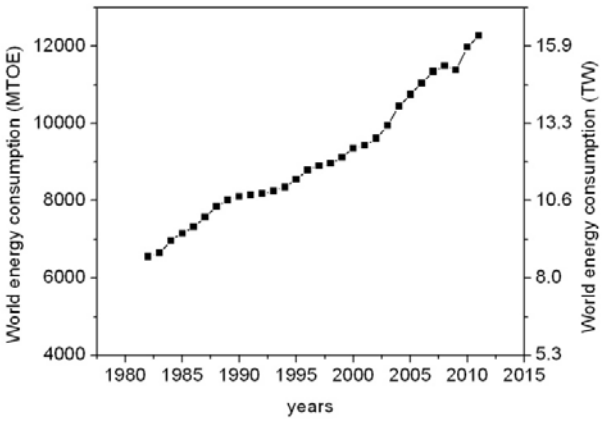

Fig. 1.2 World energy consumption adapted from the data provided by the BP Statistical Review of World Energy June 2012. The scale in TW is calculated assuming 1 MTOE = 11.63 TWh and 1 year = 8765.81277 h.

Several estimations predict that the oil and natural gas will last for a number of decades, with coal lasting up to a few hundred years, though there is not agreement on the exact numbers. Most of the analyses are based on conventional oil, but the numbers will be different if new oil resources are found and can be extracted. Currently, oil companies are investing in unconventional oil, extracted with techniques different than the traditional oil well method and from places that can't be reached with the present technology. Of course this oil is more expensive than the conventional oil.
The damage to the world economy will be high if the production of oil starts to decrease rapidly. Therefore an efficient mitigation of the problem via the introduction of new technologies must be started well in advance because the time scale for introducing new technologies to our society can be very long.

The use of fossil fuels is relevant also to a number of other issues. For instance, when fossil fuels are consumed and burnt, CO_2 is emitted into the atmosphere. This gas is not fixed by nature at a fast rate and so it stays in the atmosphere for a long time. The so called carbon cycle is therefore broken. There is no doubt that the CO_2 in the atmosphere is increasing due to human activities. Indeed the continuous measurements taken at the Mauna Loa Observatory in Hawaii by C. D. Keeling et al. [4] (Fig. 1.3) show concentrations that are higher than the maximum value of the oscillations in the last 400 thousands of years (preindustrial level: ~280 ppm) and keep on rising [5]. Since CO_2 is a green house gas, this graph suggests the risk of an environmental problem. It is expected that the increase of CO_2 in the atmosphere may lead to an increase in the global average temperature. This warming of the planet will probably lead to the melting of the arctic ice and glaciers and changes of climate with consequences for all the life forms on our planet. As a matter of fact, an increase in temperature during these decades (~0.2°C/decade in the past 30 years) has been measured. The data are shown in Fig. 1.4 taken from an online report by NASA [6] that consists in updates of the work by Hansen et al. [7].

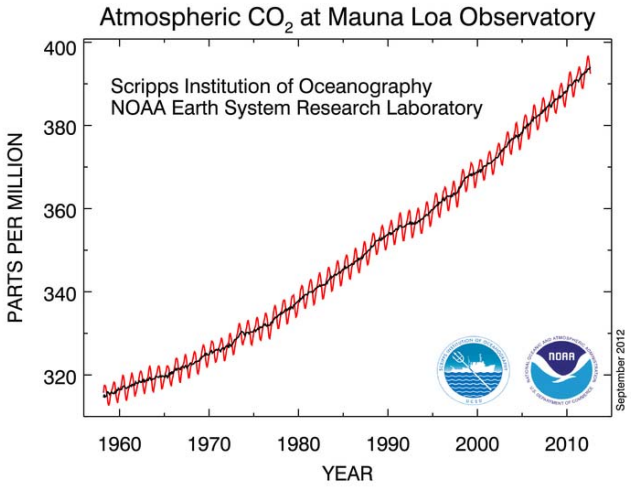

Fig. 1.3 Atmospheric CO_2 concentration in ppm measured at Mauna Loa Observatory. Adapted from http://www.esrl.noaa.gov/gmd/ccgg/trends.

Even if the cause-effect correlation between the increase CO_2 level and the global average temperature increase is not fully proven, there is a very high probability that the higher CO_2 level together with the emission of other green house gases like CH_4 by human activities is the cause of the global warming. If we prudently assume that this probability is equal to 1, due to the long lifetime of CO_2 in the atmosphere, we should find ways to decrease the CO_2 production as quickly as possible [8].

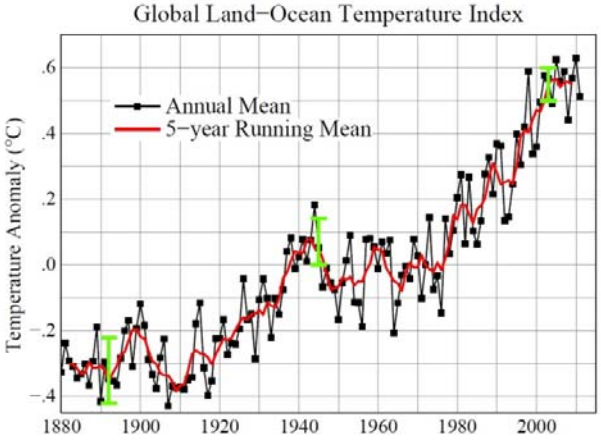

Fig. 1.4 Global temperature adapted from http://data.giss.nasa.gov/gistemp/graphs_v3.

The proposed CO_2 sequestration that involves capturing emitted CO_2 and trapping it underground is not a long term viable solution because the carbon cycle will not be closed, and so the result is only a postponement of the problem.

Another important consideration with fossil fuels is that these resources are localized. They are controlled by a few nations, and so a net of dependences and a delicate equilibrium is created at international level. The breaking of this equilibrium is the

cause of almost all the wars of the contemporary era. Unlike fossil fuels, solar energy is distributed more homogeneously on our planet. Therefore the use of solar energy technology "will increase countries' energy security through reliance on an indigenous, inexhaustible and mostly import-independent resource" [9].

1.3 The sun as an alternative

The sun that we often see shining in the sky over our heads can be the solution for a society that wants to move from fossil fuels to renewable and sustainable energy sources. The sun is a yellow dwarf star with a diameter of about 109 times the one of the earth and produces energy by nuclear fusion of hydrogen into helium. This energy is generated in the core of the sun, and diffuses into the surrounding universe in the form of kinetic energy of particles or light radiation. The photons leaving the sun photosphere travel an average distance of $1.496 \cdot 10^8$ km before reaching the Earth (it takes around 8 minutes). Solar light makes possible the life as we know it, being responsible of climates and providing energy, directly or indirectly, to almost all the life form that are present on our planet. Since the sun is expected to shine for billions of years more, it can well be considered an inexhaustible source of energy on human time scale.

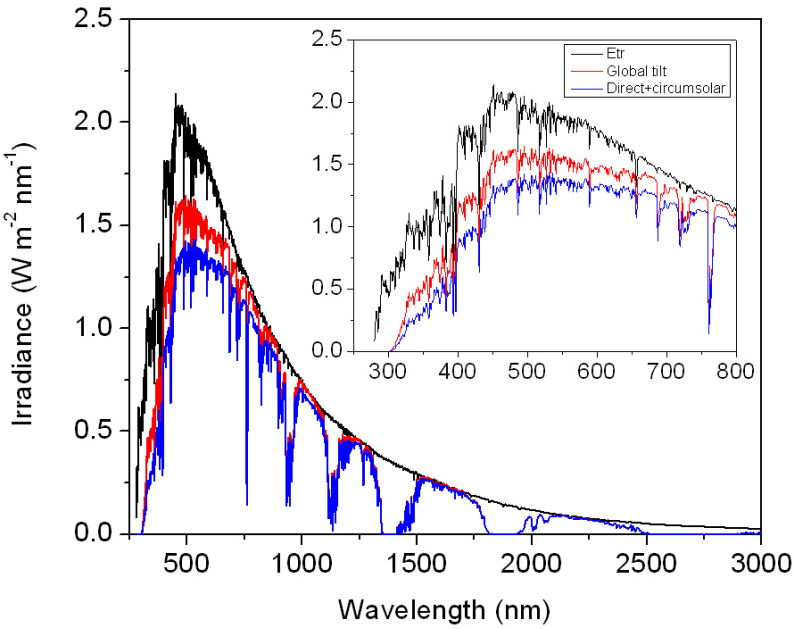

Fig. 1.5 Solar spectral irradiance. Extraterrestrial (black), AM 1.5 direct normal (blue), AM 1.5 global on a 37° tilted surface (red). From data available online at http://rredc.nrel.gov/solar/spectra/am1.5.

In Fig. 1.5 the solar irradiance is plotted as a function of wavelength for standard condition (AM 1.5) [10]. The solar power intercepted by the Earth is ~1.37 kW/m^2. If we multiply this number by the cross section of the Earth and divide by the surface area of the Earth we obtain a space and time average solar power. If we also take into account the scattering and absorption by the atmosphere and the clouds we obtain a

value of 174.7 W/m^2 for the space and time average flux of solar light reaching the Earth surface. Since the global average annual energy consumption by mankind is about 15 TW, it is easy to see the huge potential that solar energy has. With a device working at 10% efficiency of solar energy conversion we need only to cover an area equal to 0.17% the Earth surface to obtain the mentioned 15TW. However due to the alternation of day and night, sunny and cloudy day, etc... the solar energy is not a constant source of energy. For this reason it is not enough to convert it to electricity, an easily useable form of energy, but we need to store it. Unfortunately electricity is not a good way to store large amount of energy. Batteries and capacitors have a poor gravimetric and volumetric energy density, so that it makes sense to use them only for small portable applications. There are however forms of energy that have a higher energy density: its name is chemical energy. In this case the energy is stored in chemical bonds and released if necessary by a chemical reaction i.e. combustion in the case of fossil fuels.

1.4 Water splitting in photosynthesis

Nature has found a way to convert solar energy into chemical energy. It is therefore interesting to see what approach has passed the strict rules of natural selection to see if it can be a source of inspiration for the realization of an artificial device. In this paragraph I will give a brief description of water splitting in photosinthesis without any claims of completeness.
The process of photosynthesis occurs in plants, algae and some species of bacteria (i.e. the cyanobacteria). Even if the process can vary from species to species there are some common features. The process consists of the conversion of carbon dioxide into sugars, the “fuel”, using water and solar light and releasing oxygen (oxygenic photosynthesis). The general reaction is:

$$2n\ CO_2 + 2n\ H_2O + photons \rightarrow 2(CH_2O)_n + 2n\ O_2 \qquad (1.1)$$

and it can be divided into two main stages: the first one uses light to split water and makes energy storage molecules while the second stage is light independent and uses the stored energy to reduce CO_2. Since my project is focused on the water splitting reaction, and not on CO_2 reduction, we will focus only on the first light-dependent stage. In plants and algae this process occurs in cell subunit called chloroplasts. There the light is absorbed at the photosystem II (PSII) by a green pigment called chlorophyll (plus other pigments called carotenoids). This molecule absorbs more in the blue and red portion of the spectra, as can be seen from Fig. 1.6. There is still not a fully convincing theory about why the plant doesn't absorb green light, and so a substantial part of solar light. The reason might not be relevant for an artificial device where high efficiency will be obtained probably only absorbing also this part.
The light absorbed is converted through the generation of a radical pair in electrochemical potential that is believed to be enough to oxidize water and reduce protons to hydrogen [11]. Water is indeed oxidized at the oxygen evolving center (OEC) into protons and molecular oxygen. The catalytic core of the OEC is composed of a cluster of four manganese ions (oxidation states ranging from +3 to +5) and a calcium ion (Ca^{2+}) binds to oxygen. The structure of the Mn_4CaO_5 cluster is proposed to be formed of a cubane-like Mn_3CaO_4 cluster linked with the fourth Mn ion outside the

cubane [12].

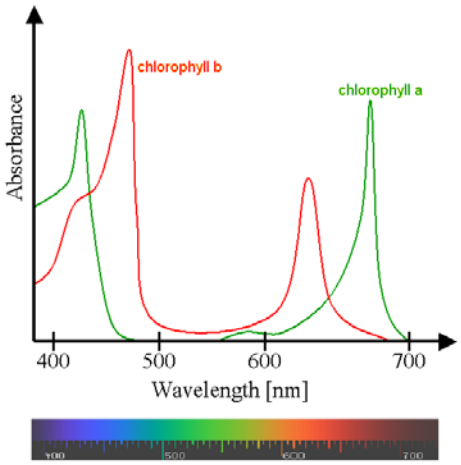

Fig 1.6 Absorbance of chlorophyll a and b. Adapted from http://commons.wikimedia.org/wiki/File:Chlorophyll_ab_spectra2.PNG

While nature oxidizes water to produce oxygen, it prefers not to reduce the protons created at the OEC but to pass the reducing equivalent along an electron transport chain to a second photosystem (PSI). This gives rise to the complex pathway shown in Fig. 1.7 known as z-scheme.

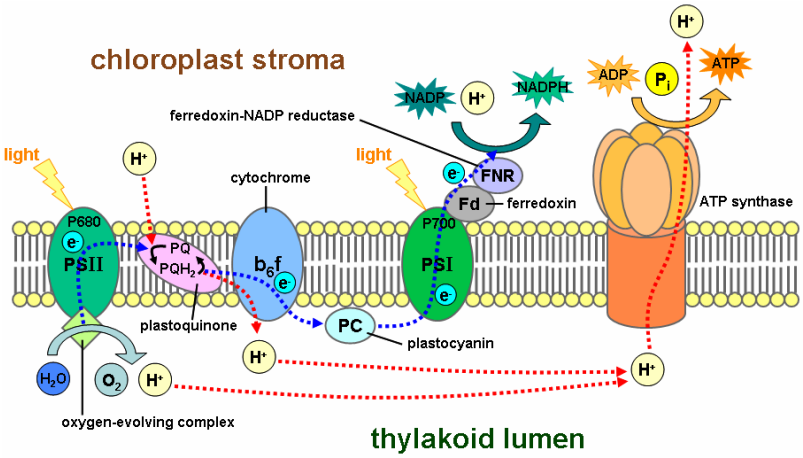

Fig. 1.7 Light dependent reactions of photosyntheisis. http://en.wikipedia.org/wiki/File:Thylakoid_membrane.png

During the electron transport chain a proton gradient is created across the chloroplast membrane and used by the enzyme ATP synthase to synthesize adenosine triphosphate (ATP), an energy storage molecule. At the PSI, light is absorbed by another chlorophyll molecule and the reducing equivalent excited to a more negative potential. The electron is passed to ferrodoxin and finally to the enzyme NADP-reductase where the reduction of the co-enzyme nicotinamide adenine dinucleotide $NADP^+$ to NADPH occurs. This molecule acts as a hydrogen carrier. In the process described so far, water has been split

using solar energy into oxygen and protons bound to hydrogen carrier molecules and extra energy is stored in ATP.
Even if the process of photosynthesis is very complex, the efficiency reached is quite low. The estimated maximum efficiency is only 5.52%, while in reality when averaged over a year it is between 0.5% and 1.3% for regions in the temperate zones [13].
In the next paragraph I will describe an artificial approach to store solar energy based on principles in common with the first stages of photosynthesis but with the hope to achieve higher efficiency.

1.5 Photocatalysis for water splitting

Similar to photosynthesis, in photocatalytic water splitting the water is oxidized into oxygen and protons, but, unlike what happens in plants, the protons are reduced to hydrogen. The overall reaction is:

$$2H_2O \rightarrow 2H_2 + O_2 \qquad (1.2)$$

Like photosynthesis, this reaction is an uphill reaction, with a positive and large change in Gibbs free energy $\Delta G^{\circ} = 238$ kJ/mol. It utilizes solar light as an inhexaustible energy source and water that is very abundant, covering ~70% of Earth's surface. Hydrogen can be used as an energy carrier and can recombine with oxygen in a fuel cell, releasing the stored energy and giving as product only clean water. Hydrogen generated this way can also be directed to chemical plants, since it is a fundamental building block of many important chemicals used every day by our society. For example, ammonia is among the most highly produced chemicals and it is synthetised by the Haber-Bosch process using hydrogen obtained by methane reforming.

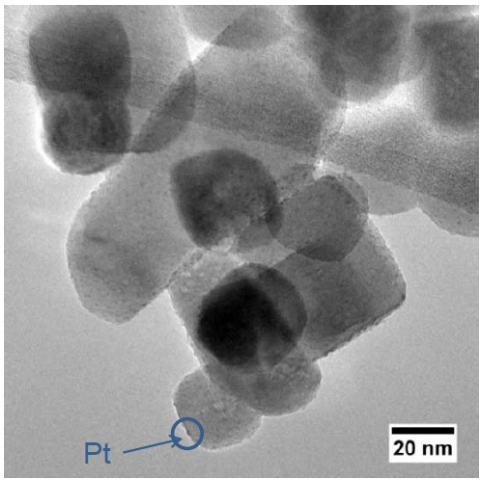

Fig. 1.8 TEM image of 1wt% Pt cocatalysts loaded on $SrTiO_3$ nanopowder. Image by F. Cavalca.

In 1972 Fujishima and Honda in their famous publication [14] showed that a single crystal TiO_2 rutile photoanode and a Pt cathode can photoelectrochemically split water after applying a small external bias. With their paper the authors "suggest that water can be decomposed by visible light into hydrogen and oxygen, without the application of

external voltage" if a proper semiconductor is used. This result opened up an enthusiastic research in the following years in the attempt to build such a system. Several approaches have been followed and can be found in many reviews. Since in my project I have worked only with one of them, I will focus my discussion on it. This method is based on a nanoparticulate one step photoexcitation material and it is one of the most promising thanks to its simplicity and potential low cost. Unlike the system used by Fujishima and Honda that utilizes electrodes, here the materials are used in the form of nanopowders. Nanopowders have large surface area, which is a positive effect as more sites are available for the reaction, and the cost of bulk material can be relevant in a cost analysis of the device. Furthermore this system does not include wires and the troubles generated by wire connections and resistances. Semiconductor nanoparticles are used as light absorber and referred to as photocatalysts. They are often decorated by metal cocatalysts (see Fig. 1.8) and their function will be explained in the following. Typical dimensions of a photocatalyst are 100-150 nm in diameter, but can extend in the micrometers range, while the cocatalysts that are loaded on the surface have typical dimensions around 2-5 nm.

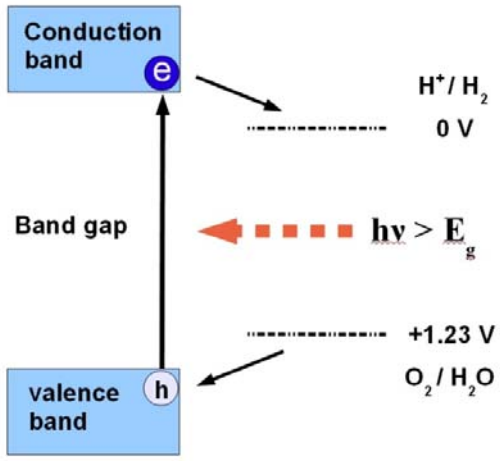

Fig. 1.9 Basic principle of water splitting using semiconductor photocatalyst.

The photocatalytic water splitting mechanism can be explained with the following steps:

1) **Light absorption**: The photocatalyst absorbs the photons. When a semiconductor absorbs photons with energy higher than its band gap ($h\upsilon > E_g$), the negative electrons are promoted to the conduction band leaving positive charged holes in the valence band (Fig. 1.9). The value of the bandgap is the relevant parameter to absorb the wanted amount solar radiation, but also the level of the conduction and valence band are important. Indeed in order for the promoted electrons to reduce the protons and be able to perform the half reaction:

$$2H^+ + 2e^- \rightarrow H_2 \qquad (1.3)$$

, the bottom of the conduction band needs to be more negative than the redox potential of H^+/H_2 (0 V vs NHE). Similarly the top of the valence band needs to

be more positive than the redox potential of O_2/H_2O (+1.23 V vs NHE) in order for the holes to perform the other half reaction:

$$2H_2O + 4h^+ \rightarrow 4H^+ + O_2 \quad (1.4)$$

From this consideration the band gap has to be at least greater than 1.23 eV since in this approach only a single bandgap material is used. From thermodynamics we should consider that the free energy available per electron to drive the reaction is not equal to the bandgap of the semiconductor, but to the difference of the quasifermi levels of the excited electrons and holes (the photovoltage of a solar cell). So it is this difference that has to be greater than 1.23 eV [15]. For a good silicon solar cells the difference between the bandgap and the quasifermi levels difference is ~0.5 eV. For this reason the bandgap of the desired semiconductor needs to be greater than ~1.7 eV. Furthermore for practical application one has to consider that to run the two redox reactions an overpotential is required. From what it is known in electrochemistry, the potential for HER can be relatively low for a good catalyst, ~0.1 eV, while for OER overpotentials of ~0.2-0.4 eV are often required even with the best catalyst available. The conclusion is that the minimum requirement for a bandgap is to be greater than 2.0 eV (or more likely 2.2 eV). With a band gap of 2.2 eV a solar conversion efficiency of ~15% can be obtained.

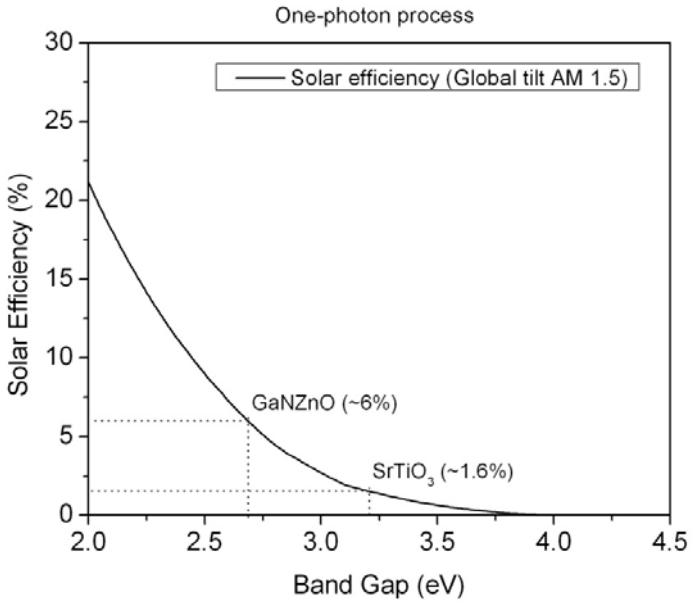

Fig. 1.10 Solar efficiency calculated using solar spectral irradiance AM 1.5 for a surface tilted 37°. The values for GaN:ZnO and $SrTiO_3$ are shown as examples.

This number is obtained using the solar spectrum at standard condition (A.M. 1.5) [10] (see Fig. 1.5). After converting the irradiance in number of photons the spectrum is integrated starting from the energy of 2.2 eV to the highest energy photons and dividing it by the total number of photons obtained from the full integral. In Fig. 1.10 the solar efficiency calculated with this method is plotted as

a function of the energy of bandgap of potential semiconductor candidates. GaN:ZnO and $SrTiO_3$, the material on which I have spent most of the time of my project, are indicated in the graph.

2) **Charges separation and migration**: After absorptions, electron-hole pairs are created. These photocarriers have to migrate to the surface in order to drive the reaction. Avoiding electron-hole recombination is fundamental in this step, because this effect produces an effective loss of the captured energy (in the form of heat for a non radiative recombination or as photons that can be not absorbed again for a radiative recombination).
   Since structural defects and impurities can act as trapping and recombination centers, chemically pure and highly crystalline materials are desirable to optimize this step.
   Loading the photocatalyst with a high workfunction metal like Platinum is thought to improve the efficiency of this step since the metal can trap electrons, extracting them from the semiconductor, and so minimizing the electron-holes wavefunctions overlap.
   Decreasing the particles sizes of the photocatalyst, other than increasing the relative surface area, also has the effect of decreasing the distance of migration from the generation of a photocarrier to the surface, reducing the probability of recombination. However, obtaining small crystalline particles is difficult. Small particles are often highly defective, which can lead to worse performance.
   A problem present in some semiconductor materials like ZnO and many metal sulfides, i.e. CdS, is that the photocarriers, instead of migrating to the surface to perform the wanted redox reactions, prefer for example to oxidize the ions of the material i.e. the holes prefer to oxidize the S^{2-} in CdS and O^{2-} in ZnO instead of water. This process is known as photocorrosion and has to be suppressed in order to have a stable photocatalyst.

3) **Surface chemical reactions**: At the surface the holes with the appropriate energy can oxidize water and the electrons reduce the protons. In this step, the surface of the catalyst is playing the important role, therefore having a system with highly active sites and high number of active sites is the requisite to obtain high efficiency. The semiconductors normally used as photocatalysts are bad catalyst for hydrogen evolution reaction (HER). Therefore the semiconductor particles are often loaded with noble metals to improve the surface reaction kinetics. Platinum is a typical cocatalyst for hydrogen evolution. In principle also a cocatalyst for the oxygen evolution reaction (OER) can be loaded *i.e.* IrO_2 or RuO_2. However this is often not done because it doesn't produce a big enhancement in the activity. This is probably due to the fact that almost the totality of the photocatalysts reported to work for the overall photocatalytic water splitting are metal oxide. In metal oxides the O2p orbital of the oxygen is the main contribution of the valence band, leading to a highly positive valence band. Therefore the holes have a high overpotential to drive the water oxidation. However if as smaller band gap semiconductor is discovered to work for this reaction i.e. a nitride or oxynitride, this kind of cocatalyst may be also useful to improve the kinetics and so the overall efficiency.

In the previous discussion we have seen that the role of the cocatalyst is both to reduce recombination between electrons and holes and to improve the surface kinetics by providing active sites for HER. At the same time the role of the photocatalyst is to absorb the photons and, in the case where only a cocatalyst for HER is loaded, to provide the active sites for OER.

1.6 Prospective for realistic water splitting plants

If all the steps described so far are satisfied, then photocatalytic water splitting can occur. From a practical realization and commercial point of view, the main requirements that our material need to have are stability, efficiency and low cost (toxic materials should also be avoided). In the case of the approach that we are describing 10 years of particle lifetime and 10% of solar-to-hydrogen efficiency, as suggested by James et al. in a recent technoeconomic analysis report, are reasonable but highly challenging values for these parameters [16]. In the same work the authors proposed a reactor design based on these and other technical assumptions in order to produce with this baseline module 1 ton of hydrogen per year in the cheapest way. According to their prediction a price of \$ 1.63/kg H_2 will be obtained with such a system.

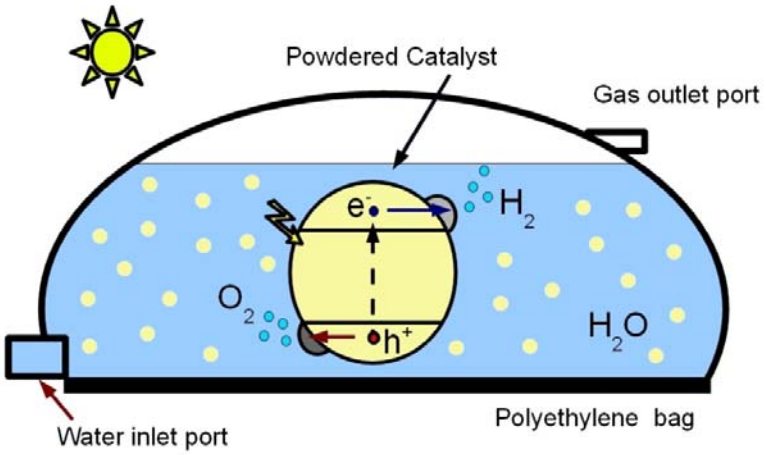

Fig. 1.11 Cartoon showing the "baggie" device with the colloidal suspension of photocatalyst nanoparticles. The photocatalytic mechanism is also shown in the zoom in of a nanoparticle. Notice that the dimensions of the reactor are not in scale.

The system consists of a shallow horizontal plastic (polyethylene) envelope, called a "baggie", that will contain the photocatalyst nanoparticles and pure water (Fig. 1.11). The nanoparticles are in colloidal suspension in water and this one can be resupplied by a water inlet port. The baggie is made so that the upper part can lift above the liquid during hydrogen and oxygen evolution, providing a gas head space. The products collected in this headspace can then exit through a port and pass to a gas handling subassembly. Here the water vapor is removed from the gas mixture by a cooler/condenser, the gas is compressed to 300 psi (20.7 bar) and hydrogen and oxygen

are separated, i.e. by pressure swing adsorption. The optimized proposed dimensions are 32 m long, 1.2 m wide and 10-28 cm high. 18 of these reactors are needed for a plant that produces 1 ton of hydrogen per day.
A preliminary estimation for the realization of a water splitting plant have been done also by Domen at al. [17]. To design their large-scale plant the authors also assumed a 10% solar to hydrogen efficiency and the goal "to provide one-third of the projected energy needs of human society in 2050 from solar energy". From these considerations they suggest that if a plant with an area of 5km by 5 km (25 km^2) can be built the entire world would need 10000 of such plants to accomplish the goal. Each of these large-scale plants should produce 570 tons of hydrogen per day.
One of the main problems of using one step excitation nanoparticulate photocatalyst system clearly emerges from the discussion of these plants. This is the fact that hydrogen and oxygen are produced in the same reactor bed and in the ratio that is within the inflammability range of this mixture (4-95 % hydrogen in pure oxygen). Even if after it has been extracted from the reactor this inflammable mixture can be handled by the standard industrial technology, there is still a safety issue and risk of ignition while the gases are in the reactor. A good technology has to be developed to provide a solution to this problem and this may raise the cost of the plant.
Despite the open technical challenges, the numbers that come out from above analysis clearly provides optimism for large scale inexpensive water splitting.

1.7 Dissertation overview

In the following part of the thesis the discussion has been divided into four chapters.

Chapter 2 introduces the experimental setup and the silicon based μ-reactor. This chapter is important to understand the following two chapters (chapter 3 and 4) since the measurements presented in those chapters are obtained with the μ-reactor described here. This μ-reactor is also the base for the modifications done to design two new kinds of μ-reactors described in chapter 6.

In chapter 3 I present some relevant gas phase photocatalytic water splitting experiments that I have done during my PhD. The conditions that increase the activity for this reaction are investigated.

Chapter 4 can be view as a continuation of chapter 3. Here I discuss the water splitting back reaction and the experiments designed to measure the water formation rate.

Finally, in chapter 5 I discuss two projects aimed at combining photocatalytic reactivity measurements and in-situ characterization. The first is about a Pyrex transparent μ-reactor to perform in situ optical measurements. The second is an attempt to interface an open μ-reactor with a UHV chamber equipped with surface science tools.

The thesis ends with the general conclusion and the outlook (chapter 6).

Chapter 2

Experimental setup

2.1 Silicon based µ-reactor

Almost all the experiments presented in my thesis were done using silicon based gas phase µ-reactors. This kind of technology was developed in my group and it is described in previous publications [18, 19]. The reactors were fabricated in DTU Danchip by Toke R. Henriksen and Thomas Pedersen from DTU Nanotech under the supervision of prof. Ole Hansen. This paragraph introduces the µ-reactor device, describing its design and its advantages.
Our µ-reactor is a plug flow reactor for gas phase application (0.1 - 3 bar) and it is a sandwich device made by two components: a Pyrex lid and a silicon chip (Fig. 2.1).

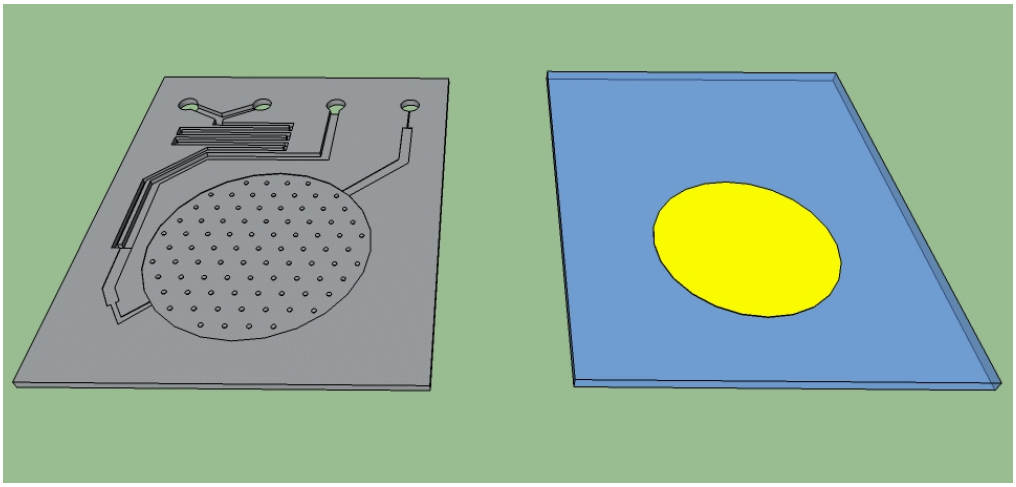

Fig. 2.1 Sketch of the silicon chip with the etched structure and the Pyrex lid. The deposited layer of catalysts nanoparticles is shown in yellow.

The silicon part is made by cutting a standard silicon wafer of crystalline Si(100). Similarly, the Pyrex lid is diced from a Pyrex wafer. Both of the parts have the same lateral dimensions 20 x 16 mm, while differing in thickness: the Pyrex is 500 µm thick, while the silicon 350 µm. Thanks to this small area, up to 16 reactors can be obtained from two single wafers of Pyrex and silicon. Before being cut into the 16 reactors, the silicon wafer is wet etched in order to create a structure of channels and a reactor chamber. The details and the steps of the fabrication process are given in reference [18]. Four holes are also etched all the way through the silicon chip. These four holes represent the only features on the back side of the silicon, while both the channels and the reactor chamber are etched on the front side. In Fig. 2.1 we can see that the chip has two inlet channels as well as a long meander structure. Its role is to allow proper gas mixing in the small volume of the chip. To deal with small volumes is an important feature in case poisonous or dangerous inflammable gases need to be used. The need of

such a long structure is due to the fact that in the reactor the flow is laminar (small Reynolds number, i.e. Re = 53 in case of air at 300 K and 1 bar and a flow of 10 ml/min). Therefore, two gases can only mix by diffusion, which is a slow process. After passing the mixing structure, almost all the gas molecules continue to flow through a wide channel and exit the reactor from the first output hole. A pressure controller, placed in the external gas line after this first outlet, regulates the total pressure in the chip.

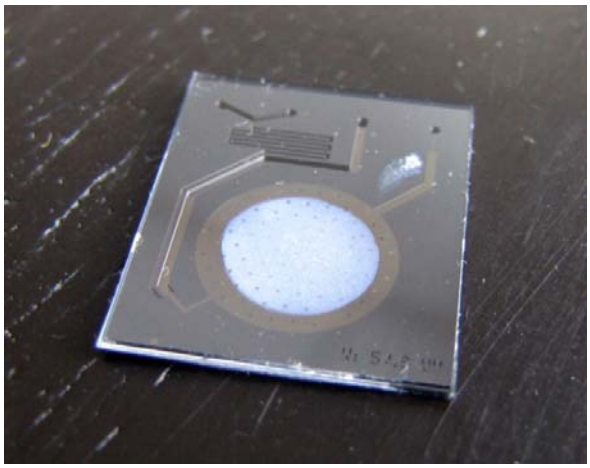

Fig. 2.2 Anodically bonded μ-reactor loaded with catalyst.

In a typical experiment, the flow entering the chip and exiting through the first outlet has a value in the order of ml/min and can be easily controlled with regular mass flow controllers (MFCs). The gases that exit through the first outlet are wasted. However, a small part of the flow can enter the reactor chamber through a shallow channel after the meander structure. This shallow channel, the reactor chamber and the channel that connects the reactor chamber with the second outlet are etched down to only 3 μm, while the part described before was etched down to 250 μm. The small dept of the circular reactor chamber combine with a diameter of only 1 cm give a total volume of 240 nl. This chamber is etched leaving many silicon pillars standing vertical from the bottom. These pillars prevent the Pyrex to collapse in the case of high temperature anodic bonding (as it will be described later). The reagents that enter the reaction chamber and the products of the catalytic reactions are detected by a quadrupole mass spectrometer (QMS) connected to the second outlet hole. A capillary at the end of the channel connected to the reactor chamber limits the flow to the QMS, so that the detector can work under the range of pressure appropriate for its operation (under standard experiments the pressure in the QMS chamber is 10^{-7}- 10^{-6} mbar), while the pressure in the reactor chamber can be kept to ambient pressure (1 bar). As a final fabrication step, the chip is thermally oxidized and an oxide with the thickness of 50 nm is formed.

The catalyst can be deposited on the as prepared silicon chip or on the Pyrex lid. The typical loading method is drop casting a solution of catalyst nanoparticles suspended in water (i.e. 5 mg in 5 ml) using a micropipette and a circular mask with a diameter of 8 mm. Spin coating is also used occasionally.

Once the catalyst has been deposited and dried, the two parts can be anodically bonded

together. In this way the final device is obtained (Fig. 2.2). This kind of sealing does not use any glue, reducing the possibility of contaminants. During anodic bonding, the chip is placed on a hot plate kept at temperature in the range 330-400˚C (Fig. 2.3). This plate is in contact with the silicon side of the reactor and it is kept at ground potential. At the same time, a potential of -1 kV is applied to a metal tip touching and pressing the Pyrex side on top of the silicon. After a time as short as half an hour or one hour, the reactor is bonded and ready to be tested. We call this way of anodically bond a sample a hot bonding because both the chip and the catalyst are kept at the same high temperature. In order to be able to bond a reactor without exposing the catalyst to high temperatures, a new way of anodically bonding has been developed some years ago by my group [19]. We call this bonding a "cold" bonding, because here the catalyst is kept at low temperatures by touching the area of the silicon underneath the reactor chamber by a cold finger (Fig. 2.3). This is a copper block kept at 10-15˚C by water cooling. The rest of the chip is heated at ~450˚C by two halogen lamps placed in an aluminum block above the Pyrex side. In this way the estimated temperature of the catalyst is ~50˚C. This kind of bonding usually takes one hour and a half.

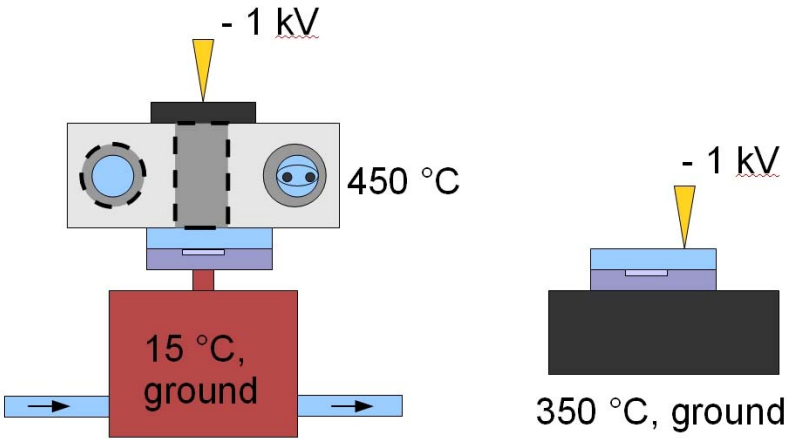

Fig. 2.3 Sketch of the setups for anodic cold bonding and standard anodic hot bonding.

Almost all the products and reagents that enter the reactor chamber are detected by the QMS. This is possible because back-diffusion from the shallow channel that enters the chamber is very small (extimated to be less than 0.01%) and the reactor chamber is not placed in the main flow channel (the one that exit through the first outlet). If the reaction chamber were placed in the main flow channel, the capillary could only sniff part of the flow and so only a part of the total amount of products it would have been detected.
µ-reactors with two kinds of capillary are available: one with a capillary of 5.6 µm width for small flow and one with 54.5 µm width for larger flow. In experiments where the backgrounds of the QMS signals are low, the detection limit can be as low as $5 \cdot 10^{10}$ molecules/s, equivalent to 10 ppm of the total flow through the capillary. The small volume of the reactor chamber divided by the flow of the capillary gives as result a residence time in the order of 2-3 s for the big capillary and 10 s from the small one. With this high time sensitivity it is possible to follow the measurements in real time and

to perform measurements faster than in a conventional batch reactor with a volume of hundreds of ml.
Another advantage of our device is that very small amount of catalyst is needed (typical loadings in the case of photocatalyst nanoparticulates are 20-60 μg) savings on synthesis time and material cost during the optimization of a catalysts or a screening study.
Furthermore, the small volume, as anticipated before, allows performing dangerous or potentially explosive reactions more safely. For example, according to the ideal gas law, only ~9.8 10^{-9} mol of gas can be accommodated in the reaction chamber at the pressure of 1 atm and temperature of 298 K. For the highly exothermic hydrogen oxidation reaction (inverse of eq. 1.2), the enthalpy of water (l) formation is -286 kJ/mol. Therefore, considering that we need 1 mol of H_2 plus half a mole of O_2 to make a mole of water, the heat released is ~2 mJ. This value is very small (1 kg of TNT releases ~4.184 MJ).
It is also worthy to mention that the high area-to-volume ratio and the relatively high thermal conductivity of the silicon chip allows a fast heat transfer to and from the chip. In this way, thermal gradients are strongly reduced, a better control of the temperature of the reactor is achieved and the temperature can be varied quickly.

2.2 Gas handling and controllers

The bonded μ-reactor is mounted in an aluminum manifold that is connected to the gas lines. The reactor is inserted into a slot of the manifold block and four Kalrez o-rings are placed in correspondence of the four holes of the chip. A metal bar with screws at the two ends is used to seal the system by pressings the reactor against the o-rings. Since air can leak through the material of the o-ring, especially when heated, argon is constantly purged on top of them, so that they are saturated by inert gas. In this way a sudden increase in temperature will only lead to a leak of argon.

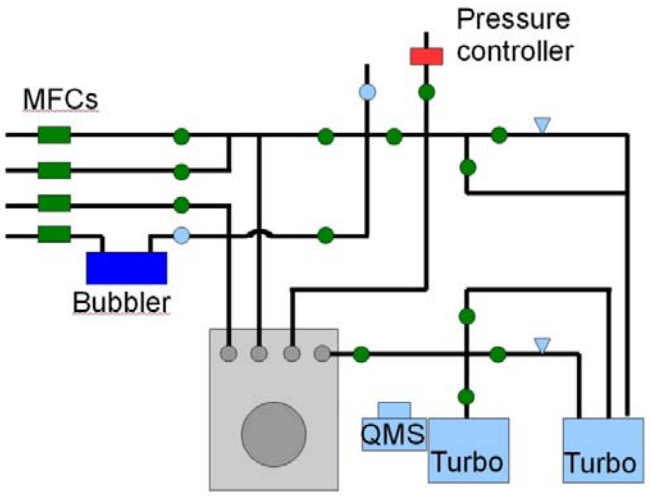

Fig. 2.4 Sketch of the setup. The green circles correspond to automatic valves, while the light blue to manual valves. Light blue triangles are used to indicate needle valves.

A scheme of the gas lines wall is shown in Fig. 2.4. Four gas lines can be connected to the setup and every one of them has a MFC. The top gas line has a branch structure (not shown in Fig. 2.4) that can redirect its flow to the other ones. The first two lines starting from the top mix together, forming the inlet line that is connected to the second inlet hole of the reactor. The other two gas lines form the inlet line connected to the first inlet hole. This setup was built by Peter C.K. Vesborg during is PhD. Some simple modifications, necessary to perform the water splitting reaction, were added during my PhD.

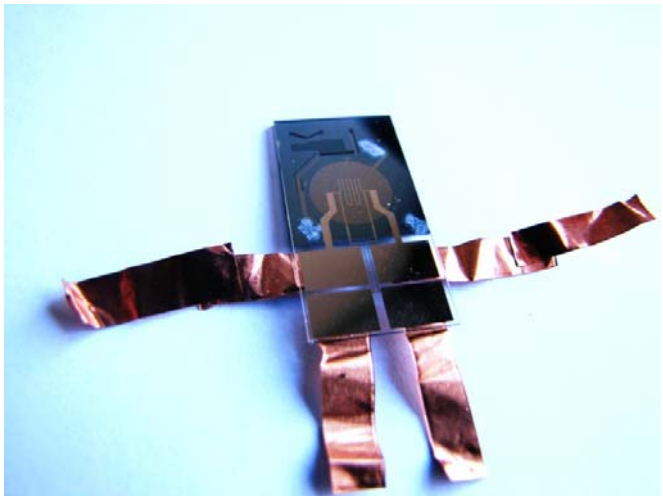

Fig. 2.5 Picture of the μ-reactor with a Pt resistance used for the four points resistance measurement.

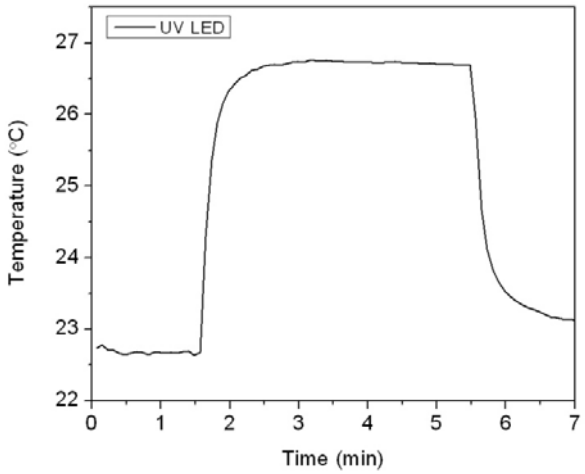

Fig. 2.6 Temperature increase as a function of time under illumination with a UV LED (Hamamatsu LC-L2, ~367 nm) at full power. This measurement has been obtained with the μ-reactor shown in Fig. 2.5. The light is switched on at ~1 min 30 s and switched off at ~5 min 5 s.

The first one was to add a bubbler that can be filled with water (or other liquid, i.e. ethanol). Flowing helium through the bubbler, the water vapor is carried to the reactor.

The partial pressure of the water vapor in the saturated helium flow is set by the temperature of the bubbler that can easily be measured with a thermocouple.

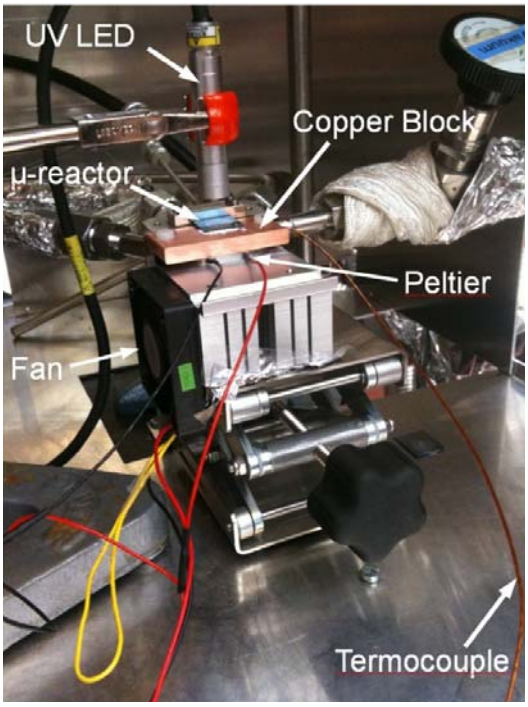

Fig. 2.7 Picture of the temperature controller placed under the μ-reactor mounted in the manifold block.

The second modification was to build a temperature controller for the reactor. A serious problem indeed was evident in my first experiments of overall water splitting. The water signal was increasing under illumination, particularly for samples with low or negligible activity. The reason of this behavior is that under illumination, the lamp heats the sample, causing the desorption of water molecules that were previously adsorbed on the reactor or/and the catalyst.
In order to estimate the increase in temperature caused by the light, a couple of experiments were performed together with my colleague Morten G. Nielsen. In these experiments, a μ-reactor with a special Pyrex lid was used. The lid was longer than a standard one and had an electrical circuit composed of a Pt resistance and 4 contacts sputtered on the surface (Fig. 2.5). After bonding, the Pt resistance remains sealed inside the reactor chamber, while the contacts extend out of the bonding area.
This device makes it possible to measure the heating indirectly with the measurements of the Pt resistance with the four point method. The experiment was performed connecting the contacts to a current supply and a voltmeter with copper tapes and wires. As light source, a high-power UV LED (Hamamatsu model LC-L2) assembled with a focusing lens (Hamamatsu L10561-220) was used. This is the light source that was used more frequently during my project. The UV LED spectrum has a peak in wavelength at ~367 nm and the FWHM is ~9 nm. The average irradiance on the sample area is ~460mW/cm^2, as measured using a photodiode (Thorlabs model S120VC). In Fig 2.6 the temperature is plotted as a function of time. The temperature rises fast when the

lamp is switched on (at t= 1.5 s), reaching a new stable value. When the light is switched off (at t = 5.5 s), the temperature decreases as expected. The increment in temperature during illumination is of 4˚C.
The heating and the consequent desorption of water is a problem for the measurements, especially in the case of water splitting reaction, where a decrease of water signal is expected. Furthermore, since water cracks into hydrogen and oxygen in the QMS, the increase of the water signal can induce an increase in the signal of hydrogen and oxygen that is not related to photocatalytic water splitting.
This problem was solved by placing a temperature controller in contact with the side of the μ-reactor made of silicon (Fig. 2.7). A silicone based thermal paste improves the quality of the contact, obtaining a good thermal conductivity between the chip and a copper block that constitute the top part of the temperature controller. The temperature is measured with a thermocouple placed in a hole in the copper block and compared to a value set in the Labview software. If the measured temperature is higher than the one set, then a Peltier cooler, placed below the block, is activated and the temperature controlled with a standard PID routine. The bottom part of the Peltier element becomes hot during the cooling operation, and this heat is removed by a fan of the model typically used to cool a cpu. A mini labjack is used to place the controller in close contact with the reactor.

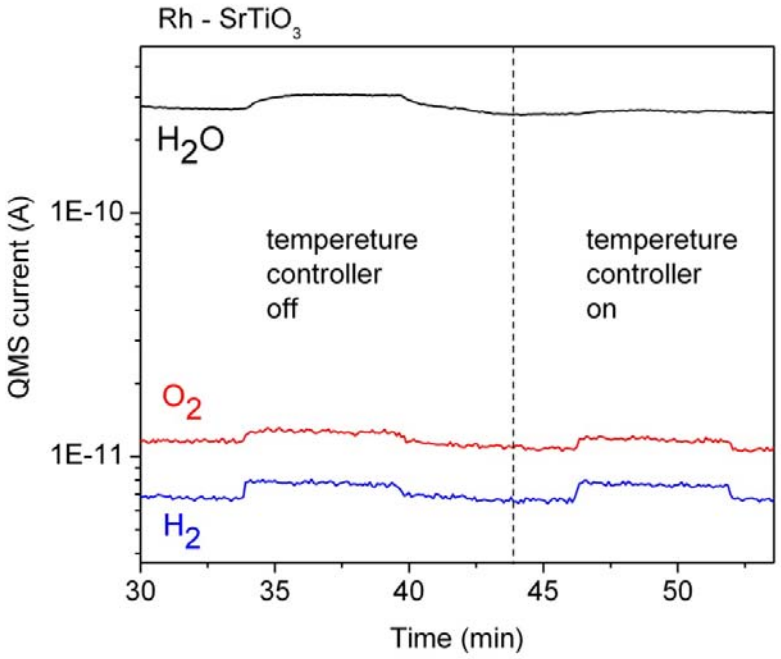

Fig. 2.8 QMS current for H_2 (m/z = 2), O_2 (m/z = 32) and H_2O (m/z = 18) as a function of time. The μ-reactor is loaded with Rh/$SrTiO_3$ catalyst. The UV LED (λ~367 nm) is switched on twice, with the temperature controller switched off and on respectively. Note the difference in the signal of H_2O.

The effect of the temperature controller during a photocatalytic water splitting measurement is shown in Fig. 2.8.

Apart from the bubbler and the temperature controller, other general improvements of

the setup were obtained and new software was written together with my colleague Morten G. Nielsen and under the supervision of Peter C.K. Vesborg. A picture of the setup is shown in Fig. 2.9.

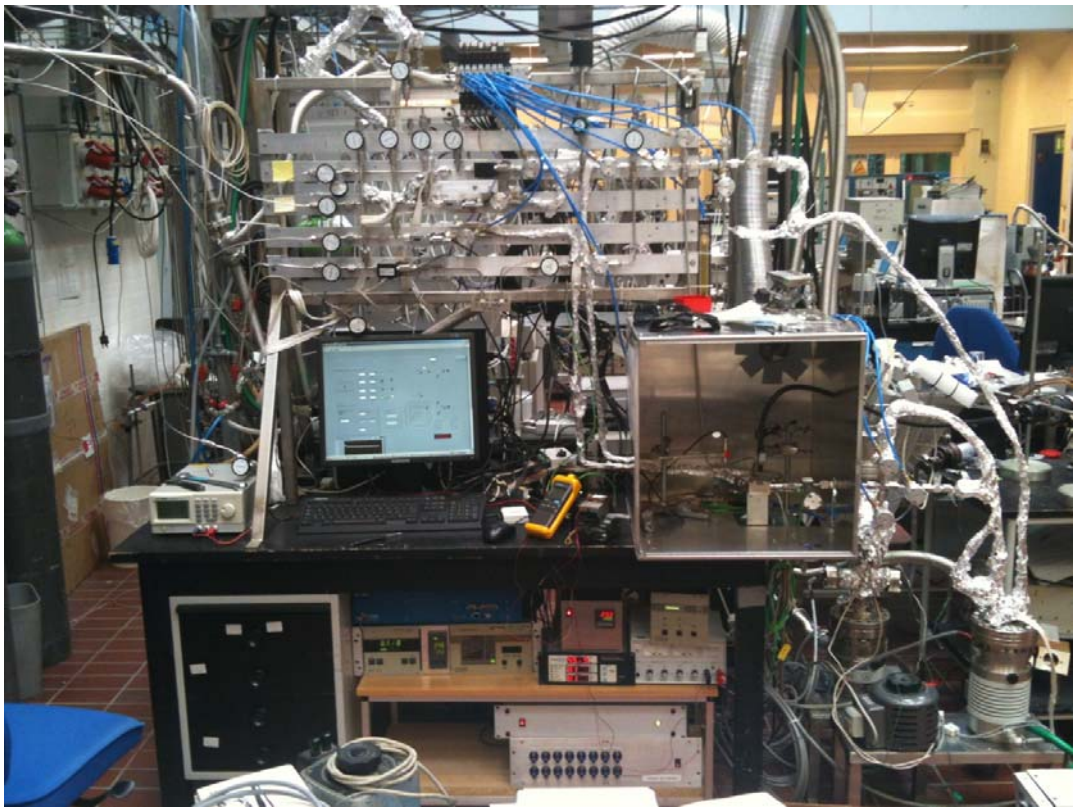

Fig. 2.9 Setup for photocatalytic experiments with μ-reractors (10/07/2012).

The valve between the reactor and the QMS and the valves that connect the gas lines to a roughing pump have been replaced by automatic pressure valves. The new valves are controlled by compressed air and can be in a binary state, open or closed. They can be interfaced with Labview, so that automated procedures, for example pump down sequences, can be programmed. Particularly important is the pump down sequence before opening to the QMS. In fact, every time a new chip is mounted, there is a volume filled with 1 bar of air between the capillary in the chip and the valve closing the line to the QMS. Previously, this volume was pumped by carefully opening a manual valve. This procedure is very delicate and time consuming. With the automatic valves the procedure is automated and just needs to be started by clicking a button in the Labview front panel. The pump down sequence last 10 min and after that the setup is ready to measure. This pump down sequence consists in 3 steps. In the first one, the valves are opened in a way that allows the gas at 1 bar to be pumped by a turbo pump through a needle valve with a fixed aperture. This valve limits the flow to the turbo and it is necessary because the automated valve can only be fully open or closed. After 5 min, the pressure is sufficiently low that the volume can be opened directly to the turbo pump. This second step also last 5 min. Finally, the volume is opened to the QMS chamber that is pumped with a dedicated turbo pump. In this last step the setup is ready

to measure. Using two turbo pumps allows reducing strongly the air contamination and the relative pressure variation to the chamber with the QMS, increasing the lifetime of the filament of the QMS. The extra turbo pump can be also used to pump down the gas lines with a similar procedure, reducing the possibility of oil contamination respect to the case when only the roughing pump was used. This procedure is used to pump down the lines between experiments with different gas flow composition (i.e. passing from water splitting to a CO oxidation experiment).

The program that controls the setup has been changed completely in order to use software more similar to the ones used by the other setups in my department. Starting from a model program developed by T. Andersen and R. Jensen and made portable by K. Nielsen, we implemented all the functions of our setup. Two programs are used: one of them controls the valves, the MFCs, the pressure controller, the pump down sequence and the temperature, while the second controls the measurements of the QMS and displays them in a plot vs. time.
A big advantage of the new software is that now the data are automatically saved online in a protected database. In this way, a backup is automatically created and the data are available to be accessed from the office without the need to be transferred with an USB stick.

2.3 Quadrupole mass spectrometer

A crossed beam QMS is used to detect products and reagent gases. Several gases can be measured in the same experiment, choosing different values of m/q, where m is the mass and q is the charge of the ionized gas. A typical measurement consists in monitoring the current of the ionized gases as a function of time.
It is possible to convert the currents (charges/time) in flows of molecules (molecules/time) with a calibration procedure previously described by our group [20]. The calibration procedure is fundamental to check the stoichiometry for a studied reaction. Indeed, since the ionization probabilities of gases are different, the ratio of the QMS currents for different gases produced in a reaction does not follow the stoichiometric value. During the calibration procedure for every gas, these ionization probabilities are implicitly taken into account. Therefore the ratio of the converted molecules flows should follow the stoichiometric value.

Chapter 3

Gas phase photocatalytic water splitting

3.1 Water splitting with materials only active under UV irradiation

As mentioned in the first chapter, many studies about photocatalytic water splitting have been published and reviewed in recent years [21, 22]. Most of the materials that have been found to be active for the overall reaction work only under UV irradiation. These photocatalysts are mainly metal oxides. They can be divided into two major groups: metal oxides consisting of d0 metal cations (mostly Ti^{4+}, Nb^{5+}, Ta^{5+}) and metal oxide consisting of d10 cations (mostly Ga^{3+}, In^{3+}, Ge^{4+}) [21]. They often present high stability, can be easily sinthesized and some of them are commercially available. A common feature of most of these semiconductor materials is that the dominant contribution to their valence band comes from the O2p orbitals that have a potential of about 3 V vs. NHE. The top of the valence band is too positive vs. NHE and is therefore considered to be the main limitation that has to be modified in order to push the absorption into the visible. However, even if they can absorb only a small or no amount of solar radiation the study of these materials is fundamental to understanding what determines a good photocatalyst, which modifications improve the activity and which strategies one should follow to extend the absorption of light to longer wavelength. For the above reasons and due to the amount of literature to which to compare the results we decided to start with these materials.

In order to investigate if it were possible to perform the experiments in gas phase, we performed a literature search for photocatalytic water splitting with water vapor. The exit of the search confirmed the possibility to run gas phase photocatalytic water splitting. However, we found out that almost the totality of papers in this field present results obtained suspending the particles in liquid water. Even though some papers on gas phase water splitting were published in the 80s the research moved towards the liquid case. This trend is understandable since the activity in liquid phase is higher than in gas phase, and therefore easier to detect [23]. Furthermore, for the same reason, a final device will probably work with liquid water. However we think that gas phase experiments have some advantages over liquid phase: some information can be easier or/and quicker obtained in gas phase experiments (see chapter 4 about photocatalytic water splitting and back reactions using the same sample) and it should be easier to interface the reactor with other setups with the goal to perform more in situ characterization and obtain precious information on the system (see chapter 5). Especially for UHV applications it is easier to separate the catalyst from the gas by pumping, than to collect the catalyst from a liquid environment. These advantages are important from a research point of view, but the possibility for a real application is also interesting to investigate. Indeed a gas phase device can be a potential application if the water that is present in the air, even in a desert where there is abundance of sunlight, can be used.

$SrTiO_3$ is a perovskite semiconductor with a bandgap of 3.2 eV and is a well known material [24]. Photocatalytic gas phase water splitting has been demonstrated by Domen et Al. in 1982 using $SrTiO_3$ loaded with NiO/Ni cocatalyst [25]. At the beginning of my PhD I worked with this material. The powder was purchased at Sigma-Aldrich (SrTiO3, 99.5% metal basis, product number 517011). The average particle size was found to be < 100 nm by the TEM images obtained by F. Cavalca (Fig. 1.8). No activity can be observed when $SrTiO_3$ is used alone, without cocatalyst. This fact is well known in literature and typical of almost all the photocatalyst, with exception of some with a very high bandgap (i.e. ZrO_2) [26]. Performing a preliminary screening where the $SrTiO_3$ nanoparticles were loaded with different cocatalysts hydrogen and oxygen evolution was detected when Pt was added. The procedure that I have followed to load the Pt is described in the paper of Liu et al. where it is applied to anatase TiO_2 [27]. The Pt is deposited on the $SrTiO_3$ by an impregnation method from an aqueous solution of $H_2PtCl_6 \cdot 6H_2O$. 0.2 g of $SrTiO_3$ powder was added to the desired amount of $H_2PtCl_6 \cdot 6H_2O$ solution (1mM Pt solution) in an evaporating dish at 60˚C above a water bath. During the initial stage of the evaporation the solution was constantly stirred with a magnetic rod and, in the final stage, manual stirring with a glass rod was used. After drying, the powder was collected and heated in air at 180˚C in an oven for 4 hours.

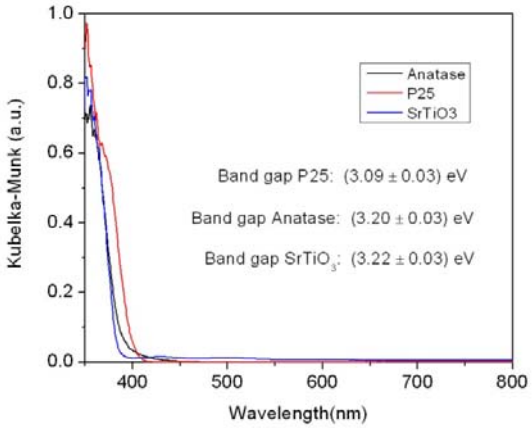

Fig. 3.1 Diffuse reflectance spectra of $SrTiO_3$, P25, anatase TiO_2.

Four samples with different Pt loadings were prepared according to this method: 0.5 wt%, 1 wt%, 2 wt% and 3 wt%. All of them were active for overall water splitting. Since this loading method was successful, application to other semiconductors was tried. Of particular interest was to see if it was possible to detect hydrogen and oxygen evolution for TiO_2, and especially for Degussa P25 (now Aeroxide® P25 from Evonik), the most famous commercial TiO_2, tested for many different photocatalytic reactions. Therefore, the same amount of Pt, 1 wt%, was loaded on $SrTiO_3$, P25 and anantase TiO_2 from Tayca Corporation. In Fig. 3.1 the Kubelka-Munk function (K.M.) is plotted. This is obtained from diffuse reflectance measurements by this equation:

$$F(R) = \frac{K}{S} = \frac{(1-R)^2}{2R} \tag{3.1}$$

and is the analogue of the absorbance obtained from a transmission measurement. R is the reflectance as measured in the experiments using a diffuse reflectance sphere and F(R) is the Kubelka-Munk function, often expressed as the ratio of the absorption and scattering coefficient, K and S.
The band gap is estimated by extrapolating the value at which the tangent to the onset of the K.M. function intercepts the x-axis. The value of 3.2 eV is obtained for $SrTiO_3$ and anatase while ~3.1 eV is obtained for P25 in fair agreement with the literature. One should notice that P25 is a mixture of anatase (78%), rutile and amorphous phase. Rutile has a band gap of 3.0 eV, so the presence of this phase slightly extends the absorption to longer wavelength. After the optical characterization, three reactors were prepared loading 40 μg for each sample. The activity of these samples were tested using the Hamamatsu UV-LED (λ_{peak} ~367 nm) and a Xenon lamp (1kW).

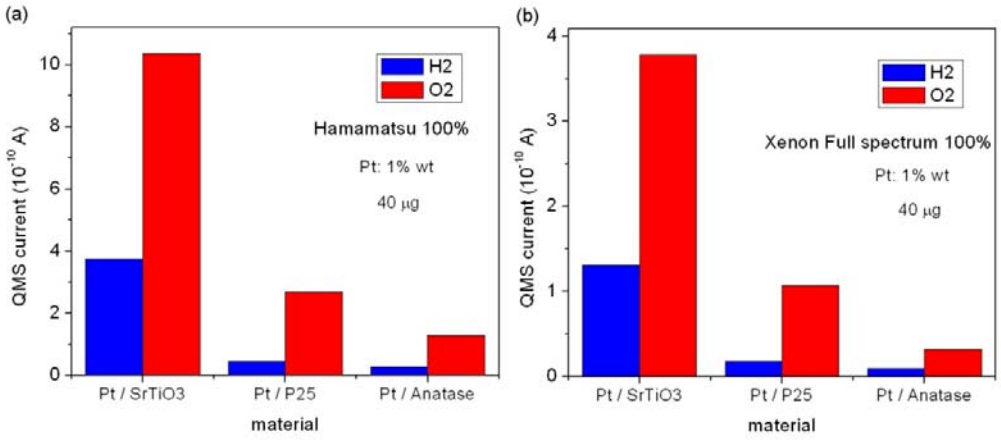

Fig. 3.2 Comparison of the rate for H_2 and O_2 photocatalytic evolution (expressed in QMS current) for 1 wt% Pt loaded on $SrTiO_3$, P25 and anantase TiO_2. The samples were illuminated by (a) an UV LED (~367 nm) and (b) the 1 kW Xe lamp.

The results are shown in Fig. 3.2. The activities obtained with the two light sources are similar. The first noticeable result of this experiment is that water splitting can be observed with TiO_2 anatase when loaded with Pt. Indeed as reported by Tabata et al., there was no unanimous consensus regarding the ability of Pt/TiO_2 to split pure water [28]. Overall water splitting with Pt/TiO_2 has only been achieved in few papers, but NaOH coating [29, 30] or the additions of alkali carbonate (especially Na_2CO_3) [31] was necessary in order to observe it. From the energy position of the bands, both anatase and rutile has a valence band much more positive than the H_2O/O_2 redox potential, so they could produce oxygen. However, the bottom of the conduction band of rutile is essentially at the same level as the H^+/H_2 redox potential while the one of anatase is slightly negative, by 0.20 eV (figure 3.20 of reference [32]). From these considerations, it seems extremely unlikely for rutile to be able to evolve hydrogen and thus to be active for the overall water splitting, while this can be possible for the anatase phase. The main reason of the difficulties in detecting overall water splitting with Pt/TiO_2 is probably that the high catalytic activity of Pt for the back reaction leads to a negligible net evolution of hydrogen and oxygen, since the evolved products are consumed before being detected. However it appears that our setup is sensitive enough to detect the

hydrogen and oxygen that does not undergo back reaction. Comparing the activity of the two TiO_2 samples, one can see that the activity of P25 is comparable but slightly higher than that of pure anatase. Since data for the crystallinity and BET area of the anatase samples are missing, it is difficult to attribute this difference to a specific cause. However, it is interesting to notice that P25 is often more active than a more pure anatase sample. This behavior is thought to be related to the synergy between the two phases, supported by the report by Zhang et Al. that the formation of a phase junction between anatase and rutile strongly enhance the photocatalytic activity [33].
The activity of the P25 is however surpassed by the one of $SrTiO_3$, which is almost 4 times higher. The high activity of $SrTiO_3$ over TiO_2 is often attributed to the higher conduction band of this material [21]. It is indeed known that $SrTiO_3$ photoanodes can split water without external bias [34]. Due to the higher activity this material was preferred as a model system during my PhD.
Studies on these UV light photocatalysts proved that our setup was able to detect the products of the photocatalytic water splitting reaction if the photocatalysts were prepared in the right way. Since the final goal of photocatalytic water splitting is to perform the reaction using solar light, we decided to move on and investigate materials with visible light absorption.

3.2 GaN:ZnO

GaN:ZnO is an oxynitride with visible light absorption, that can achieve overall water splitting [35, 36]. This result was first reported by Maeda et al. in 2005, and the overall water splitting was achieved after loading it with RuO_2 [37]. Together with $ZnGeN_2$/ZnO, GaN:ZnO is one of the few materials that are reported to work under visible light [38].

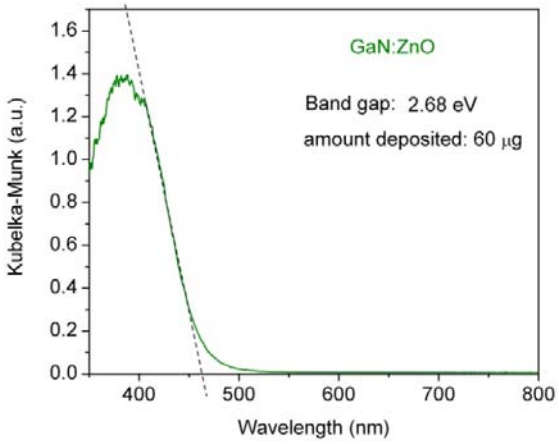

Fig. 3.3 Diffuse reflectance spectra of GaN:ZnO.

It has a d10 electronic configuration and it is obtained after nitridation of a mixture of β-Ga_2O_3 and ZnO nanopowder that has been carefully grinded and mixed in a mortar. XRD spectra showed that the material has a single phase wurtzite structure with (100) and (101) diffraction peaks at angles 2θ in between the ones of GaN and ZnO [37, 39]. These two semiconductors have both a wurtzite structure with similar lattice parameters.

From this observation, it has been proposed that the prepared GaN:ZnO is a solid solutions of GaN and ZnO instead of a physical mixture of the two. The optimized nitridation conditions depend on many factors and especially on the characteristics of the starting oxide materials, such as the size of the nanoparticles. Typical values for the optimized sample are a temperature of 1123 K, a flow of NH_3 of 250 $mL \cdot min^{-1}$ and a nitridation time of 10h [37, 39]. Calcination at higher temperature still produces GaN:ZnO but the obtained photocatalyst was less active, probably due to surface zinc defects. At lower temperature it was difficult to obtain a single phase material. Changing the nitridation time as well as the ratio of ZnO to β-Ga_2O_3 leads to materials with different band gap in the range of 2.4 – 2.8 eV, as estimated from the onset of absorption from diffuse reflectance measurements [39]. The change of the onset of the absorption corresponds to a change in composition of the photocatalyst. If we refer to the compound as $(Ga_{1-x}Zn_x)(N_{1-x}O_x)$, then the value of x can vary from 0.05 to 0.22. For high content of Zn, the absorption shifts towards longer wavelength. Fig. 3.3 shows a plot of the Kubelka-Munk function obtained from diffuse reflectance measurement that were collected with an optimized GaN:ZnO powder (x=0.12). The band gap is estimated to be 2.68 eV. It is interesting to notice that the highest activity is not obtained with the material that has the narrowest bandgap. Indeed short nitridation times give high Zn/Ga content and narrow band gap but low crystallinity, while long nitridation time can cause sintering or creation of defect due to zinc volatilization. So the best catalyst seems to be found for conditions somewhere in between extremes [39]. A reduction in the density of zinc defects and the related oxygen defects has been achieved by Maeda et al. with post calcination in air at the temperature of 550 °C (823 K) for 1 h of the as made GaN:ZnO [40]. The elimination of these defects that act as traps between photogenerated electrons and holes, results in an improvement in activity when the material is loaded with $Rh_{2-y}Cr_yO_3$ (1 wt% Rh, 1.5 wt% Cr).

The origin of the visible light absorption of the GaN:ZnO has been investigated in literature and it is very interesting considering that GaN and ZnO has a band gap of 3.4 eV and 3.3 eV respectively.

A first explanation was reported by Maeda et al. [37] and relies on the p-d electron orbital repulsion. This mechanism has been described for II-VI semiconductors, which are materials that have a cation metal d subband inside the valence band [41]. The repulsion of p and d orbitals raises the maximum of the valence band without changing the conduction band position with the consequence of reducing the band gap. In the case of GaN:ZnO, the repulsion between Zn3d and N2p is suggested to reduce the band gap with respect to the one of GaN. This explanation was based on calculations performed with density functional theory (DFT) that predicted that the contribution to the bottom of the conduction band for GaN:ZnO is mainly due to 4s and 4p orbitals of Ga, while the top of the valence band consists of N2p and Zn3d orbitals. However the explanation can be more complex. Indeed, a photoluminescence (PL) spectroscopy study by Hirai et al. has shown the presence of luminescence bands for GaN-rich $(Ga_{1-x}Zn_x)(N_{1-x}O_x)$ with x=0.05-0.20 [42]. Their energy position can be attributed to impurity energy levels in the band gap. Therefore, the visible absorption can have its origin in the transitions of electrons from Zn acceptor levels to the conduction band or to unfilled O donor levels. The mechanism predicted by DFT could still be valid for a stoichiometric solid solution. However, the observation of the PL signals can be compatible with another explanation. According to soft x-ray emission and absorption spectroscopy measurements, McDermott at al. proposed a model in which the GaN:ZnO is described as a

heterostructure of GaN and ZnO with two optical gaps at 2.6 eV and 2.8eV, respectively [43]. These gaps are obtained at the interface between the two materials, and arise from the repulsion of the conduction bands and not from an increase in the valence band maximum. This repulsion leads to conduction band states that are more negative in energy than the conduction band of GaN, while in the p-d model the conduction band of GaN:ZnO is almost at the same level as the one of GaN. Finally, it should be mentioned that in the same work, the authors also showed that the surface of GaN:ZnO consists in a surface oxide layer of Ga_2O_3. Since in this study the authors didn't find any evidence of increased valence band maximum or features that can attribute the visible light absorption to Zn acceptor levels it is considered to show the most probable nature of the "real" GaN:ZnO (at least in the composition range examined).

3.3 Overall water splitting

As discussed in the previous paragraph, GaN:ZnO is an interesting candidate for solar light photocatalytic water splitting due to the fact that it can split pure water into hydrogen and oxygen using visible light when loaded with an appropriate cocatalyst. This system has been studied extensively with the photocatalyst suspended in liquid water. The activity has been tested loading the material with many cocatalysts i.e. RuO_2, noble metals, metal-chromia mixed oxides [44] and metal/chromia core/shells [45]. However to our knowledge, no gas phase photocatalytic water splitting investigations were previously done with a material with visible light response or with any oxynitrides and nitrides. Among the various cocatalysts analyzed, the Rh-Cr mixed oxide seems to be the most active [46]. For these reasons, we started a collaboration with the group of prof. Kazunari Domen from the university of Tokyo that consisted in testing $Rh_{2-y}Cr_yO_3$/GaN:ZnO nanoparticles produced in their lab in Tokyo by prof. Kazuhiko Maeda and Anke Xiong with our μ-reactor system.
The main part of this paragraph is based on my article in Energy and Environmental Science [47] (attached in the end of the thesis).

Catalyst preparation

For this work GaN:ZnO was prepared by nitridation of β-Ga_2O_3 (0.73 g) and ZnO (1.27 g) powders under NH_3 flow (250 mL min^{-1}) at 1123 K for 10 h. The as-synthesized GaN:ZnO powder was then subjected to post-calcination in a static air atmosphere at 873 K for 1 h. The Rh-Cr mixed oxide was prepared by impregnation of GaN:ZnO (0.1g) from a 3-4 ml solution of $Na_3RhCl_6 \cdot nH_2O$ (Rh 17.8 wt%) and $Cr(NO_3)_3 \cdot 9H_2O$ placed in an evaporating dish over a water bath. The suspension was stirred using a glass rod to complete evaporation. The resulting powder was collected and heated in air at 623 K for 1 h. To test this material, a reactor with 20 ± 10 μg of catalyst was prepared. The catalyst was deposited by drop casting a solution of $Rh_{2-y}Cr_yO_3$/GaN:ZnO that was prepared with the powder and Millipore water. The maximum amount of catalysts that can fit in the chamber can be calculated once the packing density is known. This amount is not to be confused with the material density, and can be obtained by weighting a known volume of the powder material. For this sample the value of ~836 g l^{-1} was obtained. Since there were no literature references for this value, the same

procedure was used to determine the packaging density of P25 and compared this to the value reported by the company Evonik that now produces the P25. A value of 139.7 g l^{-1} was obtained, which is in good agreement with the value of 130 g/l reported, confirming that the measurement for GaN:ZnO should be reasonable. For GaN:ZnO, knowing that the reactor volume is 240 nl, one obtains an estimated maximum loading of 200 µg. Bonding the reactor with such a large amount of material would be almost impossible, and that value has to be considered a maximum limit. In fact usually, the material is not deposited on the entire area of the reactor chamber. A mask with a diameter smaller than the diameter of the chamber is used in order to avoid that particles very close to the edge will end up on a part of the reactor that has to be sealed. Furthermore, if the deposited layer is higher than the reactor depth, some loose particles can also scatter away from the reactor area after pressing the lid with the silicon during the bonding, causing a failed bonding. For these reasons a smaller and more reasonable loading was chosen.

Solar activity

In Fig. 3.4 is shown a measurement obtained using a simulated solar spectrum.

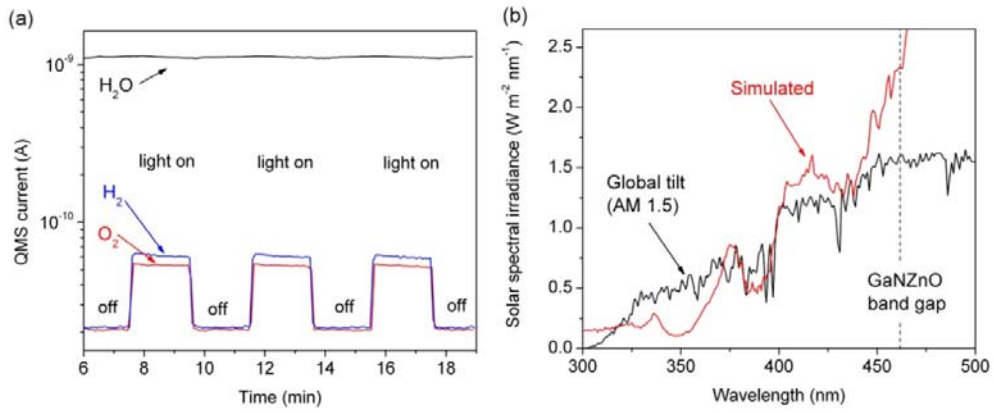

Fig. 3.4 (a) QMS current for H_2 (m/z = 2), O_2 (m/z = 32) and H_2O (m/z = 18) as a function of time. Three cycles of illumination are shown. The lamp used simulates the solar spectral irradiance for AM 1.5 for $\lambda <$ 462 nm. (b) The irradiance by the light source used in the experiment compared to the global spectral irradiance on the 37° sun facing tilted surface for an absolute air mass of 1.5. The integrated irradiance from 300 nm to 462 nm (= 2.68 eV) is equal to 126 W/m^2 for the solar spectrum and 132 W/m^2 for our lamp. Figures adapted from [47].

A Xe-arc lamp was equipped with a neutral density ND0.5 filter, a water filter and an AM 1.5 filter in order to simulate the solar spectrum in the range of wavelengths that can be absorbed by the GaN:ZnO. The global spectral irradiance on the 37° sun facing tilted surface for an absolute air mass of 1.5 as defined by American Society of Testing and Materials (ASTM G173) and our simulated solar irradiance is shown in Fig. 3.4b. The integrated irradiance from 300 nm to 462 nm (~2.68 eV) is equal to 126 W/m^2 for the solar spectrum and 132 W/m^2 for our lamp. The temperature of the experiment was set to 22˚C (295 K) and the partial pressure of water to 21 mbar. In Fig. 3.4a, the signals of H_2 and O_2 clearly rise when the light is switched on, and drop when it is switched off

(three cycles, with two minutes of light on and two minute of light off for each cycle). With the low light intensity used in the previous experiment it is very difficult to see a decrease in the water signal upon illumination. It will be shown later that this is possible with a different light source.

Visible activity

In order to confirm that the activity seen with the solar simulator is not only due to a contribution from the UV wavelength, an experiment was performed with blue/violet illumination. The light source was an array of 4 laser diodes (Sharp GH04P21A2GE) with a wavelength of λ=406 nm and FWHM of ~1 nm. Another experiment was performed with the Xe lamp with cut-off filters for shorter wavelengths.

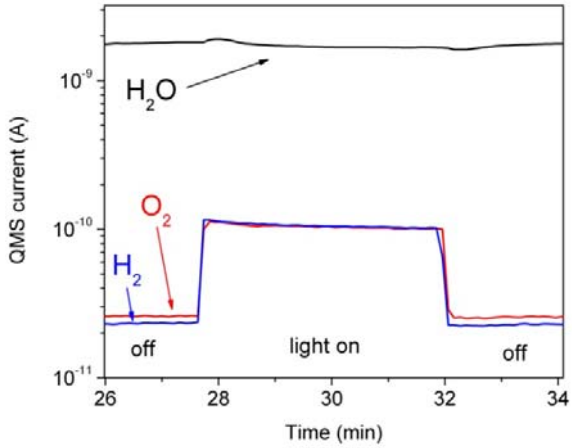

Fig. 3.5 QMS current for H_2 (m/z = 2), O_2 (m/z = 32) and H_2O (m/z = 18) as a function of time (blue/violet diode laser array, λ ~ 406 nm, ~ 180 mW/cm^2, ~ 4 minutes light on). Figure adapted from [47].

The result of the first experiment is shown in Fig. 3.5 and confirms that the material is active in the visible range. The second experiment (not included in the article) is shown in Fig. 3.6. For every filter two cycles of illumination were performed. The first set is actually only the Xe lamp without any filter. Then the filters are cutting off more and more of the shorter wavelength from 280 nm, 400 nm, 420 nm, 435 nm and 515 nm. The difference between this experiment and an action spectrum is that in that case narrow band filters are used, while here short wavelength cut off filters were used. The result is consistent with the diffuse reflectance measurements, and activity can be detected even with a 420 nm cut off filter. No activity is detected for wavelength longer than 515 nm as expected, since the material is not absorbing at those wavelengths.

Activity vs. light intensity

The experiment presented in the previous section shows also the stronger activity of the material under UV light illumination. Indeed if we use a light source with a higher intensity and in the UV-range, where the absorption of the material is higher, it is even

possible to see a drop in the water signal (Fig. 3.7). This decrease of the water signal is a further proof that the evolved hydrogen and oxygen molecules are coming from the decomposition of water. The detection of the decrease in water signal is almost impossible to achieve with a powder suspension in a conventional liquid phase batch reactor, because it will require running an experiment over very long time, making the experiment extremely unpractical. In our case, the decrease occurs immediately after illumination and its dependence on light intensity can be resolved.

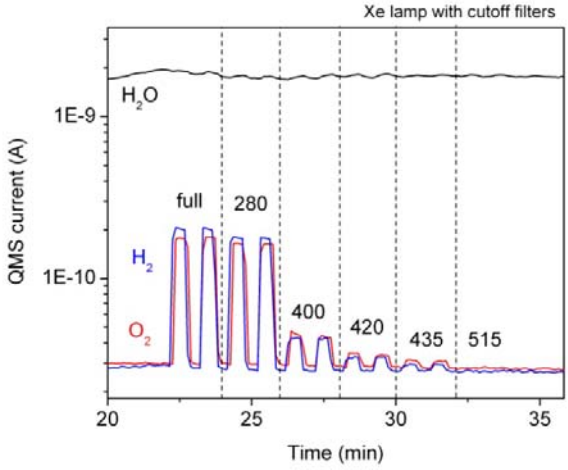

Fig. 3.6 QMS current for H_2 (m/z = 2), O_2 (m/z = 32) and H_2O (m/z = 18) as a function of time. The 1kW Xe lamp with cutoff filters has been used in this experiment (two cycles of illumination for each filter). The numbers in the figure refer to the nominal cutoff wavelength of each filter. The first two cycles are performed using the lamp without filters (full spectrum).

To investigate this aspect as well as the dependence of hydrogen and oxygen evolution with light intensity, several experiments were carried out using the high intensity UV LED.

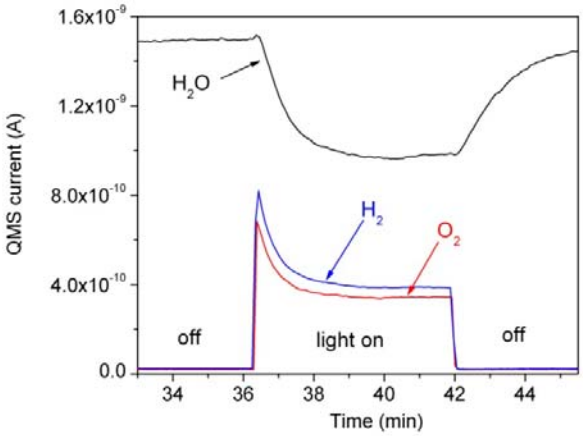

Fig. 3.7 QMS current for H_2 (m/z = 2), O_2 (m/z = 32) and H_2O (m/z = 18) as a function of time (UV LED, $\lambda \sim 367$ nm, ~ 460 mW/cm^2, ~ 4 minutes light on). Figure adapted from [47].

This is particularly suitable for this kind of experiment because its intensity can be changed electronically with a program written in Labview from 100% to 10%, and its high intensity makes it possible to measure photocatalytic activity two or three orders of magnitude in light intensity by inserting ND filters. In the following experiment a ND1.0 filter was used in order to go down to 1% of intensity. The sample was illuminated for 5 min for each intensity and the light was switched off for 5 min between every measurement. The shape of the raw signal during illumination is similar to the one reported in Fig. 3.7, where the activity is high at the beginning of the illumination and decays to a stable value within ~30 s.

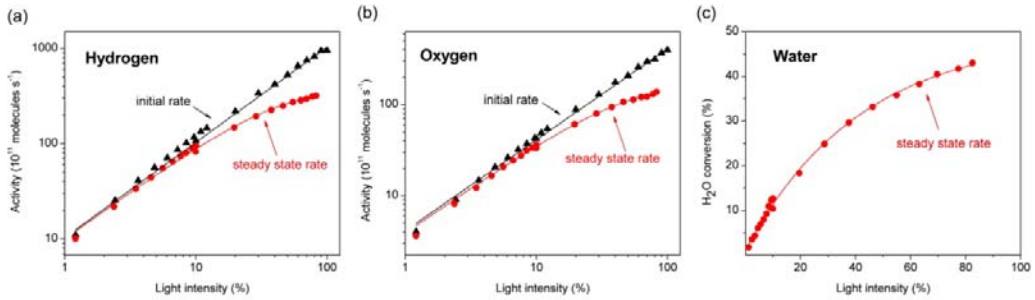

Fig. 3.8 Rate of H_2 (a) and O_2 (b) evolution for gas phase water splitting as a function of light intensity (UV, λ~367 nm, 100% of light intensity ~460 mW cm^{-2}). The initial rate (triangles) and the rate achieved after 5 minutes of illumination (circles) are plotted for both the products. The corresponding H_2O conversion is plotted in per cent (c). Figures adapted from [47].

The initial rate values as well as the values after 5 minutes, just before the light off, are plotted in Fig. 3.8a-b for H_2 and O_2 evolution. In Fig. 3.8c the water conversion is plotted in per cent. Notice that a conversion up to 43% is obtained at the maximum light intensity (460 mW cm^{-2}). The decay of the signal for hydrogen and oxygen can be ascribed to two primary contributions.

The first is the decrease in output light intensity of the LED as a function of time due to self-heating of the LED. The intensity of the UV LED as a function of time was measured to estimate this contribution, cycling it with the same period as in the water splitting experiment. It was found that the intensity decreased ~15% at full power in the worst case. This effect has been taking into account in plotting Fig. 3.8a-b, scaling the x-axis of the steady state points. This correction is the reason why these points have a value of x lower than the initial points corresponding to the same experiment. At the time of my writing of this thesis, this correction is no longer necessary because we are using a mechanical shutter between the LED and the sample. However, even after the correction, there is still a difference between the initial peak values and the steady state ones. The initial rate shows a linear behavior as a function of light intensity, while the rate after 5 min of illumination tends to level off at high intensity.

Our result for the initial rates is in agreement with the linear dependence of the gas activity as a function of the light intensity that has been observed in liquid phase for low intensity up to $1 \cdot 10^{22}$ photons h^{-1} [48]. Hisatomi et al. calculated the number of particles used in their experiment to be $\sim 1.2 \cdot 10^{13}$. This corresponds to having 10^5-10^6 photons s^{-1} $particle^{-1}$. In our case, the maximum intensity is $4.4 \cdot 10^{20}$ photons$\cdot h^{-1}$ and the maximum number of particles, calculated using the same procedure of Hisatomi et al., is $2.3 \cdot 10^{10}$.

Therefore, the rate of photons per particles is roughly 10^6 photons s^{-1} $particle^{-1}$, so in a similar regime as the mentioned work.
The second reason that leads to the difference between the peak points and the stable points is related to the decrease of the coverage of water on the active sites. During illumination we move from the limit of zero conversion, where the water coverage is θ, to an equilibrium where the water coverage is now θ'< θ.

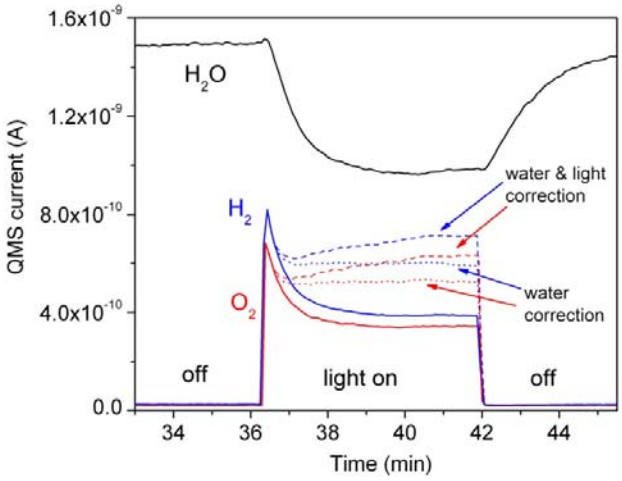

Fig. 3.9 Correction due to the H_2O consumption for the H_2 and O_2 QMS signals of Fig. 3.7 (dotted lines) and the further correction due to the light intensity decay (dashed lines). Figure adapted from [47].

This equilibrium is determined by the rate of the reaction and by the fact that, during the reaction, the water is consumed and needs to readsorb. At high light intensity, the decomposition of water is fast, which is reflected in the decrease in water partial pressure that can be seen in Fig. 3.8c. Thanks to the fact that the water signal is monitored, an attempt has been made in order to correct for this effect (Fig. 3.9). The signals of hydrogen and oxygen have been multiplied by the ratio of the currents H_2O^{dark}/H_2O^{light}, and further by the ratio of light intensity $\Phi(t = 0)/\Phi(t)$, where *t* is the time during which the light is on. As can be seen in Fig. 3.9, the value corresponding to the initial peak is almost completely recovered when the two corrections are added.

Activity vs. water partial pressure

The dependence of the activity on the partial pressure of water can be monitored directly diluting the flow of wet helium with dry helium. In Fig. 3.10, the evolution rate of H_2 and O_2 are plotted as function of water partial pressure. The bubbler was at a temperature of 20.3˚C (293.5 K), corresponding to a water partial pressure p_{H2O} of 23 mbar for the saturated flow. The temperature of the μ-reactor was kept constant at 25˚C (298 K). A linear behavior is obtained in the range of partial pressure examined for both hydrogen and oxygen. It is remarkable that a finite activity can even be detected at a water partial pressure as low as 2 mbar. This result could be very interesting for the realization of a gas phase photocatalytic water splitting device in the desert area. In these areas there is abundance of solar light and, despite the lack of liquid water and the dry soil, there is a reasonable level of water partial pressure in the air. During the

summer time for example, in the deserts of south-western USA, there is a partial water pressure of 10–12 mbar, which is relatively constant (the dew point is 5–10 ˚C, 278–283 K). However we will see that the dependence of the gas evolution rate is more complex, and will lead to more trouble in the realization of such a device.

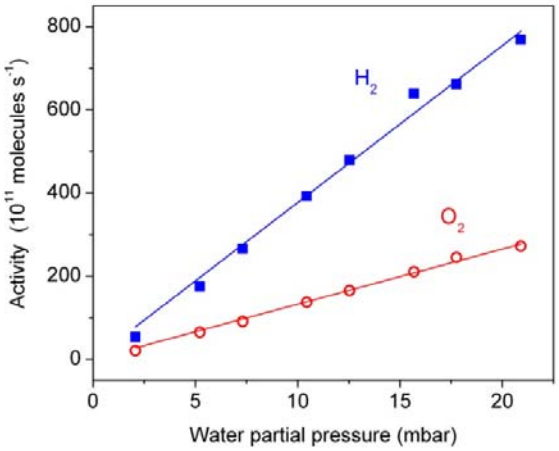

Fig. 3.10 Initial H_2 and O_2 evolution rate for gas-phase water splitting as a function of the water partial pressure. Temperature of 25 ˚C (298 K), UV LED at λ~ 367 nm (~460 mW cm^{-2}). Figure adapted from [47].

Activity vs. temperature

In Fig. 3.11 the initial gas evolution rate is plotted as a function of the temperature of the reactor.

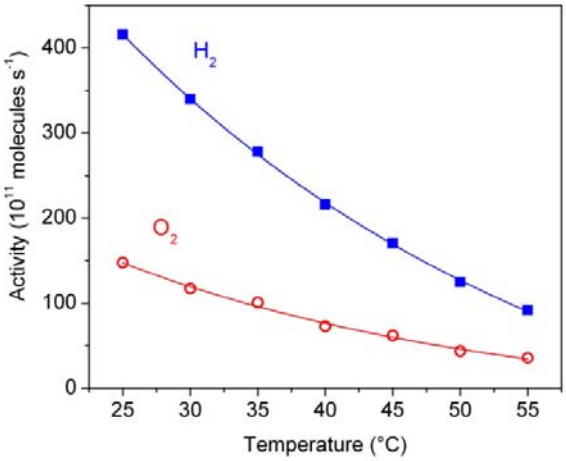

Fig. 3.11 Initial H_2 and O_2 evolution rates for gas phase water splitting as a function of temperature (298–328 K). (UV LED, λ~ 367 nm, ~230 mW cm^{-2}, H_2O = 21 mbar). Figure adapted from [47].

These results were obtained from a set of measurements where the light intensity of the UV LED and the temperature of the bubbler were kept constant (and so the water partial pressure) while changing the temperature of the reactor from 25 ˚C to 55 ˚C (298 to 328 K) in steps of 5˚C. The temperature was measured with a thermocouple and kept constant with a Peltier element. The activity clearly decreases while increasing temperature. This experiment also emphasizes how important it is to keep the temperature controlled in the other experiments in order to have reproducible results.

Relative humidity

The observed decrease in activity can be explained if the activity is dependent on the relative humidity.

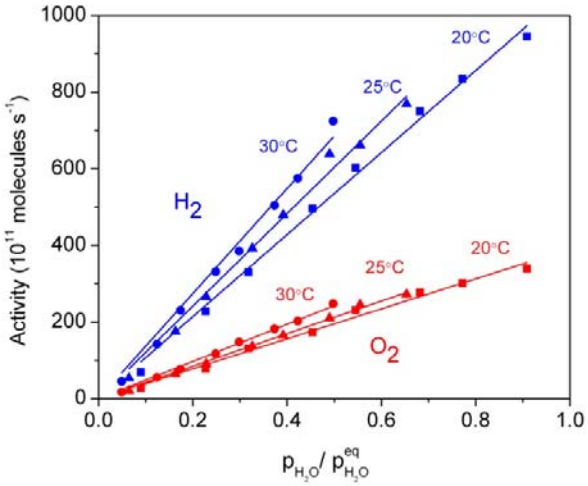

Fig. 3.12 Initial H_2 and O_2 evolution rate for gas-phase water splitting as a function of relative humidity (water partial pressure divided by the water equilibrium vapor pressure). Three sets of data points are plotted corresponding to experiments made at the temperature of 20 ˚C (293 K) (squares), 25 ˚C (298 K) (triangles) and 30 ˚C (303 K) (circles). (UV LED, λ ~ 367 nm, ~460 mW cm^{-2}.). Figure adapted from [47].

The relative humidity is determined by dividing the water pressure, p_{H2O}, by the equilibrium vapor pressure of water, p^{eq}_{H2O}, at the temperature of the µ-reactor. Therefore, the relative humidity will drop when the temperature of the reactor is increased. To further check this hypothesis a set of experiments were carried out changing the water partial pressure, while keeping the temperature constant. The experiments were repeated for three different temperatures, 20 ˚C, 25 ˚C and 30 ˚C (293, 298 and 303 K). These temperatures correspond to p^{eq}_{H2O} of 23 mbar, 32 mbar and 42 mbar, respectively. The results are shown in Fig. 3.12, where the gas evolution rate is plotted as a function of the relative humidity, p_{H2O}/p^{eq}_{H2O}. Apart from a small deviation, the data lie on the same lines. The linear dependence observed can be condensed into the formula for the gas evolution rate r:

$$r(t) \propto \frac{p_{H2O(t)}}{p^{eq}_{H2O}(T)} \tag{3.2}$$

In order to check that also the data obtained in the experiments for the activity as a function of increasing temperature were changed, the data shown in Fig. 3.11 have been replotted as normalized reaction rate $r \cdot p_{H2O}^{eq} / p_{H2O}$ and shown in Fig. 3.13 as a function of temperature. The figure confirms that the strong temperature dependence of the activity observed in Fig. 3.11 is mainly due to the change in relative humidity as a consequence of the change of temperature. This figure also confirms a further weak temperature dependence also shown in Fig. 3.12. This weak dependence is showing that the activity slowly increases, raising the temperature in the range between 25 ˚C and 45 ˚C. The same tendency is also observed for the stable value after 5 min. Hisatomi et al. studied the temperature behavior in liquid phase in the range of temperature between 2 ˚C (275 K) and 48 ˚C (321 K). They also found an increase in the activity with increasing temperature and calculated an apparent activation energy of 7.6 ± 2.4 kJ mol^{-1}.

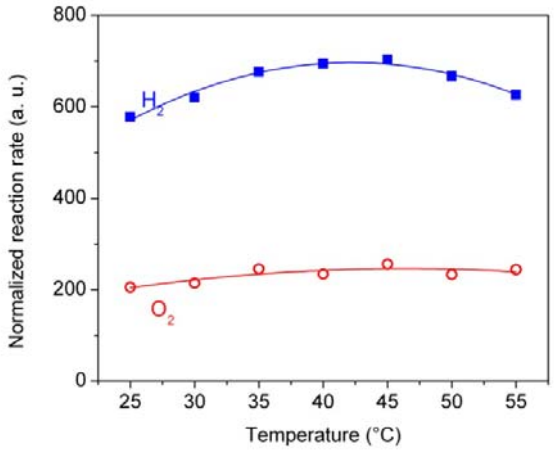

Fig. 3.13 Initial H_2 and O_2 evolution rates reported in Fig. 3.11 multiplied by the factor p_{H2O}^{eq} / p_{H2O} as a function of temperature. Figure adapted from [47].

Since our temperature range is included in the one studied by Hisatomi et al., I have also calculated the apparent activation energy constructing an Arrhenius plot from the data of H_2 evolution from figure Fig. 3.13 in the range from 25 ˚C to 45 ˚C. A value of 8.0 ± 1.4 kJ mol^{-1} is found, similar to the value of Hisatomi et al. Notice that constructing the Arrhenius plot from the data in Fig. 3.13 instead of the data in Fig. 3.11 we have taken out the contribution of relative humidity. In this way, the limiting effect of the relative humidity on the activity does not contribute to the activation energy that we have calculated. This is based only on the remaining contributions to the dependence on the temperature that we have observed. Furthermore, the calculated value is just a rough estimate valid for low temperature. In the present experiment, the temperature behavior deviates from the Arrhenius plot for temperatures higher than 40 ˚C. In particular for higher temperatures (the points at 50 ˚C and 55 ˚C), the activity even slowly decreases. This drop in the activity at higher temperature can be due to an increase in the rate of electron-hole recombination when the temperature is increased.
The dependence on relative humidity that we have seen explains well the temperature behavior of the activity and can also explain the behavior upon changing the partial

pressure of water. Indeed, the linear dependence of the data in Fig. 3.10 are explained by the formula 3.2, since in that experiment the temperature of the reactor and so p_{H2O}^{eq} was kept fixed. If we add also the dependence on light irradiation, that we have seen to be linear for the initial rates, we obtain a relation for the rate of gas evolution:

$$r(t) = k(\lambda, T)\Phi(t)\frac{p_{H2O(t)}}{p_{H2O}^{eq}(T)} \quad (3.3)$$

where r is the reaction rate, k(λ,T) is a parameter dependent on wavelength and temperature, including the weak temperature dependence that is not due to a change in the relative humidity, and Φ(t) is the light irradiance.
The dependence on the relative humidity can be explained on the microscopic scale when considering the mechanism of overall water splitting. It is known that the hydrogen evolution site is the $Rh_{2-y}Cr_yO_3$ cocatalyst, while the oxygen and the protons are produced at the surface of GaN:ZnO by oxidation of adsorbed H_2O* molecules or other intermediates (OH^-*, OOH*, ...) [49]. The surface conduction of protons is playing an important role in connecting the two half reactions.
In liquid phase, the conduction of protons to the cocatalyst is easy in acidic pH, where there is a reservoir of protons. In gas phase, this conduction is improved by increasing the relative humidity. More water is adsorbed when the relative humidity is increased and, in this way, the proton mobility is also increased [50].
The activation energy observed for proton mobility in water (2-3 kcal kJ mol^{-1}, 8-12 kJ kJ mol^{-1}) is in agreement with the small activation energy that we have found [50]. Many factors may contribute to the value that we have calculated, such as the transport and annihilation of electron–hole pairs, the detailed reaction mechanism of splitting water, and the oxygen and hydrogen evolution processes, so one should be careful on drawing conclusions from the comparison of this value. The only acceptable conclusion is that if the proton mobility is the limiting factor, then our calculation is in agreement with this hypothesis.
The importance of the relative humidity for a gas phase water splitting device has also been shown by Spurgeon at al. in a gas phase electrolyzer, where the two electrodes are connected with a PEM membrane [51]. The work by J.M.Spurgeon and N.H.Lewis appeared in the same edition of Energy and Environmental Science as my article, and also in their case, the lower electrolysis current density was attributed to “dehydration of the PEM at reduced relative humidity values”, and thus to a worse proton conduction.

Flash desorption experiments

To further investigate the role of relative humidity it was tried to quantify the amount of adsorbed water molecules as a function of the relative humidity. The main interest was to see if there was see a linear correlation between the activity and the amount of water adsorbed, and to estimate the water coverage at different relative humidity. As a first attempt, a series of experiments of flash desorption were performed. In these experiments, the relative humidity was set by keeping the temperature of the reactor and the partial pressure of water constant. Then the reactor was heated with a heat gun (temperature in the range of ~140-150 ˚C) for 15 s at each value of relative humidity. Different values of relative humidity were obtained changing the water partial pressure. The reactor was loaded with similar amount of catalyst as the one used for the

previouslty discussed photocatalytic experiments. After every heating sequence, the reactor was cooled down to the same temperature (25 ˚C). During the heating, a peak in the water signal was formed which was integrated in the analysis of data. The same experiment was repeated for an empty reactor. The results are shown in Fig. 3.14.
The data display the clear s-shaped isotherm expected from BET theory with the central part at intermediate relative humidity that can be approximated with a linear behavior [52, 53]. However, the values of the empty reactors, that should represent the subtracting background, are overlapping with the ones of the reactor loaded with the catalyst.

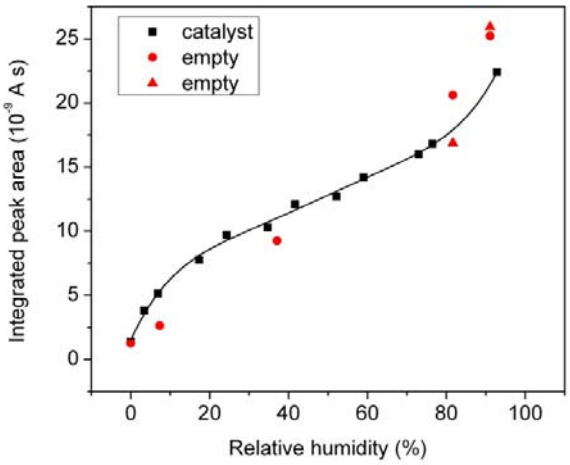

Fig. 3.14 Integrated water desorption peak as a function of relative humidity. The black square data points are obtained with the reactor loaded with $Rh_{2-y}Cr_yO_3$ /GaN:ZnO, while the red circles and triangles with an empty reactor. The water desorption peak was obtained with a heat gun at ~140-150 ˚C for 15 s and they are directly proportional to the number of H_2O molecules adsorbed.

A possible explanation is that in this experiment the heating is propagating to the entire reactor and to the manifold block thanks to the good thermal conductivity of the silicon. In this case we might lose sensitivity, since in principle we would like to heat only the catalyst or at least the reactor chamber. Furthermore even in that case the geometrical area of the reactor chamber plus the channel leading to the QMS is 1.59 cm^2, while the one of the entire reactor is 2.29 cm^2. This is comparable with the area of our catalyst since, as previously reported, it is about 8 $m^2 g^{-1}$ and so 2-4 cm^2 in the case of our loading. A preliminary attempt to repeat that experiment using more catalyst and a different heating technique based on a heating cartridge has been done. However, due to the lack of time and upcoming new interesting projects, we have decided to stop these experiments. An experiment with automated changing of water partial pressure and heating sequence will be necessary for these experiments to be realised.
Interesting results regarding the correlation of adsorbed water, relative humidity and proton conduction was obtained by Tejedor-Tejedor et al [54]. Their samples consist of wafers of nanoporous anatase TiO_2 that were previously immersed in a solution of pH 1.5 in order to protonate the surface. The proton conductivity is measured by electrochemical impedance spectroscopy using alternate current between two sputtered electrodes. Their results clearly show that for their samples the proton conduction increases with the relative humidity and is correlated to the adsorbed water (water

content). The relation between proton conductivity and relative humidity show an s-shaped behavior that can be approximated with a linear behavior between 20 and 80 % of relative humidity. Their findings seem to support our suggestions.

Stoichiometry and quantum efficiency

While in the liquid phase under optimal conditions the ratio between the evolved hydrogen and oxygen molecules is stoichiometric, in our gas phase experiments, the conversion of the QMS signal in flow of molecules seems to be always higher than the stoichiometric ratio up to ~2.5 in the worst case. This observation can possibly be explained by an oxidation of something in the μ-reactor. The holes can oxidize the nitrogen in the catalyst to N_2. Small amounts of N_2 evolution has been observed in liquid phase only in the first couple of hours of reaction [49]. However, we could not detect any N_2 evolution in our case. Another possible explanation is that extra hydrogen can come from oxidation of small contaminations from hydrocarbons. Indeed the catalyst is able to reform hydrocarbons such as ethanol and in the very first test after the bonding of a new reactor, CO_2 (m/z = 44) and CH_4 (m/z = 15) are evolved under illumination. However these signals decrease very fast. During the measurements reported, only very small traces of CO_2, CO-N_2 (m/z =28) and CH_4 are observed which cannot justify the deviation from the stoichiometric value.

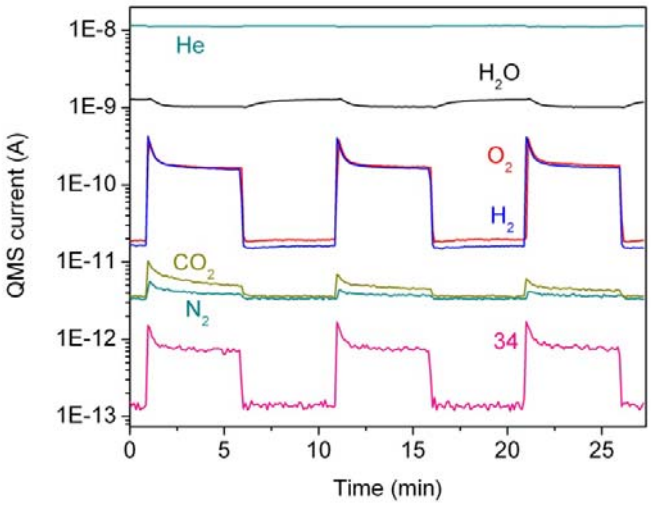

Fig. 3.15 Photocatalytic water splitting experiment. QMS current for H_2 (m/z = 2), O_2 (32), He (4), H_2O (18), CO_2 (44), N_2/CO (28) and the signal from m/z = 34 as a function of time. Three cycles of illumination with the UV LED.

The formation of H_2O_2 as an intermediate specie during the water oxidation reaction has also been considered in the efforts to find the origin of the higher hydrogen to oxygen ratio. A small amount of mass m/z = 34 was found (Fig. 3.15). However, the amount detected (in any case too small for our purpose, being two orders of magnitude less than the oxygen signal at m/z = 32) could be perfectly well explained by the by the natural abundance of ^{18}O. Assuming the ionization probability of $^{16}O_2$ and $^{18}O^{16}O$ to be the same, the ratio of $\Delta(m/z=32)/\Delta(m/z=34) = 248$ is in agreement with an abundance of 0.2% for the ^{18}O and 99.8% for the ^{16}O.

The catalyst was also exposed to illumination for many hours and no evidence of photodegradation could be found.

The quantum efficiency, defined as the ratio between the number of electrons that contribute to the reactions and the number of photons absorbed, has been calculated with the $Rh_{2-y}Cr_yO_3$/GaN:ZnO used the in these experiments. In gas phase this efficiency depends of course on the relative humidity. In this case it was chosen to calculate the efficiency at p_{H2O}= 21 mbar and T = 25 ˚C (298 K) and with the UV LED as light source (λ = 367 nm). In order to obtain the number of electrons, the number of evolved hydrogen molecules was multiplied with 2, to take into account that two electrons are necessary to make a H_2 molecule. The number of incident photons that are absorbed is estimated to be ~29% from transmission and diffuse reflectance measurements on the same catalyst deposited on a Pyrex lid before bonding. Finally, a quantum efficiency of 0.16% has been estimated. The value of 5.5 ± 0.2% has been obtained by colleagues in a liquid phase experiment using the same catalyst under irradiation with photons in the same range of wavelength (in their case 350 ± 10 nm). The values of the two experiments are in agreement with previous observations that the activity in liquid phase is higher than in gas phase. Analyzing the experiments, one can find a couple of differences apart from obviously the phase of water. In the two experiments, the catalyst is not loaded in the reactors in the same way. In the liquid case, it is dispersed in the water solution while in the gas phase experiment, it is packed in a layer of nanoparticles in contact with each other and covered with one or more monolayer of water according to the relative humidity. A second difference is that in liquid phase, it is possible to tune the pH in order to optimize and improve the activity, since this depends on pH [49], while in gas phase the pH is not defined.
As mentioned already, the microscopic reason can still be related to the different proton conductivity in the two cases.

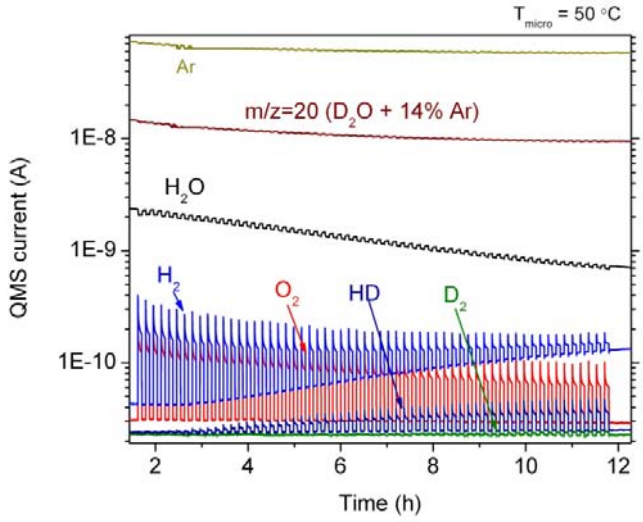

Fig. 3.16 Overnight mild temperature baking at 50˚C while flowing dry Ar and Ar saturated with D_2O. The light from the UV LED has been chopped during the experiment. QMS current for H_2 (m/z = 2), HD (3), D_2 (4), O_2 (32), H_2O (18), D_2O (20) and Ar (40) as a function of time.

3.4 Isotope effect

Receiving the suggestion (during paper submission) that the contribution of the surface proton conductivity can be elucidated by isotope experiments involving D_2O water, several tests were carried out. The bubbler was baked and filled with D_2O water (D_2O from two different suppliers was tried: Aldrich Chemical Co, D2O, 99.8 Atom % D and Cambridge Isotope Laboratory, D_2O, d_2 99.8%).

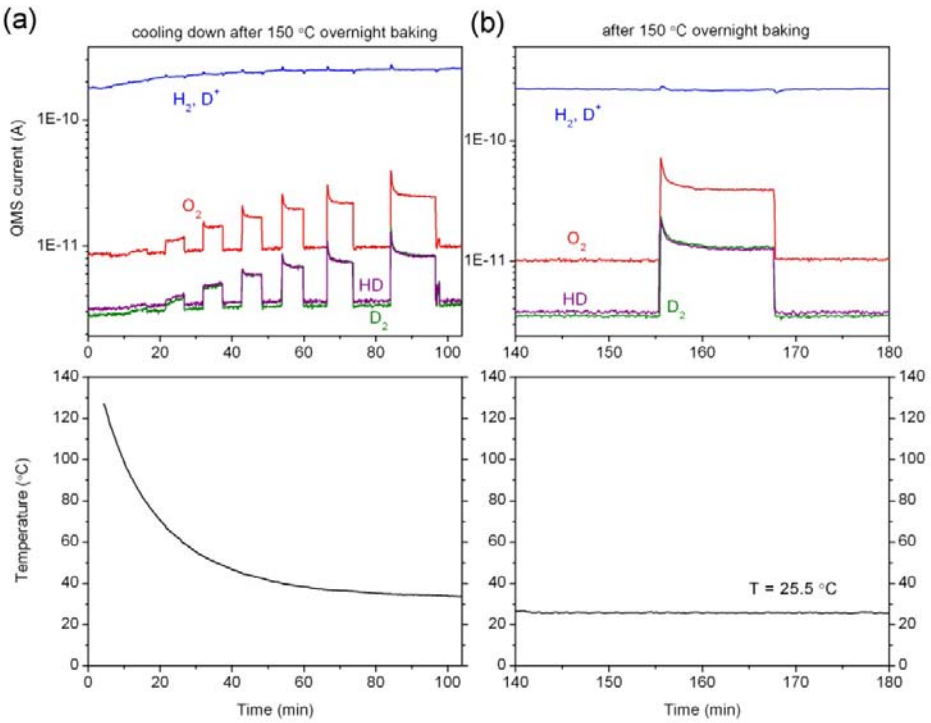

Fig. 3.17 QMS currents for H_2 (m/z = 2), HD (3), D_2 (4) and O_2 (32) after an overnight baking at 150 ˚C. The currents are plotted during the natural cool down process (top panel a) and after, when the temperature is stabilized at 25.5 ˚C (top panel b). The corresponding temperature of the μ-reactor is also plotted in the bottom panels. The light from the UV LED has been chopped during the experiments.

For this experiment, it is not possible to use Helium as carrier gas because the signal from the photocatalytic production of D_2 will overlap with the one of the Helium background since both have m/z = 4. For this reason, as a first attempt Argon was used as carrier gas. In this case, it is possible to monitor D_2 evolution, but it is not possible to see clearly D_2O, since m/z = 20 will also have contributions from double ionized Argon (also 20, since m/z = 40 with z=2). The probability of double ionization of Argon is 14%, so 14% of the m/z = 40 is the contribution of Argon to the signal at mass m/z = 20. In order to remove H_2O from the system, the lines were flushed with D_2O and baked overnight at 50 ˚C. During the baking, a sequence of illumination cycles were

performed using the UV LED and the activity detected (Fig. 3.16). In Fig. 3.16 one can notice that the evolution of D_2 and HD does not occur before the ratio of D_2O and the remaining H_2O is very high. However, the real signal of water H_2O at m/z = 18 is overlapped with cracking of D_2O to DO, with a probability of 20%. This observation reflects how difficult it is to remove H_2O and suggests an inhibition of D_2 evolution by the presence of H_2O that can be regarded as an indication of an isotope effect in favor of H^+ compared to D^+. The fact that the background of H_2 (m/z =2) increases is probably due to the cracking of D_2O to D^+ which also has mass m/z = 2.

Since, at the end of the baking, there was still a presence of protons (as can be seen for example in the signal related to HD, m/z = 3) it was decided to bake the setup again overnight at higher temperature, 150 ˚C. Furthermore, in order to be able to observe D_2O without complications, N_2 was used as carrier gas. With this carrier gas, the detection of N_2 evolution due to photodegradation is no longer possible. Anyway this was not the purpose of the experiment, and there are no reasons why this should happen in this experiment and not in the one with pure water. During the cooling down from 150 ˚C, a set of illumination cycles confirmed that also the activity for D_2 evolution from D_2O splitting decreased at higher temperature, confirming that the relative humidity discussion for H_2 evolution from H_2O splitting is very likely to be valid also in this case (Fig. 3.17a). After the baking, the signal related to H_2 had completely disappeared, or in any case could not be detected on top of the D^+ background. Unfortunately, there was still evolution of m/z =3, indicating evolution of HD (Fig. 3.17b). The presence of OH groups strongly adsorbed on the tubing surface, the reactor or the catalyst might be a possible explanation for this behavior. The final solution for this problem may require flushing the tubing and pumping for longer time and maybe baking at even higher temperatures.

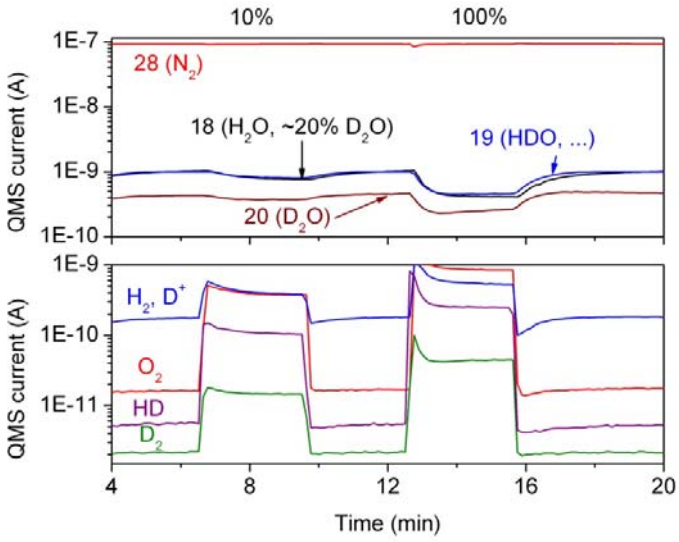

Fig. 3.18 QMS current for H_2 (m/z = 2), HD (3), D_2 (4), O_2 (32), H_2O (18), D_2O (20), HDO (19) and N_2 (28) as a function of time for a 50/50 mixture of H_2O and D_2O using N_2 as a carrier gas. The $Rh_{2-y}Cr_yO_3$/GaNZnO has been illuminated twice with the UV LED at 10% and 100% of the full power (~460 mW cm^{-2}). The currents have been plotted in two panels for convenience.

Since it was impossible to completely eliminate H^+ from the system, it was decided to perform an experiment in which the bubbler was filled with a 50/50 mixture of H_2O and D_2O. The purpose of this experiment was to see which one of the hydrogen evolution was dominant, if the H_2, the D_2 or the HD or difference in the consumption of D_2O respect to H_2O. This experiment was further motivated by the fact that the previous experiments suggested a preference for reduction of H^+. Also for this experiment, the setup was previously baked at 150 ˚C. The bubbler was at the temperature of 29 ˚C. At this temperature, the partial pressure of H_2O and D_2O are 40 and 35 mbar respectively, so the two values are very similar. The μ-reactor was at the temperature of 30 ˚C and the wet N_2 flow was slightly diluted with dry N_2, obtaining a final relative humidity of 86% for both the vapor components of the mixture (at 30 ˚C the equivalent vapor pressures are 42.5 mbar for H_2O and 37 mbar for D_2O, so you obtain the same relative humidity). One should notice that in the case of a mixture of D_2O and H_2O, also HDO is obtained due to the scrambling of the protons. The raw data are shown in Fig. 3.18 for high and low intensity irradiation.

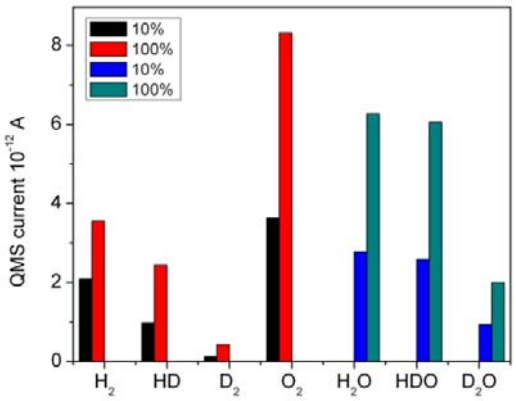

Fig. 3.19 Comparison between the rates of evolved gas [H_2 (m/z = 2), HD (3), D_2 (4), O_2 (32)] and consumed [H_2O (18), D_2O (20), HDO (19)] from the experiment shown in Fig. 3.17. Both the data with the UV LED at 10% and 100% of the full power (~460 mW cm^{-2}) are shown.

In Fig. 3.19, the global comparison of the signal is shown. For H_2, HD, D_2 and O_2 the values correspond to a positive increment during illumination, while for HDO, H_2O and D_2O the modulus of the signal is shown, because the change in their flow is negative, since they are consumed during reaction. From the comparison of HDO, H_2O and D_2O it is seen that D_2O seems to be decomposed less efficiently. If we assume the same ionization probability for H_2, HD and D_2, which is a reasonable assumption due to the similarity of these molecules, we obtain the three evolution rates. If we add these three rates and compare the sum with the oxygen evolution rate we see that a nearly stoichiometric ratio is obtained (Fig. 3.20). Comparing the single evolution rates of H_2, HD and D_2, there is a net preference for the evolution of H_2 followed by HD and finally D_2. This strong isotopic effect in favor of H_2O splitting respect to D_2O is consistent with results seen for electrolysis, suggesting that further insight might be obtained here [55, 56]. Unfortunately, it has not been possible to extract the activation energy for the D_2O splitting since quantitative experiments have been seriously hampered by the fact that

OH groups in the tubing system and in the reactor make clean D_2O experiments very difficult. However, the isotope effect that is observed here might not be related to proton mobility, since the isotope effect in that case is expected to be small, only a factor of 1.4, according to the work by Agmon and references therein [50].

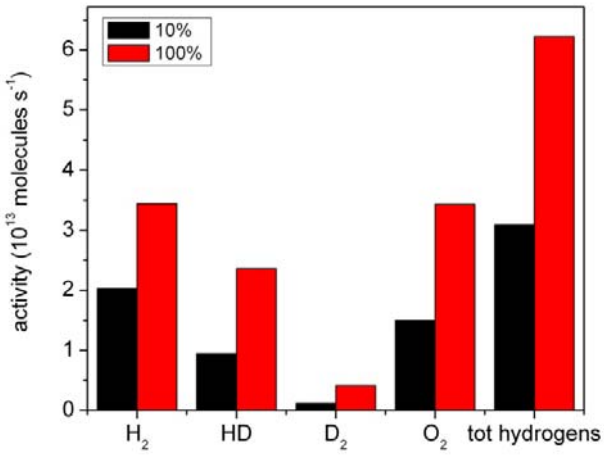

Fig. 3.20 Comparison of the activity of evolved gas [H_2 (m/z = 2), HD (3), D_2 (4), O_2 (32)] shown in the experiment in Fig. 3.17. Both the data with the UV LED at 10% and 100% of the full power (~460 mW cm^{-2}) are shown. The last two columns labeled "tot hydrogens" correspond to the sum of the first three pairs of columns (H_2, D_2 and HD) for 10% and 100% of the full UV LED intensity respectively.

3.5 Summary and conclusion – Chapter 3

This chapter has treated the gas phase photocatalytic overall water splitting reaction. The first experiments described were done using $SrTiO_3$, P25 and anatase TiO_2. These photocatalysts proved to be active under UV illumination if loaded with Pt for the production of both H_2 and O_2. The method for loading Pt is described, and the photocatalytic activity is compared for the three systems. The activity trend for the Pt loaded samples is $SrTiO_3$ > P25 > anatase TiO_2.
For the rest of the chapter, the focus moved to the more interesting GaN:ZnO. This photocatalyst loaded with $Rh_{2-y}Cr_yO_3$ is one of the few photocatalysts that is able to achieve overall water splitting with visible light. The experiments showed that this system is highly active for the gas phase water splitting reaction and hydrogen and oxygen could even be detected under illumination with a solar light simulator (AM 1.5). The visible light activity of the $Rh_{2-y}Cr_yO_3$ /GaN:ZnO has been verified using an array of blue laser diodes and a Xe lamp equipped with cut-off filters.
The effects of the parameters that are relevant for the gas phase reaction have been studied using this material. For example, the dependence of the activity as a function of light intensity showed a linear behavior for the initial rate, while the steady state is deviating from this trend. This behavior has been studied in comparison with the water consumption rate that can be also detected using our μ-reactor. The decrease in water partial pressure during the reaction explains this effect. Therefore, the dependence of the activity on the water partial pressure has been studied directly, diluting the water vapor

flow with dry helium. As expected, a proportional linear behavior was found. In contrast, the effect of increasing the temperature of the reactor is a strong decrease in the activity. Both this effect and the dependence of the partial pressure of water are explained in terms of relative humidity. Indeed the rates for H_2 and O_2 evolution as a function of relative humidity follow a linear proportionality. A simple expression for the rates of H_2 and O_2 evolution that summarize all the results has been obtained. The detailed mechanism that is associated with the dependence on the relative humidity has been explained considering the adsorption of water on the surface of the catalyst. In relation with this, we have suggested that surface proton conductivity is strongly related with the increase in activity when the relative humidity is increased. Isotope experiments using D_2O water were not enough to further prove this hypothesis even though they show an isotope effect in favor of the splitting of H_2O compared to D_2O. Nonetheless, this idea is supported by several works in the literature and, at the current status of the knowledge of the system, seems to be a valid explanation.

Chapter 4

Water splitting back reaction

4.1 Comparison of the photocatalytic activity of GaN:ZnO loaded with different cocatalysts

In the previous chapter I reported on the results of a study of the photocatalytic water splitting reaction using a $Rh_{2-y}Cr_yO_3$/GaN:ZnO catalyst. The modification of GaN:ZnO with $Rh_{2-y}Cr_yO_3$ shows a superior activity than when modified with more standard hydrogen evolution reaction (HER) catalysts such as Pt and Rh [46]. A very high activity comparable with that measured for the $Rh_{2-y}Cr_yO_3$ cocatalyst, is also obtained with a Cr_2O_3/Rh core/shell cocatalyst [45]. In this case, unlike the mixed oxide where the Cr and Rh precursors are mixed in the same solution and deposited at the same time by impregnation, the Rh is deposited first and the Cr is deposited later by photodeposition. During the photodeposition process the photogenerated electrons in the GaN:ZnO are trapped in the Rh due to its high workfunction. On the Rh surface the electrons can reduce the Cr^{6+} ions forming a shell of Cr_2O_3. In this way the deposited Cr species are only on the Rh nanoparticles and so only on the hydrogen evolution site.
The promoting effect of this cocatalyst is not just limited to GaN:ZnO. For example, Wang et Al. published recently a work on overall water splitting using GaN nanowires where they couldn't detect any activity when only Rh was loaded as a cocatalyst, while hydrogen and oxygen evolution could be observed with the Cr_2O_3/Rh core/shell cocatalyst [57].
The origin of the higher activity of the chromia shell and the chromium mixed cocatalysts is very interesting, but not simple to explain. For this reason, in this chapter we will discuss the experiments that have been performed in order to clarify this effect using unmodified GaN:ZnO and GaN:ZnO loaded with either Rh, Pt, Cr_2O_3/Rh, Cr_2O_3/Pt, or Rh–Cr mixed oxide. In this paragraph, the comparison of the activity for photocatalytic water splitting obtained with the same catalysts will be discussed. One of the motivations for these experiments was to confirm for the gas phase the same trend found in liquid experiments, since apart $Rh_{2-y}Cr_yO_3$/GaN:ZnO [47], none of the other systems were previously studied in gas phase water splitting. The second purpose of these experiments was to compare these results with the ones regarding the water splitting back reaction explained in the following paragraphs. The results presented in this chapter are based on the work published in my second manuscript that I have written in collaboration with the group of Prof. Domen [58].
For the work presented in this chapter, GaN:ZnO was prepared by Prof. Maeda and Anke Xiong. The preparation conditions were slightly different from that of the GaN:ZnO used in the experiments described in the previous chapter. This time, a mixture of β-Ga_2O_3 (1.08 g) and ZnO (0.94 g) powders was heated under a flow of NH_3 (200 ml min^{-1}) at 1098 K for 13.5 h. The as-synthesized powder was then post-calcined in a static air atmosphere at 873 K for 5 h [58].This difference is because the particle size of β-Ga_2O_3 purchasable from High Purity Chemicals Co. (Japan) has been changed, causing a change in the optimal preparation condition. The dependence of the

parameters that can be tuned during the preparation and the activity of the catalyst have been previously studied by Maeda et al. [36, 39]. Even if the starting material was different, Prof. Maeda was able to reproduce almost the same activity of the sample discussed in the previous chapter. In my experiments I have confirmed that a similar activity is obtained with the GaN:ZnO synthesized with the new conditions. The $(Ga_{1-x}Zn_x)(N_{1-x}O_x)$ solid solution (x = 0.12) obtained has a featureless morphology as can be seen in the SEM picture (Fig. 4.1) with a specific surface area of 7–8 $m^2 g^{-1}$ determined by nitrogen adsorption at 77 K. and an estimated band gap of 2.7 eV.

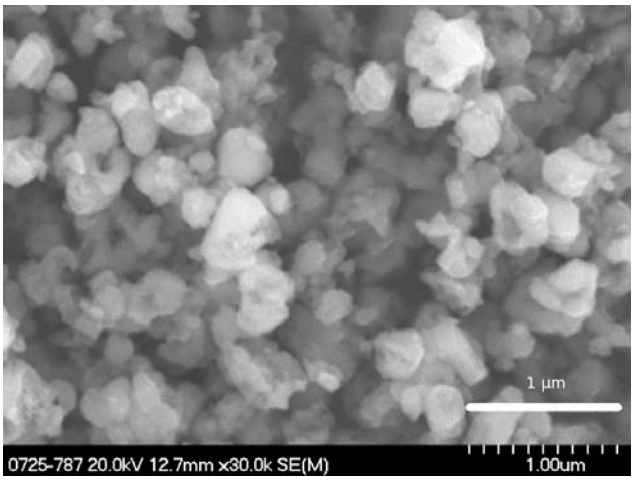

Fig. 4.1 SEM image of GaN:ZnO particles used in the experiments described in chapter 4. Figure adapted from [58].

The Rh and Pt cocatalyst were loaded by photodeposition from Na_3RhCl_6 and H_2PtCl_6 solution respectively (1 wt% of metal in both cases). With the same procedure the core of the core/shell cocatalysts has been photodeposited. After that, the Cr_2O_3 shell has been photodeposited from K_2CrO_4 solution. We estimate that ~0.3 wt% of Cr has been deposited, according to previous study and considering the self limiting nature of Cr_2O_3 photodeposition [59]. The $Rh_{2-y}Cr_yO_3$ cocatalyst (Rh 1wt%, Cr 1.5 wt%) was loaded by impregnation, using the same procedure described previously in chapter 3.

These catalysts were tested for gas phase photocatalytic water splitting using the UV LED (~367 nm) as a light source. This time, the reactors were prepared loading 60 µg of catalyst. In order to avoid too high turn-over numbers with the most active catalysts and therefore being strongly limited by diffusion of reactants, the LED were used at 20% of its power (I ~ 92 mW/cm^2). The illumination by a UV light source instead of a visible one has been performed in order to have a higher signal-to-noise ratio. Indeed, all the samples were also tested with a 1 kW Xe lamp and a longpass cut-off filter at 420 nm and even if all the samples loaded with cocatalysts were found to be active, the activity is low compared to the activities measured with the UV LED. Especially for Pt and Rh loaded samples, the signal to noise ratio is quite poor when the Xe lamp is used. The experiments were carried out at a high level of relative humidity, ~86% (constant water partial pressure ~ 27.3 mbar, and the temperature of the reactor ~ 25 ˚C, 298 K). This choice is justified by our previous finding of the importance of relative humidity in the mechanism of gas phase water splitting.

The comparison among all the catalysts tested is shown in Fig. 4.2. For both the initial rate and the stable value obtained after 5 min of illumination. No activity could be detected for GaN:ZnO without a cocatalyst, therefore it is not shown in the figure. Nonetheless that measurement is important because it shows that without a cocatalyst is not possible to have high rates of hydrogen and oxygen evolution.

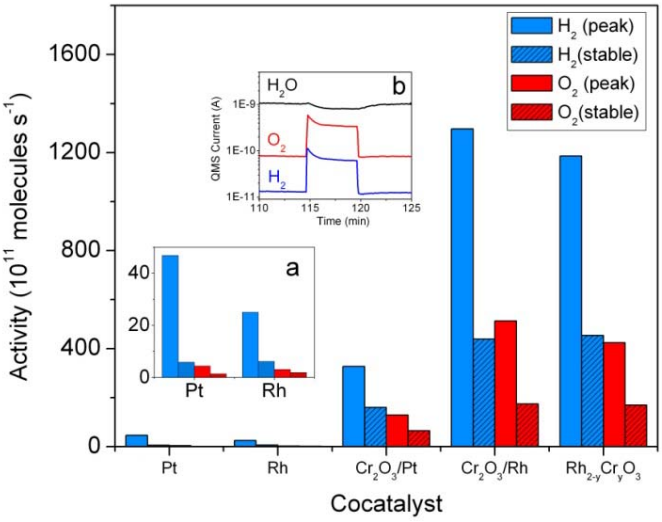

Fig. 4.2 H_2 and O_2 evolution rates for overall photocatalytic water splitting with GaN:ZnO loaded with different cocatalysts. Relative humidity 85%. UV LED at $\lambda \sim 367$ nm (I ~92 mW/cm^2). The results for Pt and Rh are also shown in an enlargement (a). The typical shape of the signals for H_2 and O_2 evolution is shown in insert (b). Both the values for the initial peak (full color) and the stable values (hatched) are shown for each gas. Figure adapted from [58].

All the other samples could evolve hydrogen and oxygen. The samples loaded with noble metals have the lowest activity. Among the Cr containing cocatalysts, the Cr_2O_3/Rh and the $Rh_{2-y}Cr_yO_3$ show similar activity, and both activities are higher with respect to the Cr_2O_3/Pt. This trend is in agreement with what has been reported in literature for the liquid phase reaction [46, 60]. In particular it is interesting to notice that the Cr_2O_3 shell improves the activity of both the noble metals.
These results are well reproducible, the uncertainty being ~15%-20% within different experiments. Possible sources of errors can be small fluctuations in the amount of catalysts loaded in the reactors, probably due to slightly different concentrations of the solution used in the drop casting, or errors in the estimation of the relative humidity.
The ratio of the H_2 to O_2 is slightly higher than the stoichiometric ratio for $Rh_{2-y}Cr_yO_3$, Cr_2O_3/Rh and Cr_2O_3/Pt, ~2.5 for both the initial and stable rate. For the noble metals, the ratio between hydrogen and oxygen evolution rates is particularly not stoichiometric for the initial peak and it decreases during illumination. This behavior seems to be consistent with what we have found and discussed previously in chapter 3 for $Rh_{2-y}Cr_yO_3$/GaN:ZnO, but unfortunately there was no satisfactory explanation for this discrepancy.
The trend in Fig. 4.2 and in particular the reason why the GaN:ZnO samples loaded with Rh and Pt have a lower photocatalytic activity than the ones loaded with $Rh_{2-y}Cr_yO_3$, Cr_2O_3/Rh and Cr_2O_3/Pt cannot be explained just considering the pure catalytic

activities of the different cocatalysts involved. For example, Pt is a very good catalyst for HER, as it has been shown in the work of Trasatti based on experiments of electrochemical hydrogen evolution [61] and in the theoretical study using DFT calculations of Nørskov et al. [62]. Rh, even if lower than Pt, has also a very high activity for hydrogen evolution. Both of these noble metals occupy top positions in the volcano plot reported in the mentioned works. Unlike them, Cr_2O_3 is not a good catalyst for HER. Therefore, other considerations are necessary to explain the trend. We will see that these considerations are based on the fact that H_2 and O_2 evolve in the same volume, unlike what happens in electrochemistry where the two gases evolve in different compartments.

4.2 Introduction to the water splitting back reaction

The water splitting back reaction is a serious problem in one-step photoexcitation systems, because for such systems hydrogen and oxygen are photocatalytically evolved in the same reactor.

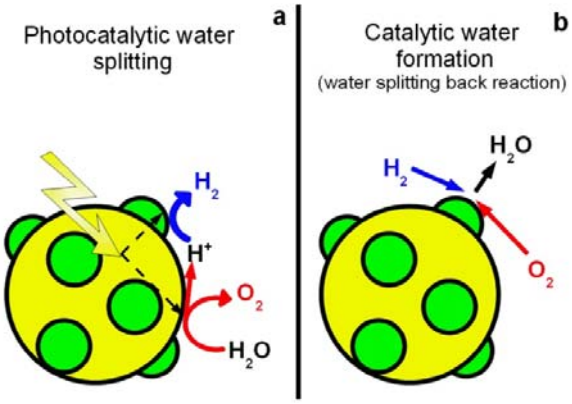

Fig. 4.3 Cartoon showing photocatalytic water splitting (a) and catalytic formation of water (b) on a photocatalyst (yellow) loaded with a cocatalyst (green). Figure adapted from [58].

As shown in the cartoon of Fig. 4.3, H_2 and O_2 can recombine on the cocatalyst, that often has active sites for hydrogen oxidation, to produce water. This is of course a process that needs to be avoided because it creates a loss of products, with their stored energy released as heat. This reaction is studied in heterogeneous catalysis in terms of the hydrogen oxidation reaction i.e. on Pt single crystals used as a model system, and Pt nanoparticles on oxide support [63, 64]. In the literature regarding photocatalysis, the problem of water splitting back reaction is well known, however only a few studies were published where the back reaction rate was measured. For this reason I will give a brief overview of the experiments that have been reported to my knowledge.
Domen et al. proposed for $Ni/SrTiO_3$ a thermal treatment to protect the Ni metal surface with NiO. This catalyst, denoted by $NiO_x/SrTiO_3$, showed improved activity that was attributed to a decreased back reaction rate [25, 65]. The improvement of photocatalytic activity was also attributed to a decreased back reaction rate for the iodine coated Pt/TiO_2 system studied by Abe et al. In this system, the iodine anions from a NaI aqueous solution were adsorbed preferentially on Pt forming an iodine atom layer, I

[66]. The authors performed a back reaction experiment introducing H_2 and O_2 gas mixture (H_2:O_2 2:1) in a close gas-circulating system connected to a Pyrex glass cell containing 10 mg of catalyst without water and measuring the total pressure. They notice that the total pressure decreases from ~65 Torr to 30 Torr in 1 min for the Pt/TiO_2 while it took 2 h for the I/Pt/TiO_2. A similar experiment was performed by Sayama et al. (mostly the same authors) with Pt/TiO_2 powder that has been previously irradiated in a Na_2CO_3 solution [67]. This system also shows an improved photocatalytic activity than the same catalyst used in pure water, where no H_2 and O_2 evolution could be observed. The back reaction experiments show that the total pressure decreases much slower for the sample previously irradiated in the carbonate salt aqueous solution. Therefore, it is concluded that the suppression of back reaction is contributing to the enhanced activity of that system. Sasaki et al. also studied the water splitting back reaction for their z-scheme system Ru/$SrTiO_3$:Rh –$BiVO_4$ [68]. Their back reaction experiment is slightly different than the one mentioned before. In their case the catalyst is in water suspension when the H_2 and O_2 mixture is introduce instead of being dry, and they monitor both the single H_2 and O_2 pressure instead of the total pressure. They also found a fast decrease of both the partial pressures when Pt is loaded instead of Ru and correlate this with the higher rate found for Ru loaded catalyst.

4.3 Measurements with μ-reactors

In the experiments mentioned one can clearly see the importance of suppressing the back reaction in order to improve the photocatalytic activity. In order to find the origin of the strong difference in activity that was found in the experiment described in the paragraph 4.1, water splitting back reaction experiments were designed and performed with the same catalysts used in the photocatalytic water splitting experiments. These experiments were inspired by the suggestion by Maeda et al. [59] that the Cr_2O_3 shell could suppress the back reaction and by the first experimental evidence using model electrodes by Yoshida et al [69].
One advantage of using the μ-reactor technology with such a small reactor chamber is that we can run a highly exothermic reaction like water formation in a very small volume, strongly limiting the amount of energy released and so the safety issue involved (see the calculation in chapter 2).
Water formation from the catalytic reaction of H_2 and O_2 was studied directly by measuring the amount of water evolved as detected by a QMS. This approach is different with respect to the one used in the previously reported back reaction experiments where the product of the reaction, that is water, is not measured. All the experiments were performed at room temperature (25 ˚C, 298 K), diluting the H_2 (2 ml/min)/O_2 (1 ml/ min) flow mixture with 15 ml/min of He and at 1 bar of total pressure. These parameters were chosen because the purpose of the experiments is to run the back reaction under similar condition to the ones that the catalysts are subjected to during a photocatalytic water splitting experiment (presence of stoichiometric H_2/O_2 mixture, room temperature and 1 bar). Instead of starting with a stoichiometric mixture as in the previously reported experiments, only one of the two reactant gases (H_2 or O_2) is present in the flow at the beginning of the experiments. In Fig. 4.4 a typical back reaction experiment starting with O_2 is presented. The experiment starting with H_2 is similar.

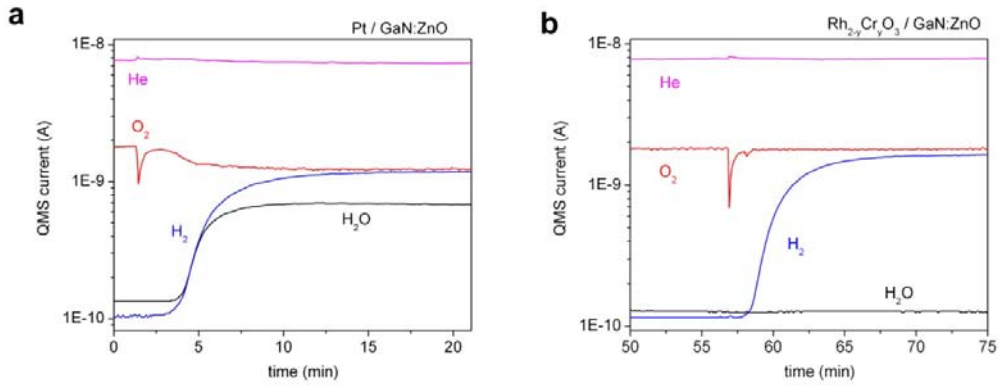

Fig. 4.4 Examples of water splitting back reaction experiments with Pt/GaN:ZnO (a) and $Rh_{2-y}Cr_yO_3$/GaN:ZnO (b). QMS currents for H_2 (m/z = 2), O_2 (m/z = 32), H_2O (m/z = 18), and He (m/z = 4) as a function of time. Figure adapted from [58].

At the beginning of the experiment only O_2 and He are flowing in the reactor. The O_2 signal drops forming a short local minimum immediately after the flow of H_2 is turned on. Usually, the H_2 is introduced 90 min after the chip is mounted in the manifold block, because at this point the background of the water signal has reached a reasonably stable value. At the same time of the O_2 minimum, a peak in the He signal occurs. These features are not related to any catalytic activity but are only due to a change in the flow of channel 1. The flow of this channel increases suddenly from 15 ml/min of He to 17 ml/min due to the 2 ml/min flow of H_2. In Fig. 4.4a, where the raw current for a reactor loaded with Pt/GaN:ZnO is shown, one can see that water starts evolving after the introduction of H_2. At the same time, the oxygen is consumed, confirming the occurrence of the back reaction:

$$2H_2 + O_2 \rightarrow 2H_2O \tag{4.1}$$

The experiment was performed in the dark, so the formation of water is purely catalytic and occurs without the need of photogenerated carriers. The Langmuir-Hinselwood is the dominant mechanism of this spontaneous reaction ($\Delta G < 0$) that occurs via the dissociative adsorption of hydrogen and oxygen [63]. The behavior of the $Rh_{2-y}Cr_yO_3$/GaN:ZnO is completely different than the one of Pt/GaN:ZnO as can be seen in Fig. 4.4b. In this case no water formation or consumption of oxygen could be detected. This measurement clearly shows that water splitting back reaction is suppressed when $Rh_{2-y}Cr_yO_3$ is used as a cocatalyst instead of Pt. This experiment also rules out the possibility that the water evolution observed in the first experiment is due to catalysis occurring on the hot filament of the QMS. If this happens it is negligible and occurs at a rate below my detection limit.
This experiment was performed for all the other samples tested in paragraph 4.1, including the GaN:ZnO without cocatalyst. In this case no formation of water was measured, confirming that the back reaction is not occurring at a significant rate on the GaN:ZnO surface but only on the cocatalyst. This also implies that the conclusion drawn from this study can probably be extended for the same cocatalysts loaded on

different photocatalysts than GaN:ZnO. The comparison of the activity for back reaction for all the samples is shown in Fig. 4.5.

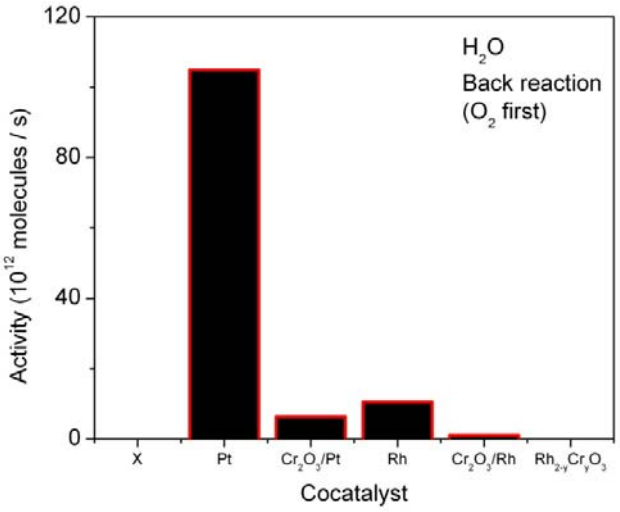

Fig. 4.5 Comparison of the water formation rates in the water splitting back reaction experiments starting with a flow of O_2 and He for the GaN:ZnO loaded with different cocatalysts. The "x" stands for the GaN:ZnO powder without cocatalyst.

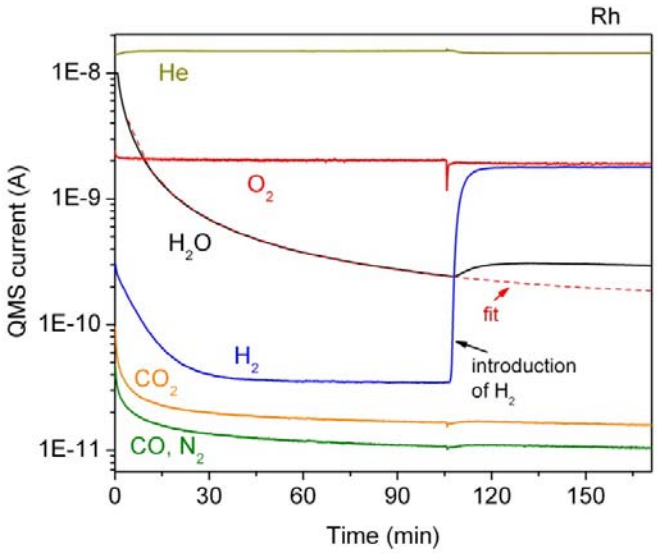

Fig.4.6 Water splitting back reaction experiment with Rh/GaN:ZnO showing the fitting (dotted line) used to estimate the water background. The QMS currents for H_2 (m/z = 2), O_2 (32), H_2O (18), He (4), CO_2 (44) and CO/N_2 (28) are shown as a function of time. Figure adapted from [58].

The water formation rate is measured after 30 min of the introduction of the second reactant gas (that in the case of Fig.4.5 is H_2). The water background is slightly decreasing during experiment, so a fitting line is used as background and subtracted from the water evolution signal in order to obtain a better estimate of the rate.

This fitting is calculated in the time of the experiment before the introduction of the second reactant and extended to the following times. An example of the fit is shown in Fig. 4.6 for the case of Rh/GaN:ZnO. From the comparison of the rates we can see that the back reaction runs much faster on Pt and that both the noble metals has a higher catalytic activity for water formation than their respective core/shell cocatalysts.

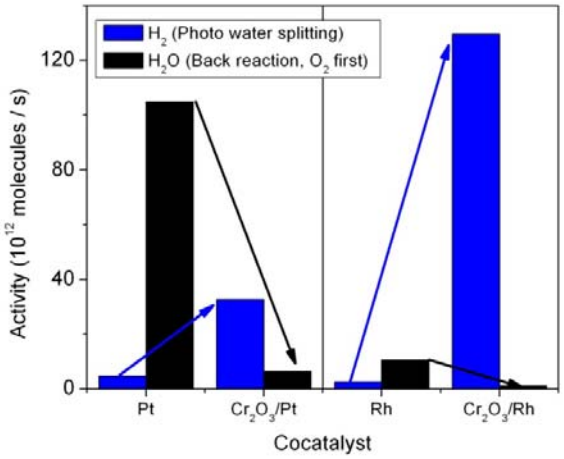

Fig. 4.7 Comparison between the GaN:ZnO loaded with the two noble metals and their core/shell modification. In the figures, the initial H_2 evolution rate for overall photocatalytic water splitting (blue) and the H_2O formation rate for the dark back reaction experiments starting with O_2 (black) are shown. Figure adapted from [58].

In order to formulate an explanation for the photocatalytic trend shown in Fig. 4.2, we can focus on the comparison of the noble metals with their respective core/shell modification for both the photocatalytic water splitting rate and the dark back reaction rate (Fig. 4.7). For both noble metals, the effect of the Cr_2O_3 shell is to enhance the net photocatalytic water splitting activity and suppress the back reaction. These experimental findings confirm the results by Yoshida et al. obtained with the model electrodes [69]. The Cr_2O_3 shell blocks the O_2 that cannot reach the noble metals surface. In this way, the oxygen reduction reaction (ORR):

$$4H^+ + 4e^- + O_2 \rightarrow 2H_2O \qquad (4.2)$$

as well as the catalytic reaction between H_2 and O_2 (reaction drawn in Fig. 4.3b) is strongly suppressed. At the same time the shell is penetrable to protons. Therefore they can reach the metals surface, react with the photoexcited electrons and escape passing through the shell as hydrogen molecules. The H_2 molecules could be able to pass the shell due to its smaller radius compare to the O_2 molecules. So the Cr_2O_3 acts as an oxygen-blocking proton/hydrogen membrane (Fig. 4.8).
The high activity for back reaction shown by Rh and Pt is well understood when compared with what is known in the literature. Indeed, Pt and Rh show a high activity for ORR as reported in fuel cell study [70] and in the volcano plot calculated using DFT by Nørskov et al. [71]. Comparing the volcano plot for ORR with the one for HER one can see that in both cases the two noble metals, and especially Pt, occupy positions very

close to the peak. Therefore, they are good catalysts for both the reactions. So the trend shown in Fig. 4.2 is a trade-off between these two phenomena. In order to have a high photocatalytic net activity the cocatalyst should be very good for HER but very poor for ORR. However this condition is very difficult to be fulfilled by a single material. It is probably a better approach to try to protect the HER catalyst with a proton permeable membrane, like the Cr_2O_3. In this way even if the cocatalyst is good for ORR, this reaction will not run because it is separated from the O_2 produced at the OER active sites.

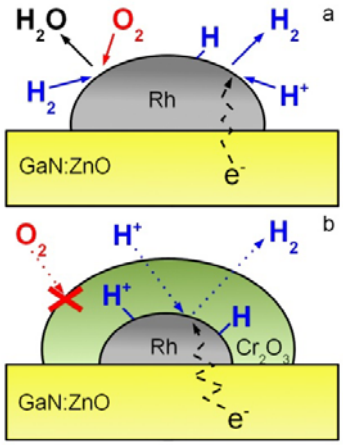

Fig. 4.8 Oxygen blocking by the proton- and hydrogen-permeable Cr_2O_3 shell. In the case of Rh/GaN:ZnO both the photocatalytic H_2 evolution and the catalytic H_2 oxidation occur on the Rh surface (a). In the case of Cr_2O_3/Rh cocatalyst, H_2 evolution still occurs at the Rh surface due to the permeability of the Cr_2O_3 shell, but the O_2 is prevented to reach the Rh surface (b). Figure adapted from [58].

This mechanism is valid for both Cr_2O_3/Rh/GaN:ZnO and Cr_2O_3/Pt/GaN:ZnO and explains their higher net photocatalytic water splitting rates compared to the respective noble metals. However, it is interesting to notice that there is a big difference in the net photocatalytic activity between the two core/shell systems (Fig. 4.7). When GaN:ZnO is loaded with Cr_2O_3/Rh, the net rate of photocatalytic production of H_2 and O_2 is higher. This behavior is also observed in liquid phase experiments [60]. This difference can be also explained considering the balance of photocatalytic H_2 and O_2 production and catalytic back reaction. The forward photocatalytic water splitting rate is expected to be higher with the system containing Pt from considerations based on the higher activity of Pt than Rh for HER reaction. However the water formation is not completely suppressed in the case of Cr_2O_3/Pt/GaN:ZnO, while for the Cr_2O_3/Rh/GaN:ZnO is basically negligible. As a result, we can very likely obtain the net activity measured in the photocatalytic experiments.

This explanation suggests that the system with a Pt core will be more active, maybe even more than the one with a Rh core, if Pt could be protected more efficiently from oxygen.

Notice that the hypothesis of a higher forward water splitting rate of the Cr_2O_3/Pt/GaN:ZnO is also supported by the comparison of the GaN:ZnO loaded with the bare noble metals. In this case, even if Pt/GaN:ZnO has a much higher rate for back reaction than Rh/GaN:ZnO, their net photocatalytic activity is comparable. Therefore,

the forward photocatalytic water splitting activity has to be higher in the case of Pt/GaN:ZnO than Rh/GaN:ZnO.

The proposed explanation that the increased photocatalytic activity is obtained by the suppression of the back reaction implies that the rate determining step is the charge transfer to the molecules at the surface of the catalyst and not the charge transfer at the interface between the GaN:ZnO and the cocatalyst. This second case could have also influenced the trend due to possible different Schottky barriers at the metal/semiconductor interface. However, it seems that this is not the case for our samples. The conclusion that the rate determining step is not the charge transfer at the interface between the photocatalyst and the cocatalyst is in agreement with the work published by Szklarczyk and Bockris [72]. The authors performed experiments to study electrochemical H_2 evolution with p-InP photocathodes covered with islets of different metals (Pb, Cd, Co, Au, Ni and Pt). The activity from these electrodes showed a good correlation with the activity of the electrodes made of the bulk metals. From this comparison, the authors conclude that the charge transfer at the photocatalyst–cocatalyst interface is not the rate determining step in the photoelectrochemical evolution of H_2 in the case of a semiconductor covered with metal islets. This conclusion is also supported by the comparison of the characteristic times for primary processes in photocatalysis reported in the review of Fujishima et al. about TiO_2 [73]. For TiO_2 loaded with Pt, the characteristic times for a charge to transfer from the TiO_2 to the Pt cluster is much faster than the interfacial transfer to adsorbates. Therefore, the last one is more likely to be a rate limiting step.

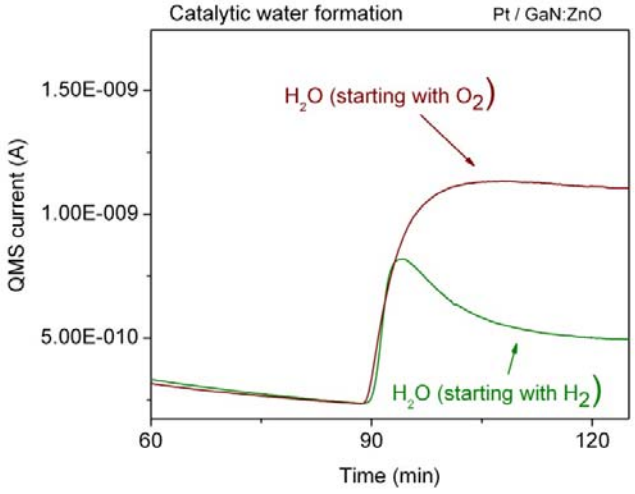

Fig. 4.9 Comparison of the QMS current increase associated to H_2O formation in catalytic water splitting back reaction (H_2 and O_2 mixed in the stoichiometric ratio) starting with dry H_2 or O_2 on Pt/GaN:ZnO. This graph combines the results of two different experiments. The x-axis in the case of the reaction performed adding H_2 to the O_2 flow has been rescaled of ~10 min in order to have the H_2O formation starting at the same time.

The mechanism discussed so far is based on a model valid for the core/shell cocatalysts. However, also with the GaN:ZnO loaded with the Rh-Cr mixed oxide no water

formation could be detected meaning that this catalyst is also able to suppress the back reaction. To explain the behavior of this cocatalyst and the high photocatalytic activity of the $Rh_{2-y}Cr_yO_3$/GaN:ZnO is more difficult because it is still not clear the role of the Rh species in the cocatalyst during the photocatalytic water splitting reaction. In other words, it is not clear if the $Rh_{2-y}Cr_yO_3$ is a completely new material (a solid solution of Rh_2O_3 and Cr_2O_3, notice that both of them has a corundum crystal structure) or if it is a composite material that can be explained by the property of Rh and Cr_2O_3. At the present stage it is known by a work of Maeda et al. based on XPS and XAFS experiments that the state of Rh species in the Rh-Cr mixed oxide is trivalent and remains unchanged after the reaction [49]. So even if the suppression of the back reaction is definitely contributing to the high photocatalytic activity, it is not sure how the hydrogen evolution can occur so efficiently on this cocatalyst.

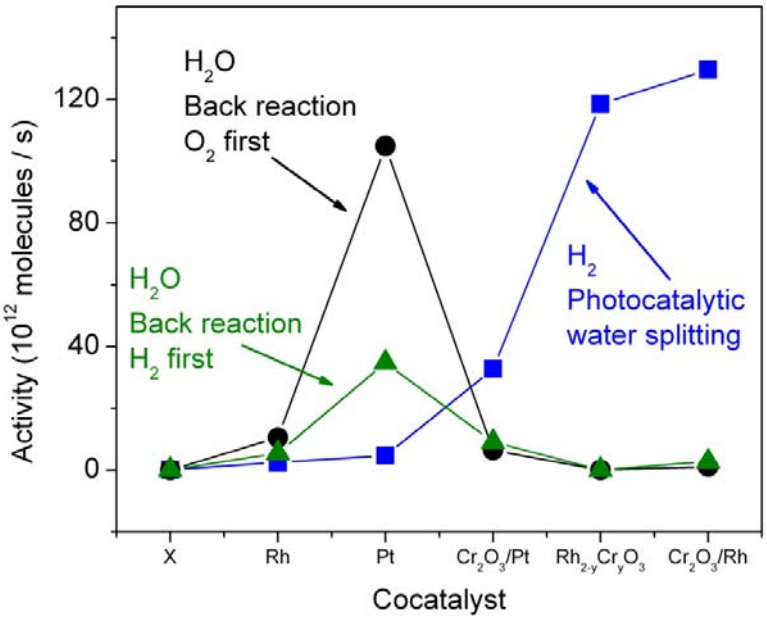

Fig. 4.10 Comparison between the rates for overall photocatalytic water splitting (only the H_2 rate is shown, blue squares) and catalytic back reaction experiments (H_2O formation in the dark) starting with H_2 (green triangles) or O_2 (black circles) diluted in He. This graph combines the results of three different experiments performed with GaN:ZnO loaded with the cocatalysts indicated in the x-axis. The "X" indicates the bare GaN:ZnO powder without cocatalyst. Figure adapted from [58].

As mentioned before, the back reaction experiment has been also repeated changing the order of introduction of the oxygen and hydrogen gas. In the two experiments there is a big difference in the starting conditions, a dry oxygen atmosphere in the first case and a dry hydrogen atmosphere in the second, while the reaction conditions are the same, H_2:O_2 mixture at stoichiometric ratio for water formation.
We have noticed a different kinetic behavior in this case. Indeed, unlike the experiments that start with O_2, the water signal for the samples that are active for the back reactions rises reaching a maximum at time ~4 min after the introduction of O_2 and then decreases to a new steady state level. For GaN:ZnO loaded with Rh and Pt, these two values are lower than the steady state rate reached when the experiment starts with O_2. A comparison of the two water signal is shown in Fig. 4.9 for the case of Pt/GaN:ZnO (All

the raw measurements are available as supplementary information of [58], the second manuscript attached at the end of the thesis).
All the results for both back reaction experiments and photocatalytic water splitting are summarized in Fig. 4.10. Only the hydrogen data have been plotted for the water splitting experiments, avoiding a too complicated figure.
The trend for the two back reaction experiments is basically the same with only a difference in the absolute value of the water formation rate.
This behavior that depends on the order of gas introduction for the back reaction experiments can be explained considering the different surface coverage of adsorbates at the cocatalyst nanoparticles. Indeed, hydrogen poisoning of the surface is known to occur at moderate low temperature, like the one of our experiment. This effect originates from the weak temperature dependence of its sticking coefficient compared to the exponential temperature dependence of desorption. As a result of the different dependence of surface coverage for H_2 and O_2, a hysteresis cycle has been reported for Pt performing an experiment where the relative hydrogen concentration in the H_2-O_2 mixture has been increased and decreased [64, 74]. The observed behavior is in agreement with the two different steady-state reaction rates that we have seen.
Another difference between the two back reaction experiments is that the positive effect of the Cr_2O_3 shell of suppressing this unwanted reaction seems slightly stronger when the starting atmosphere is O_2. A partial reduction of the shell when the catalyst is exposed to a flow of H_2 flow may be responsible for this behavior. However, this point was not investigated further, since the experiment that starts with a H_2 flow is less interesting because it less resembles the real condition of a photocatalytic experiment. Indeed in that case and in what is probably going to happen in a real device, the catalyst is exposed to air before being dispersed in water or exposed to water vapor. Therefore it is not exposed to a reducing hydrogen atmosphere.

4.4 Water splitting back reaction and illumination

The back reaction experiments described so far were performed in the dark. The measurements show that light is not necessary to run this undesired reaction. For example water is produced at a very high rate on Pt even at room temperature and without illumination. However there can be the doubt that the GaN:ZnO samples loaded with cocatalysts that do not show back reaction in dark will do so when illuminated. The need to check if the back reaction is suppressed also under illumination is interesting because this condition is naturally present in the case of a photocatalytic experiment. Therefore, the back reaction experiments were performed and the samples were illuminated with the UV LED at full power when exposed to the stoichiometric mixture of H_2 and O_2. These experiments are just a continuation of the one discussed in the previous paragraph, so the procedure of introduction of the gas mixture is exactly the same. The light was shine before and ~30 min after the second reactant gas introduction with illumination cycles of 5 min light on - 5 min light off repeated 3 times. One of the reasons of exposing the samples to light when only H_2 or O_2 were flowing in the reactor is to clean the surface before the stoichiometric experiment from eventually small amount of dirt deposited from air. The second reason was to compare the behavior in

this case with the one under stoichiometric mixture. No light induced water formation was detected with GaN:ZnO without cocatalyst or with the Rh-based cocatalysts. An example is shown in Fig. 4.11 for the case of $Rh_{2-y}Cr_yO_3$/GaN:ZnO when starting with a flow of H_2. If there is an effect, it is below my detection limit, and much slower than the back reaction rate of Rh in the dark. This observation means that the sample with $Rh_{2-y}Cr_yO_3$ and Cr_2O_3/Rh cocatalysts are able to suppress the back reaction also in the presence of light.

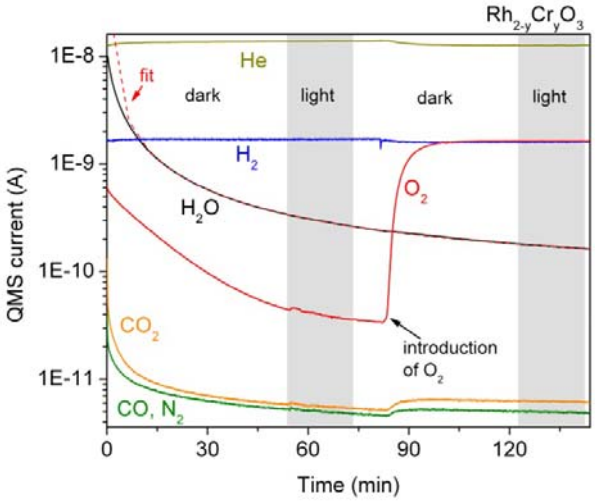

Fig. 4.11 Effect of illumination in a water splitting back reaction experiment with $Rh_{2-y}Cr_yO_3$/GaN:ZnO. The QMS currents for H_2 (m/z = 2), O_2 (32), H_2O (18), He (4), CO_2 (44) and CO/N_2 (28) are shown as a function of time. The experiment starts with a dry flow of H_2 (2 ml/min) and He (15 ml/min). At ~80 min O_2 (1 ml/min) is dosed. The grey shaded area before and after the introduction of O_2 correspond to illumination cycles with chopped light (3 light cycles of 180 s light on and 180 s light off, UV LED at $\lambda \sim$ 367 nm and I ~ 460 mW/cm^2). The H_2O background signal has been fitted in the time interval before the introduction of O_2 and the fit extended to the following times (dashed red line). Figure adapted from [58].

The case of Pt and Cr_2O_3/Pt is different. Here the water signal rises when the light is switched on, especially in the experiments starting with the H_2 flow. In particular for Pt, a new steady state is reached under illumination when the experiment starts with H_2. With this sample, the experiment was repeated two times without dismounting the chip to check if this effect was due to cleaning of surface contaminations, for example hydrocarbons (Fig. 4.12). The two experiments show exactly the same result. After the second introduction of O_2 the behavior in the dark is equal to the one of the first experiment, so the surface of Pt, responsible for the catalytic activity, is not irreversibly affected by light during the first experiment. However the behavior during illumination is clearly different than in the dark. A tentative explanation can be formulated based on a change in surface coverage of the cocatalyst induced by interactions of the adsorbates with the photoexcited carriers under illumination.

Performing this experiment, we have also found that the QMS signal at mass m/z =28 increases under illumination in the presence of the stoichiometric mixture. Also m/z=44, that corresponds to CO_2, is slightly increasing. The photoinduced behavior of m/z= 28 was attributed mainly to N_2 evolution. The reason is that this signal cannot be attributed to CO or cracking of CO_2 because its evolution as a function of time has a different

shape than mass CO_2 and a higher rate. Furthermore, this attribution is also supported by the ratio of the measured mass 14 and 28. This one is equal to 0.15 as expected from the ionization pattern of N_2 (the normalized relative intensity of m/z = 14 to 28 is expected to be 0.14).

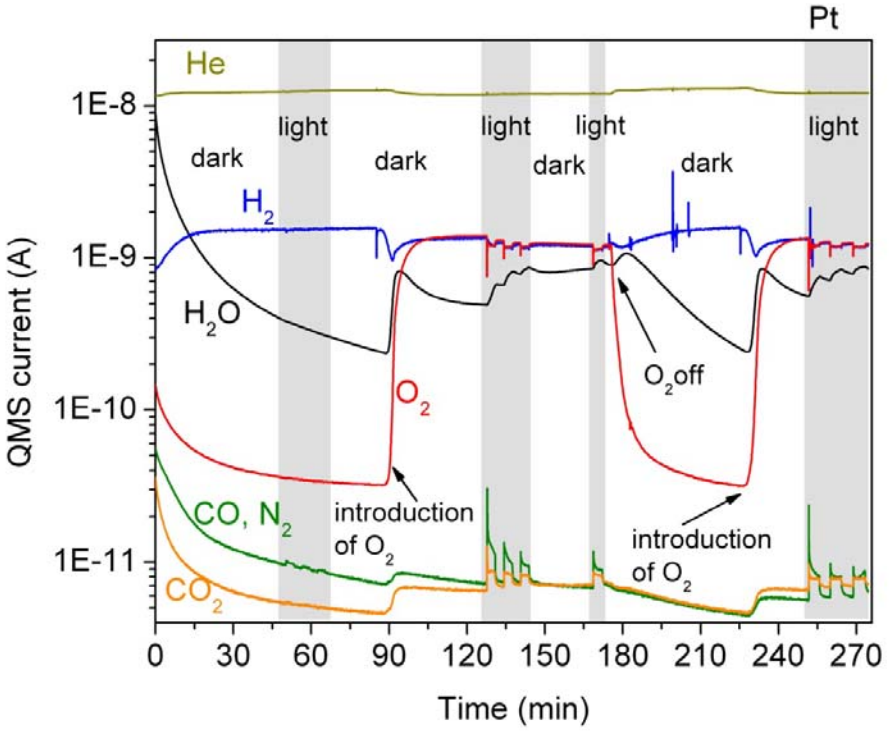

Fig. 4.12 Effect of illumination in a water splitting back reaction experiment with Pt/GaN:ZnO. The QMS currents for H_2 (m/z = 2), O_2 (32), H_2O (18), He (4), CO_2 (44) and CO/N_2 (28) are shown as a function of time. The experiment starts with a dry flow of H_2 (2 ml/min) and He (15 ml/min). At ~90 min O_2 (1 ml/min) is dosed. The O_2 flow is then switched off at ~180 min and turned on again at ~225 min. The grey shaded area correspond to illumination cycles with chopped light (3 light cycles of 180 s light on and 180 s light off at ~50 min, 3 cycles at ~125 min, 1 cycle at 168 min, 3 cycles at 250 min, UV LED at $\lambda \sim$ 367 nm and I ~ 460 mW/cm^2). Figure adapted from [58].

Therefore in the presence of H_2 and O_2 and water produced by back reaction the photocorrosion of GaN:ZnO,

$$2N^{3-} + 6h^{+} \rightarrow N_2 \qquad (4.3)$$

, seems to proceed when Pt is loaded as a cocatalyst. This is a small effect, two orders of magnitude smaller than the water signal, but still detectable. The corrosion is also observed with the stoichiometric mixture when the experiment starts with O_2 but not during the photocatalytic water splitting experiment and only with the Pt/GaN:ZnO. Both the water and a relatively high pressure of O_2 seem to be necessary to cause this photodegradation.

In order to further examine this effect, a photocatalytic water splitting experiment where O_2 is introduced in the flow of water vapor was performed. With this experiment the

photocatalytic H_2 evolution with and without the extra O_2 not produced by the photocatalytic process can be compared.

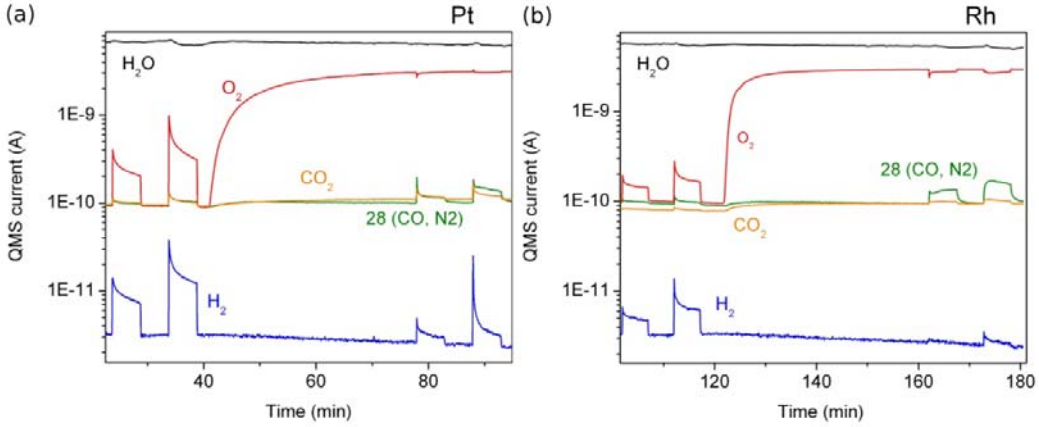

Fig. 4.13 Dosing O_2 in a photocatalytic water splitting experiment with GaN:ZnO loaded with Pt (a) and Rh (b). The catalysts have been tested with two cycles of illumination at 20% and 100% of full intensity both before and after the introduction of O_2. The QMS currents for H_2 (m/z = 2), O_2 (32), H_2O (18), CO_2 (44) and CO/N_2 (28) are shown as a function of time.

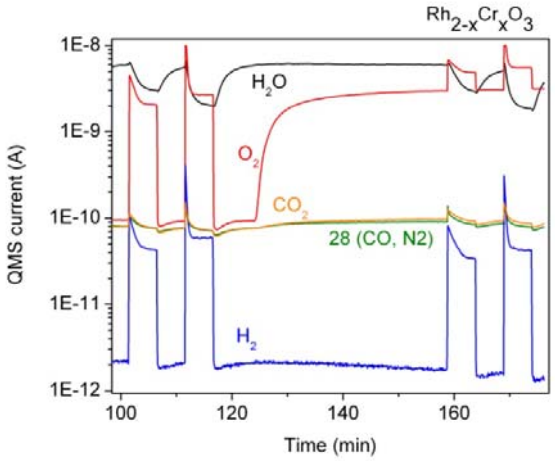

Fig. 4.14 Dosing O_2 in a photocatalytic water splitting experiment with GaN:ZnO loaded with $Rh_{2-y}Cr_yO_3$. The catalyst has been tested with two cycles of illumination at 20% and 100% of full intensity both before and after the introduction of O_2. The QMS currents for H_2 (m/z = 2), O_2 (32), H_2O (18), CO_2 (44) and CO/N_2 (28) are shown as a function of time.

The experiments were performed with relative humidity ~85%, 10 ml/min the flow of wet He and 1 ml/min the flow of dry He. Under this condition, the UV LED was switch on twice, at 20% and 100% of the total intensity. Then O_2 was introduced at 0.3 ml/min and the illumination cycle described before was repeated. This experiment was performed with all the samples described previously in this chapter. A strong decrease in the H_2 evolution rate can be seen when extra oxygen is present with the Rh and Pt sample, while the other samples keep roughly the same rate. Photocatalytic N_2 evolution was observed with Pt/GaN:ZnO (Fig. 4.13a) and Rh/GaN:ZnO (Fig. 4.13b) but not with the other samples (the example of $Rh_{2-y}Cr_yO_3$/GaN:ZnO is shown in Fig. 4.14). The N_2

evolution is difficult to see before the introduction of O_2 while N_2 is clearly evolving afterwards. This confirms the fact that both water and O_2 are necessary to observe the photodegradation. However, these experiments were never repeated, so further measurements and a stability test have to be made to completely clarify the mechanism.

4.5 Summary and conclusion – Chapter 4

The effect of the water splitting back reaction on the net rates of H_2 and O_2 evolution in photocatalytic water splitting experiments is discussed in this chapter. The first paragraph starts comparing the photocatalytic activity for gas phase water splitting of GaN:ZnO without cocatalyst and loaded with Rh, Pt, Cr_2O_3/Rh, Cr_2O_3/Pt, and Rh–Cr mixed oxide. The results are in agreement with liquid phase experiments reported in the literature and show that a higher activity is obtained by loading the GaN:ZnO with Cr_2O_3/Rh, Cr_2O_3/Pt, and Rh–Cr mixed oxide with respect to Pt and Rh. The cocatalysts are loaded in order to improve the charge separation and surface kinetics for the hydrogen evolution reaction. However the trend can't be explained only by the catalytic activity of the cocatalyst. Recent works published in the literature show that the enhanced activity can be due to the suppression of the back reaction by the core/shell cocatalysts. For this reason, the rate of water formation has been measured for the mentioned catalysts. The experiment designed to test the back reaction is performed at room temperature introducing hydrogen (or oxygen) in a flow of oxygen (or hydrogen) in the stoichiometric ratio (H_2:O_2 2:1). The rate of water formation can then be detected by the QMS. These experiments were done using the same catalysts that have been tested for the water splitting reaction so that the rate for the two reactions can be directly compared. The back reaction was tested both in the dark and under illumination and the results clearly show how the water formation is suppressed for the GaN:ZnO loaded with Cr_2O_3/Rh, Cr_2O_3/Pt, and $Rh_{2-y}Cr_yO_3$ and at the same time the activity is strongly increased with respect to Pt/GaN:ZnO and Rh/GaN:ZnO. Both the experiments starting with H_2 or O_2 show the same trend, with some differences due to different surface coverage of the cocatalysts surface.
The core/shell cocatalysts show lower back reaction rate than the respective noble metals, which can explain their higher net photocatalytic activity. These results are in agreement with the idea that the Cr_2O_3 shell acts as an oxygen blocking proton permeable membrane as suggested in the literature. Also the $Rh_{2-y}Cr_yO_3$ /GaN:ZnO system shows a higher activity associated with the suppression of the back reaction, even if in this case a detailed mechanism is not clear. The higher activity of Cr_2O_3/Rh respect to Cr_2O_3/Pt loaded GaN:ZnO, observed also in liquid phase experiments, can be explained by the incomplete suppression of the back reaction by the Cr_2O_3 shell on the Pt core, as seen in our experiments. This finding suggests that the activity of Pt/GaN:ZnO can be enhanced if a more efficient shell is deposited. The study of the back reaction under illumination did not change the picture obtained from the dark experiments. Nevertheless, it shows some effects regarding photodegradation in presence of oxygen and water that might be interesting to investigate.

Chapter 5

Expanding the capabilities of the µ-reactor platform

5.1 Introduction and motivation

The results presented so far were obtained with our silicon based µ-reactor. This design proved to be very good in measuring photocatalytic activities with different samples and reactions and also to study fundamental mechanisms of photocatalysis. However, as mentioned before, this reactor cannot be opened to analyze the catalysts after bonding and after running a reaction. The only method is to break the chip, and in this case no further measurements of catalytic activity are possible. It is of course desirable to overcome this limitation, so that in situ techniques will be available to analyze the catalyst before and after reaction and maybe even during a reaction. Part of my PhD was spent to achieve this goal. The results in this chapter have never been published and are in part preliminary.
There are mainly two strategies that can be followed to achieve the mentioned purpose. One possibility consists in changing the material or the thickness of the Pyrex lid and the silicon chip. To change the material allows changing the wavelengths that will be absorbed by the reactors, while to reduce the thickness will reduce the absorption of photons. This approach is particularly indicated for the purpose to combine optical techniques in the visible, UV, infrared or X-ray range of wavelength with the reactor. An example of this kind of reactor is the "transparent" µ-reactor that will be introduced in the next paragraph. However, techniques that use electrons as a probe or detects the out coming electrons cannot be easily integrated with this kind of modifications, due to the fact that electrons have a much smaller mean free path than photons (~0.3-3 nm for electrons with energy from 10 to 2000 eV). Therefore, the reactor chamber cannot be closed with a lid with thickness in the µm range. The second approach is more useful for this purpose. This modification consists in abandoning the idea of a permanently closed reactor. In this case, the Pyrex and the silicon are still anodic bonded together to seal the structure of µ-channels but the chamber is open on at least one side. The chamber needs to be sealed during reaction by applying a pressure between the reactor and a sample holder with an o-ring in between. In this way, the µ-reactor can be opened and closed several times. An attempt to make such a device is explained later.

5.2 Transparent µ-reactor: design and bonding

In order to characterize the catalysts loaded in a µ-reactor with optical measurements, a new kind of µ-reactor was designed. The main idea about this design is to remove the silicon chip that constitutes the bottom part of the reactor, and replace it with a Pyrex chip. In this way the device is fully transparent in transmission for a wide range of light frequencies, and measurements in reflection should be easier with the elimination of the silicon background. The first consequence of this substitution is that now anodic

bonding will not work. However, since anodic bonding is a cleaner sealing technique than the use of a polymer, it was decided to use the anodic bonding method to seal the new device. In order to be able to use anodic bonding, a very thin silicon layer (200 nm thick) was grown in a furnace on top of one of the Pyrex. The standard procedure to grow the polysilicon layer is to pyrolyze SiH_4 at temperatures ~600 °C. After growing the silicon, the underneath Pyrex and the silicon layer itself can be etched to obtain the fully transparent reactor chamber and the gas flowing channels. The polysilicon layer is etched in HNO_3:BHF:H_2O (20:1:20) and the Pyrex is etched in 40% HF, both at room temperature. The Pyrex is etched for one minute and the etch rate is about 3500 nm/min. The silicon will remain only in the places that are going to be sealed with the other Pyrex lid, and so where the device doesn't need to be transparent. A section showing the stacking structure of the device is sketched in Fig. 5.1.

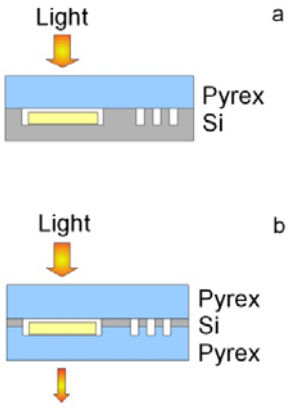

Fig. 5.1 Section of a standard silicon-based µ-reactor (a) and the new transparent µ-reactor (b) from a side view prospective.

This device is a stacking structure of 3 layers, Pyrex/silicon//Pyrex, where the double dash indicates the anodic bonding. In this notation, the standard silicon based µ-rector has the structure silicon//Pyrex. A big difference between the two devices is associated with the etching of the channel structure. Since the Pyrex is amorphous, the wet etching in this case is not directional. With this isotropic etching it is difficult to obtain channels that are deep and narrow like in the case of a silicon wafer. In particular, the compact meander structure that is used to mix the gases in the silicon based µ-reactor cannot be reproduced in the transparent µ-reactor. In order to assure appropriate mixing in chip, the meander structure has been redesigned in a long channel that goes around the long and narrow side of the reactor for two times (Fig. 5.2). A gas *A* that enters the chip in the first input hole flows into two channels that are connected with the short inlet channel of the second input hole. In this way gas *B* that is flowing in this channel is in contact with gas *A* from both sides. With this design the diffusion length is decreased because now gas *B* can diffuse on both sides into the flow of gas *A* and so mix in a shorter time. Finally, the chamber has been moved to the right respect to the long axis of the reactor to make space for the long mixing channel.

A minor difference with respect to the silicon µ-reactor is that now the bonded reactor is slightly thicker. Before, the total thickness was 500 µm (Pyrex)+ 350 µm (silicon), while now, since the same Pyrex wafer is used for both the sandwich components, the total thickness is 500 µm + 500 µm (plus 200 nm for the polysilicon). This requires the

use of a new bar in order to have space enough for the 1000 μm thick reactor when the reactor is mounted on the block.

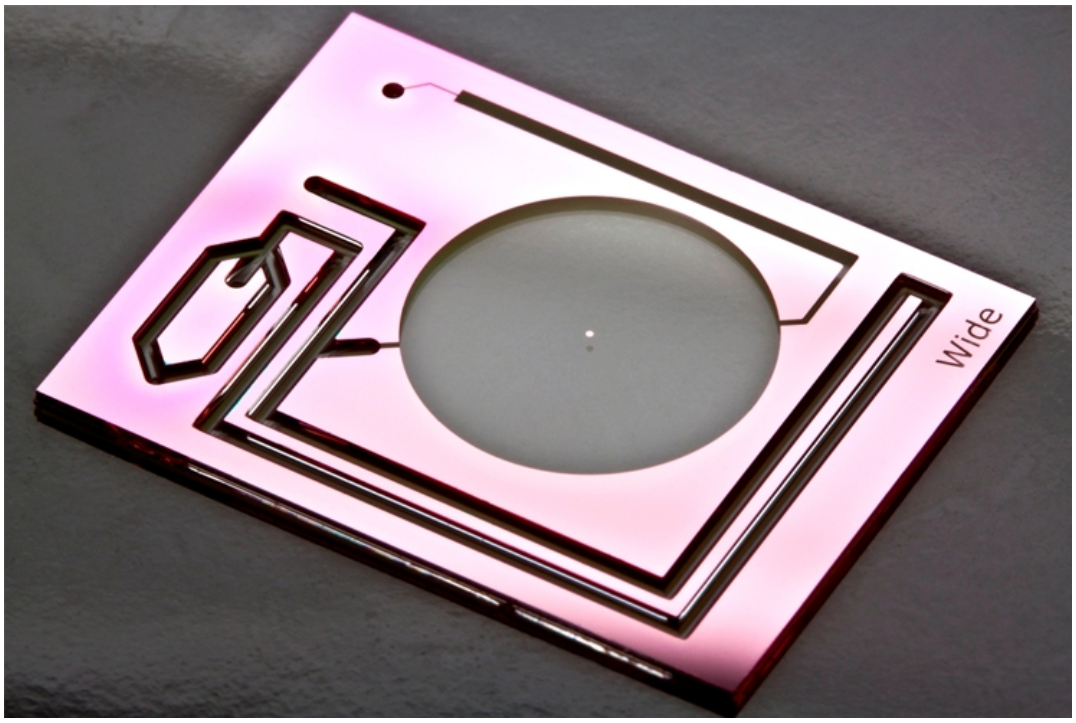

Fig. 5.2 Pyrex with a thin silicon layer (~200 nm) and the etched channel structures. This part is anodically bonded with a Pyrex lid in order to obtain a sealed Pyrex transparent μ-reactor.

The Pyrex/silicon//Pyrex is the second generation of transparent μ-reactor. The first attempt to make a transparent reactor was actually based on using fused quartz instead of one of the Pyrex lid (Quartz/silicon//Pyrex). The reason is that the use of quartz offers an advantage in the fabrication process. Pyrex is a borosilicate glass that contains many "impurities", mainly boron, sodium and aluminum. Unfortunately, because of this it does not pass the cleanness requirement of many chambers in the cleanroom facility of Danchip, where the μ-reactors are normally fabricated. As a consequence, the silicon layer cannot be grown on Pyrex in our university, but only sputtered. This way of depositing the silicon layer by sputtering, forms more rough surfaces and may cause problem in the bonding where smooth surfaces are preferable.
A little modification of the anodic bonding procedure is necessary with the quartz reactor. Since quartz is an electric insulator, the quartz chip needs to be slightly longer (21 x 16 mm) while the Pyrex lid with the usual dimension (20 x16 mm). In this way part of the polysilicon is not covered by the Pyrex and can be contacted directly with a gold wire. The first attempt to bond these quartz reactors showed negative results. Many chips broke immediately after bonding and some of them after a night without any reason. Only a couple of reactors were successfully bonded, but unfortunately without reproducibility. The main reason that most likely contributes to these failures is the difference in thermal expansion of quartz with respect to silicon and Pyrex. The linear coefficient of thermal expansion (CTE) at 20˚C is similar for silicon and Pyrex, 2.6 10^{-6}/°C and 3.3 10^{-6}/°C respectively, while for fused quartz is 0.59 10^{-6}/°C. Since the

bonding requires high temperature, the difference in the CTEs could produce thermal stress in the device and cause the cracking of the chip. A slightly higher rate of success was observed bonding a reactor with a different channel structure. This kind of reactor was designed with only one input channel, leaving more unetched area, and so more area that was anodic bonded. It might be that in this case the device was more robust to the stress. However, due to the intrinsic fragility of this kind of reactor, it was decided to remain with the Pyrex/Silicon//Pyrex design. Luckily, we could start a collaboration with CSEM in Neuchatel, where polysilicon could be grown on Pyrex thanks to a dedicated furnace.

The hot anodic bonding of the Pyrex μ-reactor did not cause any problems. Particularly useful is the fact that now, since the Pyrex becomes conductive at the temperature of the bonding, the polysilicon does not need to be contacted to ground, but the potential ofr the bonding can be applied by using the bottom plate and the top contact to the other Pyrex, as it is normally done with the silicon based μ-reactor. To have the two parts of the device with the same dimensions has the two advantages of being easier to handle the device before bonding and the hot bonding procedure is easier because it does not require the gold wire. A longer time it is anyway necessary with this design, probably because of the low conductivity of the Pyrex. Indeed, the time of the bonding is strongly decreased if, instead of a point top contact, an extended metal contact that covers more area on the Pyrex is used.

The cold bonding presented more challenges. In the case of the transparent reactor, the cold finger, that has the extra function to work as a contact to ground the bottom side of the chip, is touching the bottom Pyrex chip. In this way, the Pyrex is kept at low temperature, but unfortunately at this temperature it is not conducting. In order to solve this problem, a first attempt was tried where the reactor was clamped with two ceramic bars to the aluminum block that contains the heating bulbs. A gold wire was inserted between one of the bars and the bottom Pyrex, so that the wire was contacting a hot part. Unfortunately, this was not enough, and the reactor could not bond completely and often it cracked. In order to extend the area of electrical contact, a metal foil was used obtaining a partial success. The electrical contact was further improved by the use of a conductive silver paste, which was painted on the bottom of the Pyrex chip apart from the area corresponding to the reactor chamber where the cold finger is going to be positioned. The silver paste is grounded with the gold wire that is clamped together with the reactor with the ceramic bars. Furthermore, the temperature of the bonding was reduced by reducing the voltage applied to the heating lamps, in order to decrease the thermal gradient and the associated stress between the cold part of the Pyrex and the hot one. The decrease in temperature gave rise to slightly longer bonding time (3h total time), because the conductivity of the Pyrex is depending on the temperature. The condition for the silver paste cold bonding were: 15˚C (the temperature of the cooling water that keeps the cold finger at low temperature), 17 V (applied to the two heating halogen lamps connected in series) and 1.04 kV (the bonding potential). With these parameters a number of successfully bonded reactors were obtained. The silver paste dries completely during the bonding process, and can be easily removed from the back later.

5.3 Transparent µ-reactor: measurements

The first advantage of the new transparent µ-reactor is the possibility to measure the absorbance of the catalyst that has been previously loaded inside the reactor. In photocatalysis, two kinds of measurements are typically used to measure the absorbance: transmission and diffuse reflectance.

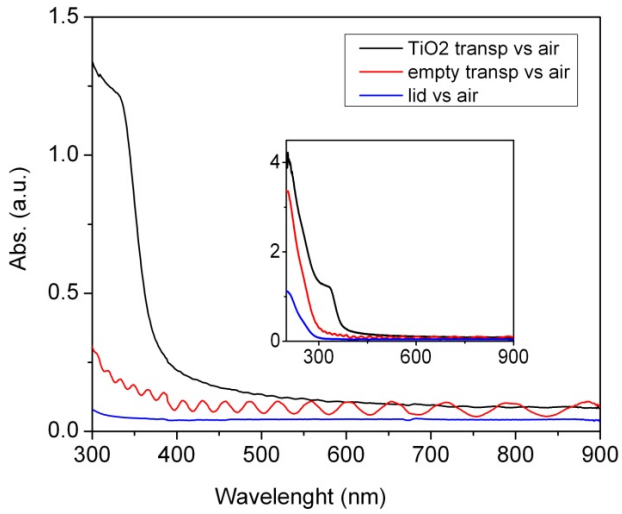

Fig. 5.3 Absorbance from UV-vis transmission measurements of a Pyrex lid (blue), an empty transparent µ-reactor (red) and a transparent µ-reactor loaded with a thin film of TiO_2 (black).

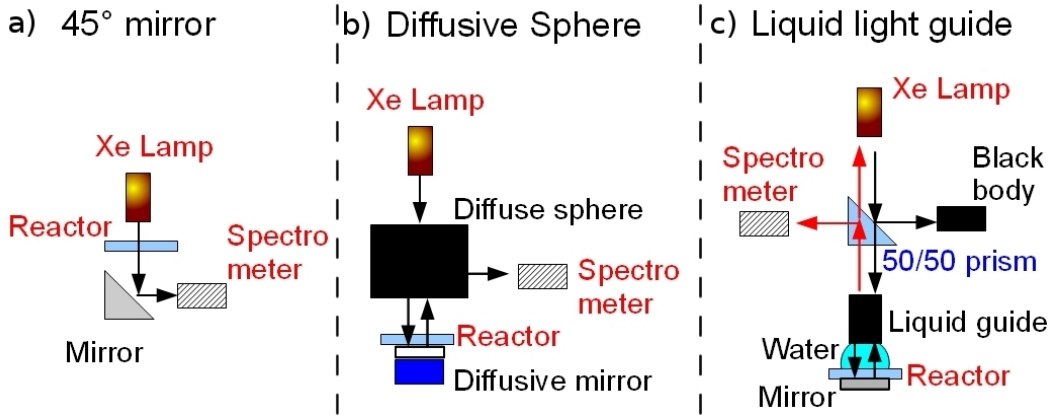

Fig. 5.4 Three different setup configurations for in situ Uv-vis measurements with a µ-reactor. A 45° mirror is used for optical transmission measurements (a) while a diffusive sphere and a diffusive mirror for a diffuse reflectance measurements (b). A 50/50 prism, a liquid light guide, a water meniscus and a mirror has been used for an alternative reflectance measurement (c).

In a transmission measurement, the transmitted light that passes through the catalyst is collected and compared with a reference spectrum taken without the catalyst. The light that does not pass is assumed to be absorbed. This is only valid if reflection and

scattering are negligible, because this method does not make any distinction between scattered and absorbed light. Therefore, this method is useful for thin films of catalyst, where the scattering is negligible compared to the absorbance.
In Fig. 5.3 two measurements of absorbance are plotted for an empty transparent reactor and a reactor with a thin layer of TiO_2 using an empty beam line (air) as a reference. The TiO_2 is deposited by spin coating the suspension of w2730x TiO_2 from Evonik. The measurements are done using a Cary 1E Spectrophotometer. The absorbance of the chip loaded with TiO_2 is perfectly in agreement with the literature.

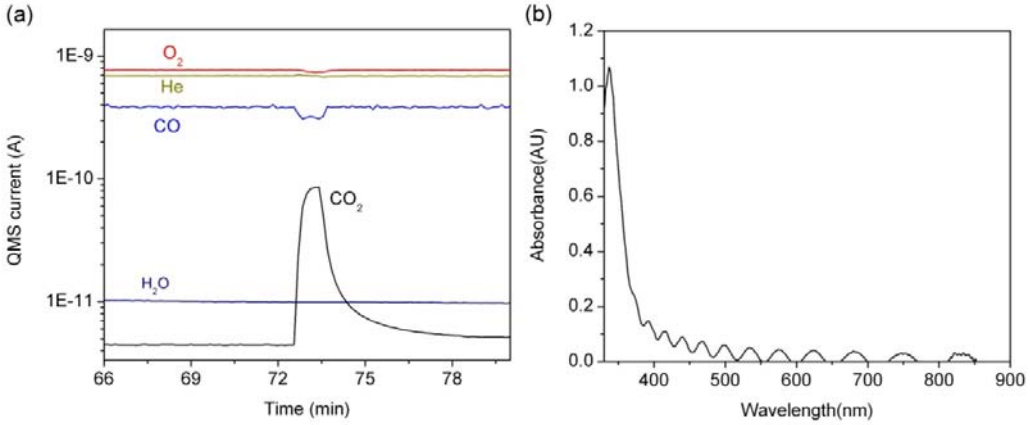

Fig. 5.5 Photocatalytic CO oxidation and in situ UV-vis absorbance using a transparent µ-reactor loaded with a thin film of TiO_2. The QMS currents for He (m/z = 4), O_2 (32), H_2O (18), CO_2 (44) and CO (28) are shown as a function of time. The absorbance measurement has been taken during the photooxidation of CO to CO_2 illuminating the sample with a 1 kW Xe lamp. An empty transparent µ-reactor has been used as a reference for the absorbance measurements.

The scattering from the thin film and the reflection of the Pyrex are negligible and only slightly increases the background from the level of zero absorbance. If the purpose of the measurement is to investigate features at shorter wavelength than 300 nm, where the Pyrex starts to absorb, some difficulties may arise. It is not simple to subtract the right background, because as can be seen in Fig. 5.3 in the case of an empty chip an oscillating signal is overlapping to the absorbance. This signal is the results of thin-film interference of the light reflected multiple times in the empty reactor. The formula for light interference in the case of a thin gap of air between two flat Pyrex glasses is:

$$2\,t = m\,\frac{\lambda}{2} \tag{5.1}$$

where t is the thickness of the air layer, λ the wavelength of light and m an integer that is even for constructive and odd for destructive interference. Using this formula on the absorbance of the empty µ-reactor measured in Fig. 5.3, we can assign the integer m to every peak and minimum and calculate the thickness t. The value obtained is ~3.76 µm, in good agreement with the expected value of 3.7 µm (the depth of the reactor is the etched depth in the Pyrex, 3.5 µm, plus 200 nm from the Si layer.). This effect is negligible in the case of loaded reactors, probably due to a small but finite scattering of the nanoparticles that is disturbing the interference. A single Pyrex lid can be used to attenuate and reduce the background due to the Pyrex. However, as said before, there is

basically no background contribution from the Pyrex at wavelength longer than 300 nm. This measurement can also be done in situ. A proof of concept was performed using the same μ-reactor loaded with TiO_2 and photocatalytic CO oxidation as a test reaction. The light illuminated the sample from the top, using an optical fiber connected to a 1 kW Xe arc lamp (Newport model 66 924). Under the reactor, a silver mirror tilted at an angle of 45˚ directs the transmitted light to the detector (a calibrated spectroradiometer, International Light model RPS-900R) (Fig. 5.4 a). The mirror would not be necessary if the detector could be placed under the reactor, in line with the optical fiber of the Xe lamp. In this case, the same light source is used as the probe for the absorbance measurements and the driving light of the photocatalytic reaction. The data of the experiments are shown in Fig. 5.5. The sample is active for CO oxidation, as can be seen from the consumption of CO and O_2 and the evolution of CO_2, as expected [75]. At the same time, the absorbance is recorded using an empty reactor as reference (unfortunately causing the oscillatory behavior shown in Fig. 5.5b). The reference spectrum has been taken before the starting of the experiments placing the transparent empty chip in the manifold block. The comparison of this absorbance with the one taken ex situ with the Cary shows a very good agreement between the two measurements (Fig. 5.6). This experiment is only a proof of concept, because nothing is expected to change in the absorbance during the reaction. More experiments involving other materials are planned and undergoing during the writing of this thesis.

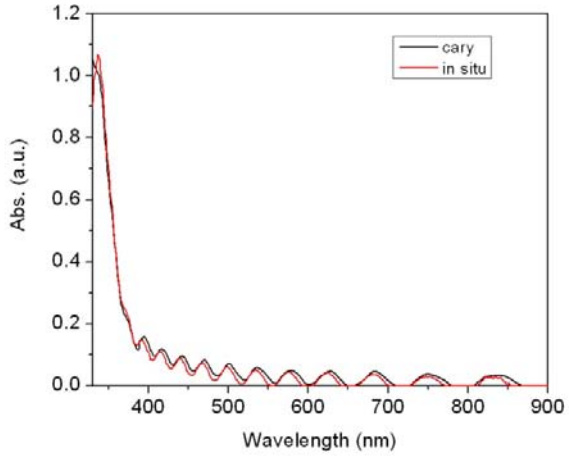

Fig. 5.6 Comparison between UV-vis light absorbance of a transparent μ-reactor loaded with a thin film of TiO_2 performed in situ (red) with the reactor mounted on the manifold block and ex situ (black) in the Cary 1E spectrometer.

For a layer of nanoparticles with the thickness in the μm range the scattering is often significant and so transmission measurements are not the best option. In this case, the best estimation of the absorbance is obtained with diffuse reflectance measurements. The diffuse reflectance sphere used in our experiments has an external cylindrical shape with a hole of 8 mm in the bottom against which the reactor with the catalyst can be placed (Fig. 5.4 b). An optical fiber connected to the top of the sphere illuminates the catalyst. A second optical fiber connected from the side of the sphere to a detector collects the diffuse light (the reflected and scattered components) from the sphere. A diffusive mirror is placed under the catalyst to assure that the light that is transmitted through the catalyst or that is scattered in the forward directions is sent back into the

sphere. The detector then measures the diffusely scattered light. This method can be used also with thin films.

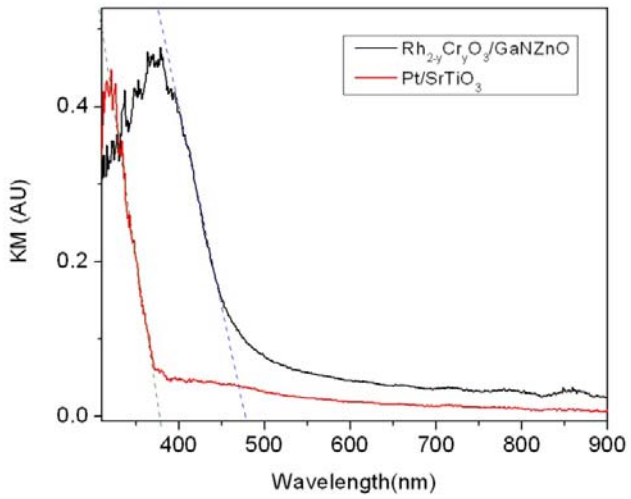

Fig. 5.7 Diffuse reflectance spectra of a transparent μ-reactor loaded with $Pt/SrTiO_3$ (red) and $Rh_{2-y}Cr_yO_3/GaN:ZnO$ (black).

Also in this case, a lid is used as a reference instead of an empty transparent reactor, in order to avoid the oscillating interference. This method to measure absorbance works perfectly, as can be seen from the example in Fig. 5.7 for reactors loaded with $Rh_{2-y}Cr_yO_3/GaN:ZnO$ and $Pt/SrTiO_3$.

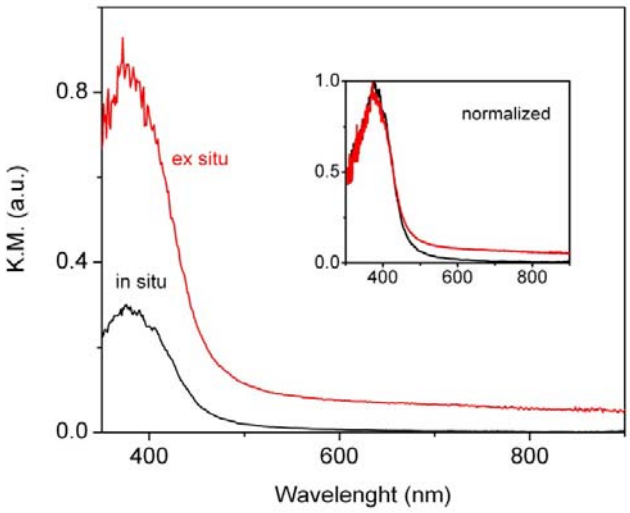

Fig. 5.8 Comparison between the diffuse reflectance of a transparent μ-reactor loaded with $Rh_{2-y}Cr_yO_3/GaN:ZnO$ performed in situ (black) with the reactor mounted on the manifold block and ex situ (red) with the reactor in close contact with the diffuse sphere. In the insert the two spectra have been normalized to 1.

To perform a diffuse reflectance measurement during a reaction is more complicated

than the transmission case. The main problem is that the sphere cannot be positioned in contact with the reactor. This is due to the fact that the reactor is kept in place in the manifold by a bar that creates an obstacle to the placement of the diffusive sphere. Therefore, part of the light that is scattered by the sample does not enter the sphere again, escaping by the side, and is not detected. However, a preliminary attempt to measure in situ diffuse reflectance was performed with a reactor loaded with $Rh_{2-y}Cr_yO_3$/GaN:ZnO, in order to estimate how bad this problem was. Quite surprisingly it was possible to measure the absorbance during the reaction. With a small metal cylinder with 1 cm of internal diameter placed between the sphere and the reactor the signal increases slightly. However, the absolute value of the K.M. absorbance is much smaller than the ex situ measurement. A comparison is shown in Fig. 5.8.
This method for in situ diffuse reflectance measurements is working at a preliminary stage. Some modifications are required in order to improve the sensitivity and reliability of the measurements.

A third approach to try to overcome these difficulties for in situ measurements was tried together with Peter Vesborg. The setup is sketched in Fig. 5.4 c. The light from the Xe lamp is split by a 50/50 beam splitter. Half of the light is lost and the other half is sent to a liquid light guide. The other end of the guide ends exactly on top of the reactor. A water meniscus between the reactor and the guide assures a good refractive index matching. A diffusive mirror is placed under the reactor. In this way the light is collected back with the same fiber and when it arrives to the beam splitter, it is sent to a detector. This method has the advantage to collect the light very close to the reactor. Unfortunately, the first attempt did not produce the wanted results and it was impossible to measure in situ absorbance. The reason was probably the wide aperture of the light guide (8 mm). This approach might also be considered in the future for optimization.

The experiments described in this chapter were performed using UV-vis light. The transparent μ-reactor is also transparent to IR radiation, but unfortunately only to the near infrared (NIR) part.

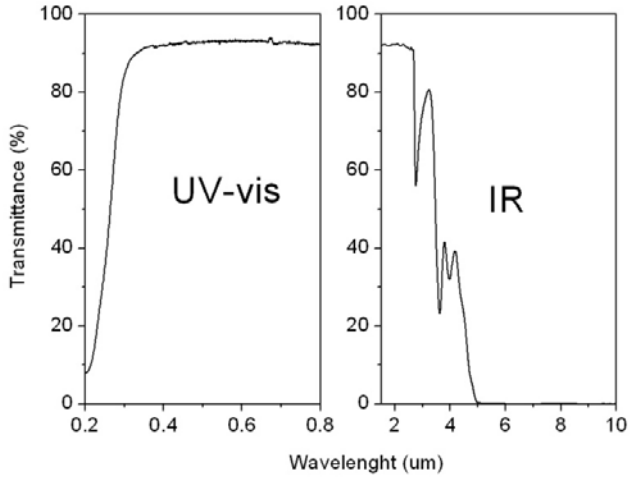

Fig. 5.9 UV-vis transmittance and IR transmittance of a Pyrex Lid (500 nm thick).

The full transmission spectrum of the Pyrex lid extended to the infrared range is shown in Fig. 5.9. The spectrum is obtained combining two measurements that I have done with the UV-vis Cary 1E spectrometer and the Thermo Nicolet Nexus FTIR spectrometer.
As anticipated, unfortunately, almost all of the interesting vibrational and rotational frequencies that are studied by infrared spectroscopy are in the middle infrared region (Mid IR). In the NIR range there are only the signatures of the overtones and the combinations of the fundamental bands that are in the Mid-IR. These signals are broader and weaker, and can easily overlap with each others creating a figure that is very complicated to analyze. The conclusion is simply that Pyrex is a bad material for Mid-IR study. Sapphire (Al_2O_3) is a much better window for the mid-IR region and is often used for this purpose. Another way to combine the IR spectroscopy with the μ-reactor is based on the use of attenuated total reflectance (ATR). For example a standard silicon based μ -reactor and a silicon ATR crystal might be used for Far-IR.

To summarize this part, we have seen that with the transparent μ-reactor is possible to perform UV-vis absorbance measurements before and after the reaction, and in some cases even during the reaction. There are several advantages associated with this combination of techniques. The sample doesn't need to be transferred out of the reactor, decreasing strongly the risk of contamination. The absorption measurement can be done in situ after a treatment, without exposing the reactor to air where the status of the catalyst can change, i.e. by oxidation. Furthermore, the amount of material is exactly the same for both the activity measurements and the optical characterization, obtaining a more precise comparison between the data acquired with the two kinds of experiments. Similarly, other optical techniques can be in principle efficiently combined with this μ-reactor, i.e. indirect nanoplasmonic sensing, Raman spectroscopy with probing light in the UV or visible range, photoluminescence and photoluminescence excitation spectroscopy.
Another interesting feature is that one can in theory synthesize a material inside the reactor after loading only the precursor, then characterize it with optical techniques, and finally test it. Of course the synthesis is limited to few methods, mainly solid state methods, and in particular to moderate temperatures, probably below 500˚C. The natural extension of this kind of reactor would be a quartz reactor. The anodic bonding will not work in this case, and a new technique has to be developed. However, in that case the nitridation that is usually performed at high temperatures could be performed in situ. This reaction is particular interesting since it is the way to make oxynitrides and nitrides that, at the present stage, are considered one of the best candidates for solar photocatalytic water splitting for a one step excitation device.

5.4 Interfacing an opened μ-reactor with a UHV chamber

In the previous paragraph we have seen that the transparent μ-reactor opens new possibilities to integrate many optical techniques with photocatalytic activity measurements. These techniques can characterize the catalyst and provide useful information. Unfortunately, as mentioned before, most of the surface science techniques are impossible to be used combined with the standard silicon based μ-reactor or the new transparent μ-reactors. Therefore, in this paragraph will be discussed a different strategy

that was followed in order to try to combine UHV surface science techniques, i.e. x-ray photoemission spectroscopy (XPS), and the μ-reactor technology. In particular, the purpose of this project was to build a setup that allows characterizing with surface science techniques a catalyst after a photocatalytic reaction without exposing the catalyst to air after the reaction. The information obtained with this method are interesting because for numerous system is not clear what exactly is the status of the catalyst during the reaction and exposure to air can alter the status of the catalyst.

Fig. 5.10 An open μ-reactor mounted on the manifold block obtained from a 2 ¾ inch stainless steel flange for UHV application.

In order to build such a setup, the reactor cannot be permanently closed, as explained before. Therefore, it was decided to make a reactor that is similar to the silicon based μ-reactor, but has the bottom of the reactor chamber removed. The silicon part has the same channel structure but it does not have the four holes used to connect the channels to the gas lines. Furthermore, as mentioned, an extra hole of 1 cm in diameter is etched through the silicon removing the bottom of the reactor chamber. Unlike the standard silicon based μ-reactor, the four holes are made in the Pyrex, after that the two components are anodically bonded together. A polymer is deposited around the edge of the removed circular area, forming a torus with an inner radius of 5.1 mm, an outer radius of 5.3 mm and about 100 μm thick. This material has the function of sealing the chamber when the reactor is pressed with a stainless steel frame. The catalyst is not deposited in the reactor, but on the metal frame. In this way, the reactor can be used multiple times, because different catalysts can be placed on several frames and can be put in contact with the reactor one after each other. As a first tentative material for the sealing ring, the SU-8 2000 epoxy photoresist from MicroChem was chosen. The reasons of this choice were that SU-8 is a very well known material, used frequently in microelectronic applications and so easy to pattern into the desired shape. For this reactor, the total volume of the reactor chamber is at least equal to ~27.7 μl, and thus two orders of magnitude bigger than the volume of the standard silicon based μ-reactor (240 nl). The new volume is obtained adding 27.5 μl, that is the volume of the removed

silicon, to 240 nl. The volume due to the compressed SU-8 is more difficult to estimate but in principle it should be also added to the 27.7 µl. The decrease in sensitivity due to the bigger volume can be partially compensated by loading more material. Indeed, now the layer of catalyst can be thick enough to absorb almost all the incident light.

Due to the sealing by pressure the reactor needs to stand on a flat surface, unlike the standard reactor that is mounted on the manifold block on a single side and is extended in air. Therefore, the block was redesigned. After a couple of iteration, it was decided to proceed with the design shown in Fig. 5.10. The block has been obtained from a standard 2 ¾ inch stainless steel flange for UHV application. In this way it is easy to configure the device with UHV apparatus. The reactor stands in the center of the flange with the Pyrex side in contact with the flange. A hole of 1 cm of diameter has been etched all the way through the flange in correspondence of the reactor chamber. On the bottom side of the flange, a 1 1/3 inch quartz viewport is mounted with screws and allows illuminating the catalyst when the reactor is closed. Four holes and four channels are etched in the flange to connect the reactor with the inlet gas lines and the output lines. The four channels ends on the side of the flange where four tubes ending with VCR connections have been soldered. Four Kalrez o-rings are placed under the four holes of the reactor. The sealing of the reactor to the flange has been kept as similar has possible with the standard one. So a bar with two screws is pressing the reactor to the flange. Another bar has been placed at the other end to help keeping the reactor in place and to align it.

Fig. 5.11 Metallic frame sample holder that is used to seal the open µ-reactor. The area where the catalyst should be deposited is colored in yellow.

The flange is mounted at the bottom of a vertical load lock. Thanks to a preexisting vertical garage in the load lock, up to 16 samples can be accommodated without the need to open the load lock to air. The garage can be moved up and down until it reaches the flange with the reactor. In the bottom of the garage, a sample holder was built where it is possible to insert the metallic frames coated with the catalysts.
The shape of the metallic frame has to obey to many constraints in order 1) to fit in the garage, 2) to be centered on top of the reactor chamber and 3) to be able to go in contact with the SU-8 ring. The top part is flat so that it can be inserted in the holder by sliding

two lateral wings into the tracks of the holder, while in the bottom there is a small cube placed slightly off-center (Fig. 5.11). This is due to the fact that the reactor chamber is not placed in the center of the reactor and the reactor has to be placed centered on the flange, since this is the only way it can fit. This creates several troubles in the alignment.

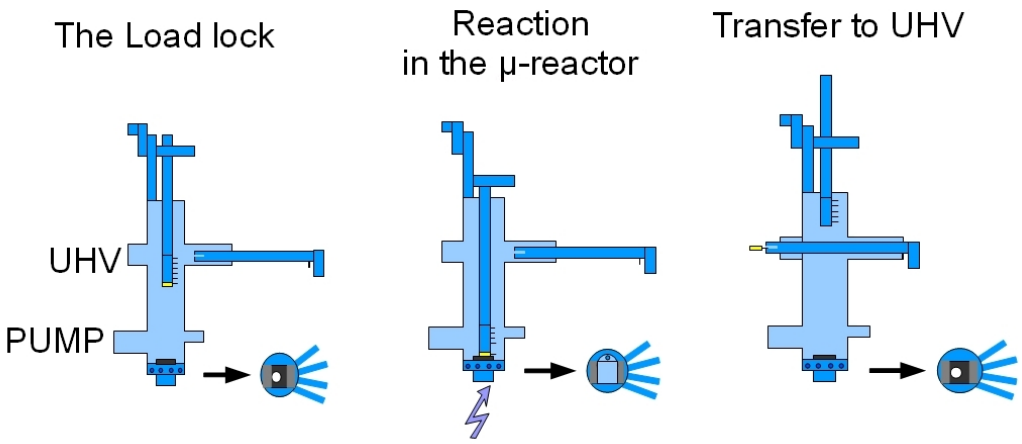

Fig. 5.12 Steps for a standard experiment combining photocatalytic reactivity tests and UHV surface science analysis. A side view of the load lock is shown together with a top view of its bottom part, where the open µ-reactor sits. During the photocatalytic reaction the reactor is sealed by the metallic sample holder and the sample is illuminated. Afterwards the load lock is pumped down and the sample can be transferred to UHV with a wobblestick grab.

The cube of the metal frame needs to be thick enough to reach the SU-8 ring, thicker than the bar that keeps the reactor in place, but thin enough to be able to be inserted in the other positions in the garage. The catalyst can be placed with the standard techniques on the bottom surface of the cube. The area of the surface of the cube (1.2 cm x 1.2 cm) is not too much bigger than the reactor chamber (the SU-8 ring is placed around the reactor chamber that has already 1 cm of diameter!!!), so the alignment needs to be extremely accurate.
There are a couple of features made in order to make that difficult task easier. An extra flange with a cylinder guide is placed on top of the flange with the reactor, helping to keep the garage centered when it approach the bottom flange. The alignment in the plane of the reactor can be checked roughly by looking through the quartz window when the sample is approaching the reactor. In case the sample holder is not in position, the metallic lid can be moved in the sample holder in one direction so that a better alignment can be achieved.
The load lock is connected with a big UHV chamber that is equipped with surface science tool to perform XPS and ion scattering spectroscopy (ISS). The sample can be transferred to the other chamber with a wobblestick grab that has a pin that matches a hole in the steel sample holder.
The idea of this project is shown in Fig. 5.12. First the sample can be transferred to UHV chamber and analyzed with XPS. Then it can be transferred back in the load lock and pressed against the reactor. Here the photocatalytic experiments can be performed. After the experiment, the load lock can be pumped and then the sample transferred to the UHV chamber and characterized with XPS after reaction. All the transfers of the

sample are done in vacuum or under a controlled atmosphere.

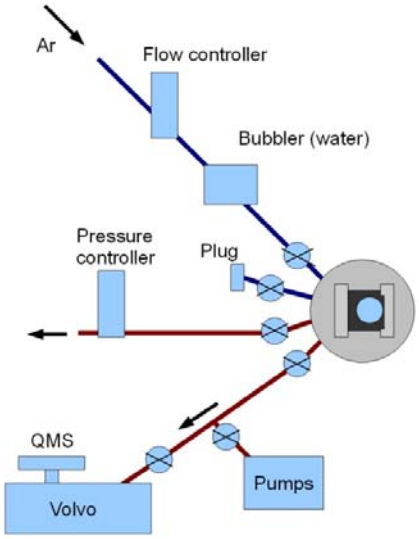

Fig. 5.13 Drawing of the setup for photocatalytic experiments with the open μ-reactor.

In order to perform the photocatalytic reaction, a simple setup inspired by the one that we are normally using was built. A scheme is drawn in Fig. 5.13. For the preliminary experiments, only one gas inlet line was used, while the other one was closed by a plug. The inlet line is connected to an Argon bottle. The flow of argon is controlled by a conventional MFC, and the gas is used as a carrier bubbling it through a new bubbler. This bubbler has a quartz window, so the level of water can be monitored and the bubbler can be opened to change the content only if necessary.
The main outlet line goes to the pressure controller as in the other setup. The outlet for the products detection goes into the main UHV chamber. Attached to the chamber there is a QMS that it is used for detection of the products. This line is also connected to an auxiliary turbo pump that is used instead of the turbo of the main UHV chamber when the line needs to be pumped. A valve can close the way to the pump during the experiment, so that all the products go into the UHV chamber for detection.
The setup was tested with a closed silicon based μ-reactor loaded with Rh_2-$_yCr_yO_3$/GaN:ZnO. This experiment was designed to check if the part of the setup dedicated to perform photocatalytic experiments was working, so the garage and the load lock were not involved. For this purpose, an old reactor was used and four holes etched in the lid in order to place the reactor in the new setup. The holes in the silicon side were closed covering that entire surface with a blue tape. The UV LED was used as light source to test the photocatalytic water splitting reaction. The results are shown in Fig. 5.14. The photocatalytic evolution of H_2 and O_2 was confirmed. This was the first photocatalytic experiment performed using that chamber (which is also known as "Volvo").

The next step is trying to repeat the experiment with an open μ-reactor. For this reason,

an open μ-reactor was mounted to the flange and the flange to the load lock. Unfortunately, many chips broke due to an excess of pressure during the sealing procedure, and in some cases, no gas could be measured in the UHV chamber. In principle, silicon is very difficult to break if it lays on a flat surface. However, it is very easy to break into pieces if you bend a part of it. The reactor should lay flat on the flange. However, in a side there are the four o-rings that even under compression can still create a finite thickness. As a consequence the reactor is not perfectly flat.

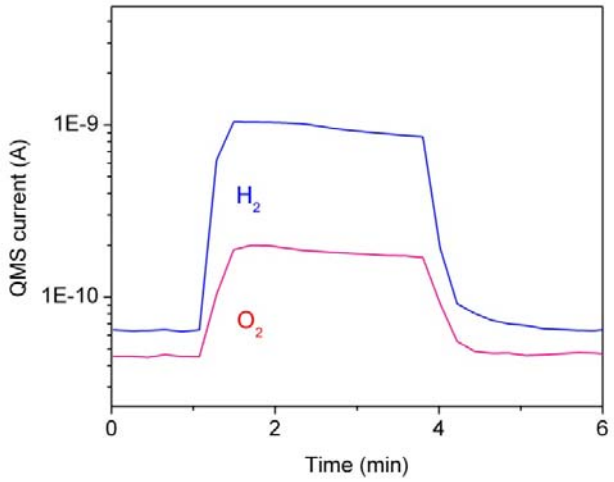

Fig. 5.14 Photocatalytic water splitting with a μ-reactor loaded with $Rh_{2-y}Cr_yO_3$/GaN:ZnO using the setup of Fig. 5.13. The QMS currents for H_2 (m/z = 2) and O_2 (32) are shown as a function of time (UV LED, λ ~ 367 nm, ~ 460 mW/cm^2). Ar has been used as carrier gas for the water vapor. The gas was flowing through holes etched in the Pyrex while the holes in the silicon have been closed by tape.

An attempt to improve this aspect has been done adding o-rings in other part of the flange below the reactor with the function of dump the eventual mechanical stress. However, this modification did not prove to be enough. Another significant problem is that, even if the metallic cube with the sample should be parallel to the reactor, it might not be the case. The solution to this problem might consist in placing a spring between the metallic sample holder and the garage. Another thing that can be improved is that at the moment, the pressure applied to seal the reactor is not measured. This could be useful to prevent the breaking of chips and assure reproducibility. Therefore, it was considered to combine a load cell (tension transducer, model TCTN-9110 from Nordic Transducer) with the setup.
Another strategy can be to try different materials as replacement of the SU-8 ring and design experiments focused to test how well these materials can seal the chamber.
This project is still open, but the work can continue based on the starting blocks and knowledge that have been developed so far.

5.5 Summary and conclusion – Chapter 5

This chapter discussed two attempts to design new kind of μ-reactors that can combine

photocatalytic measurements and in situ characterization.
In the first paragraphs, a new μ-reactor that has Pyrex lid on both side of the reactor chamber and is transparent for light with UV-vis-NIR wavelength is described. The two lids are bonded together by anodic bonding thanks to a layer of polysilicon grown on one of them. Due to the different properties of the Pyrex with respect to silicon, the cold bonding procedure has been modified by using a gold wire, conducting silver paste and lower temperature. In that part of this chapter, a previous design that was based on quartz (fused silica) is also discussed. The problems connected with the fragility of the quartz reactor due to thermal coefficient of expansion mismatch were solved by using Pyrex in the current design.
After the description of the design of the reactor, three different setups that can measure the absorbance of the catalyst after or during a catalytic reaction are discussed. The first one is working in transmission and it is dedicated to thin films. In situ measurements can be obtained and an example is shown for photocatalytic CO oxidation with TiO_2.
The second consists in using a diffuse reflectance sphere to measure the Kubelka Munk function. This setup solves the limitation of the previous one because it is possible to use with thick film of nanopowders. It can measure the absorbance of the catalyst before and after photocatalytic reaction or heat treatments. Even if in situ measurements can be obtained while running a reaction, the configuration is unfortunately not optimal for this kind of experiment, because the sphere cannot be placed in direct contact with the reactor.
The third setup is an attempt to approach the possibility to obtain in situ measurements without the diffuse reflectance sphere but using a liquid light guide. This is placed exactly on top of the chamber and the light collected by the same fiber is sent to a detector thanks to a beam splitter. At the moment, this setup is not performing as well as expected and it therefore needs to be optimized.
The last paragraph treats the attempt to combine a μ-reactor with surface science tools to analyze the surface of the catalyst before and after reaction. In order to achieve this goal an open μ-reactor is necessary. A new setup similar to the one used for experiments with standard μ-reactor has been built and it is working. However, preliminary experiments show some difficulties in sealing the open μ-reactor by pressure. These problems can be overcome by more control of the sealing procedure.

Chapter 6

General conclusion and outlook

This thesis has treated the gas phase photocatalytic water splitting reaction using μ-reactors. With this technology, several catalysts have been tested and their activities compared for the overall reaction and the production of H_2 and O_2. This is, obviously, the first necessary step in order to design a catalyst system able to run solar-driven water splitting.
From the study of the fundamental mechanism of the reaction, an expression for the rate of H_2 and O_2 evolution has been obtained. For typical water splitting conditions, the rate shows a linear dependence as a function of the intensity of the photon flux and of the relative humidity. The relative humidity, and not just the water partial pressure, is the key parameter for obtaining high activity for the gas phase reaction. In fact, the dependence of the activity on relative humidity includes a linear dependence on water partial pressure but also an inverse proportionality with respect to the temperature of the reactor.
The formula for the rate includes also a parameter to take into account the dependence on the wavelength and eventually other contributions that depend on the temperature.
Among the system tested, $Rh_{2-y}Cr_yO_3$/GaN:ZnO shows high activity for gas phase water splitting considering the photoresponse that extends into the visible light range, in agreement with what have been found in liquid phase experiments.
Water splitting back reaction experiments have been carried out testing GaN:ZnO loaded with several cocatalysts. These experiments consist in running the catalytic hydrogen oxidation reaction introducing a stoichiometric mixture of H_2 and O_2 at room temperature and measuring the water formation.
GaN:ZnO loaded with Cr_2O_3/Rh and $Rh_{2-y}Cr_yO_3$ show a strong suppression of the catalytic water formation rate with respect to Rh/GaN:ZnO. Similarly, the rate of water formation is strongly decreased for Cr_2O_3/Pt/GaN:ZnO with respect to Pt/GaN:ZnO. In both the cases, the suppression of back reaction is clearly associated with an enhancement of the net gas phase photocatalytic water splitting rate for H_2 and O_2 evolution. Therefore, the suppression of the back reaction is a fundamental process that improves the net activity of photocatalysts for overall water splitting and can be obtained by photodepositing a Cr_2O_3 shell or coloading Cr.

A new Pyrex μ-reactor fully transparent to light in the UV-vis-NIR range has been developed. With this reactor is possible to combine photocatalytic experiments performed by measuring the products of a reaction with a QMS, with in situ optical characterization. The device has been designed and tested. In the thesis a couple of experiments were presented in order to show the working principles. These experiments show the two cases of in situ transmission and diffuse reflectance measurements as examples.

A new setup has been built in the attempt to combine photocatalytic activity measurements in a μ-reactor and analysis of the surface of the catalysts by XPS and other surface science techniques. Unfortunately, some issues have been found in sealing properly the new open μ-reactor necessary for this project. However, the part of the

setup dedicated to the photocatalytic measurements is working and hopefully the remaining problems can be solved in the future building on lessons from this my project.

6.1 Outlook

At the current status of the research, there are just a couple of materials that are known to work under visible light illumination for the overall water splitting reaction (GaN:ZnO and $ZnGeN_2$/ZnO). The final goal of the research for the photocatalytic water splitting reaction is to find active materials with a visible light response. In the one step excitation approach, the optimal band gap of these materials should be ~2.0-2.3 eV. Nitrides and oxynitrides are considered to be good candidates. Ta_3N_5 (band gap 2.1 eV), TaON (2.5 eV) and $LiTaO_2N$ (2.0 eV) are three examples.
A possible project could be to try the synthesis of these photocatalysts with different methods in the attempt to decrease the density of defects that is considered their main problem.
The search for new candidates is a difficult challenge. However, a screening based on DFT calculations could provide useful indications in finding new candidates [76].

A number of experiments have been carried out using GaN:ZnO. However, there are still plenty of interesting points that are not completely understood and that are worthy to be investigated. For example, the apparent quantum efficiency of GaN:ZnO, even in the best conditions in a liquid phase experiment, is still very low (5.1% at $\lambda\sim$ 410 nm for $Rh_{2-y}Cr_yO_3$/GaN:ZnO). It would be extremely interesting if this efficiency can be increased, since this material can in principle absorbs up to ~6% of the photons coming from the sun. Furthermore, a better understanding of the origin of its visible light response might be useful to design new catalysts with a narrower band gap.
Most of the limitations associated with the GaN:ZnO seem to originate from a high presence of defects. Therefore, studying the process of its synthesis, for example with techniques that have access to information during the nitridation process, might help to synthesize a material with a higher crystallinity.
Another interesting project can be to use GaN:ZnO, which it is known to show high activity (i.e. when loaded with $Rh_{2-y}Cr_yO_3$, Cr_2O_3/Rh,...), as a model photocatalyst to try to develop better and less expensive cocatalysts, i.e. no platinum group metals (PGMs).

It would be also very interesting to try different kind of protective shell for metal cocatalysts. The Cr_2O_3 shell might not be the best choice for all the cocatalysts, as it seems in the case of Pt. For example, there are other ways to suppress the water splitting back reaction and thereby enhance the photocatalytic activity that have been reported in the literature. It might be interesting to study these systems, i.e. iodine layer on Pt or the effect of adsorbed carbonate species (Na_2CO_3, ...).
The effect of codeposited Cr in the loading of a cocatalyst (i.e. in the case of Rh-Cr mixed oxide) is still not completely understood. A better knowledge of this system is of course very useful in designing active catalysts.

The Pyrex transparent μ-reactor could easily be combined with Raman spectroscopy and

help in the mentioned projects.
The development of a transparent μ-reactor based on Quartz and without Pyrex will extend a lot the potential of the transparent μ-reactor. With the quartz reactor one could synthesize the catalysts with methods that require high temperatures, i.e. by NH_3 nitridation, directly in the reactor, measure its absorbance in situ, perform in situ Raman spectroscopy (this possibility has still to be proven) and test the photocatalytic activity for water splitting.

In the project regarding the open μ-reactor there are still a number of experiments that can be tried. Sealing properly the reactor is the limiting step at the moment. Possible solutions consist in trying different o-ring materials (i.e. softer materials) and improve the way the metal frames with the catalysts is approaching and pressing on the SU-8 o-ring. This can be done including a spring loaded frame holder and using the tension transducer.
If this step is accomplished, then it would be interesting to try to reduce the volume of the reactor chamber, in order to increase the time sensitivity.

Bibliography

[1] http://www.census.gov/population/popclockworld.html
[2] BP Statistical Review of World Energy June 2012. *www.bp.com/statisticalreview*
[3] R. L. Hirsch, *Atlantic Council Bulletin*, 2005, Vol. XVI, No. 3.
[4] http://www.esrl.noaa.gov/gmd/ccgg/trends/
[5] H. Fischer, M. Wahlen, J. Smith, D. Mastroianni, and B. Deck, *Science*, 1999, **283**, 1712.
[6] http://data.giss.nasa.gov/gistemp/
[7] J. Hansen, M. Sato, R. Ruedy, K. Lo, D. W. Lea and M. Medina-Elizade, *Proc. Natl. Acad. Sci. USA*, 2006, 103, 14288.
[8] J. Houghton, *Rep. Prog. Phys.*, 2005, **68,** 1343.
[9] "Solar Energy Perspectives: Executive Summary". International Energy Agency. 2011. http://www.iea.org/Textbase/npsum/solar2011SUM.pdf.
[10] ASTM G173-03 Reference Spectra Derived from SMARTS v. 2.9.2
[11] J. Barber, *Chem. Soc. Rev.*, 2009, **38**, 185.
[12] K. N. Ferreira, T. M. Iverson, K. Maghlaoui, J. Barber and S. Iwata, *Science*, 2004, **303**, 1831.
[13] D.O. Hall, *Fuel*, 1978, **57**, 322.
[14] A. Fujishima and K. Honda, *Nature*, 1972, **238**, 37.
[15] M. Weber and M. Dignam, *Int. J. Hydrogen Energy*, 1986, **11**, 225.
[16] B. D. James, G. N. Baum, J. Perez, K. N. Baum, *Technoeconomic Analysis of Photoelectrochemical (PEC) Hydrogen Production*; U.S. Department of Energy, Final Report, December 2009. http://www1.eere.energy.gov/hydrogenandfuelcells/pdfs/pec_technoeconomic_analysis.pdf.
[17] K. Maeda and K. Domen, *J. Phys. Chem. Lett.*, 2010, **1**, 2655.
[18] T. R. Henriksen, J. L. Olsen, P. C. K. Vesborg, I. Chorkendorff and O. Hansen, *Rev. Sci. Instrum.*, 2009, **80**, 124101.
[19] P. C. K. Vesborg, J. L. Olsen, T. R. Henriksen, I. Chorkendorff and O. Hansen, *Rev. Sci. Instrum.*, 2010, **81**, 016111.
[20] P. C. K. Vesborg, S.-I. In, J. L. Olsen, T. R. Henriksen, B. L. Abrams, Y. Hou, A. Kleiman-Shwarsctein, O. Hansen and I. Chorkendorff, *J. Phys. Chem. C*, 2010, **114**, 11162.
[21] A. Kudo and Y. Miseki, *Chem. Soc. Rev.*, 2009, **38**, 253.
[22] K. Maeda, *J. Photochem. Photobiol. C: Photochem Rev.*, 2011, **12**, 237.
[23] K. Domen, S. Naito, T. Onishi, K. Tamaru, *Chem. Phys. Lett.*, 1982, **92**, 433.
[24] D.S. Deak, *Materials Science and technology*, 2007, **23**, 127.
[25] K. Domen, S. Nalto, T. Onlshl, K. Tamaru and M. Soma, *J. Phys. Chem.*, 1982, **86**, 3657.
[26] K. Sayama and H. Arakawa*, J. Phys. Chem.*, 1993, **97**, 531.
[27] G. Liu, H. G. Yang, X. Wang, L. Cheng, H. Lu, L. Wang, G. Q. (Max) Lu and H.-M. Cheng, *J. Phys. Chem. C*, 2009, **113***,* 21784.
[28] S. Tabata, N. Nishida, Y. Masaki and K. Tabata, *Catalysis Letters*, 1995, **34**, 245.
[29] K. Yamaguti and S. Sato, *J. Chem. Soc., Faraday Trans. 1*, 1985, **81**, 1237.

[30] S. Sato and J. M. White, *Journal of Catalysis*, 1981, **69**, 128.
[31] K. Sayama and H. Arakawa, *J. Chem. Soc., Faraday Trans.*, 1997, **93**, 1647.
[32] A. Fujishima, X. Zhang and D. A. Tryk, *Surface Science Reports*, 2008, **63**, 515.
[33] J. Zhang, Q. Xu, Z. C. Feng, M. J. Li and C. Li, *Angew. Chem., Int. Ed.*, 2008, **47**, 1766.
[34] J. G. Mavroides, J. A. Kafalas and D. F. Kolesar, *Appl. Phys. Lett.*, 1976, **28**, 241.
[35] K. Maeda, K. Teramura, D. Lu, T. Takata, N. Saito, Y. Inoue and K. Domen, *Nature*, 2006, **440**, 295.
[36] K. Maeda and K. Domen, *Chem. Mater*., 2010, **22**, 612.
[37] K. Maeda, T. Takata, M. Hara, N. Saito, Y. Inoue, H. Kobayashi and K. Domen, *J. Am. Chem. Soc.*, 2005, **127**, 8286.
[38] Y. Lee, H. Terashima, Y. Shimodaira, K. Teramura, M. Hara, H. Kobayashi, K. Domen and M. Yashima, *J. Phys. Chem. C*, 2007, **111**, 1042.
[39] K. Maeda, K. Teramura, T. Takata, M. Hara, N. Saito, K. Toda, Y. Inoue, H. Kobayashi and K. Domen, *J. Phys. Chem. B*, 2005, **109**, 20504.
[40] K. Maeda, K. Teramura and K. Domen, *J. Catalysis*, 2008, **254**, 198.
[41] S. H. Wei and A. Zunger, *Phys. Rev. B,* 1988, **37**, 8958.
[42] T. Hirai, K. Maeda, M. Yoshida, J. Kubota, S. Ikeda, M. Matsumura and K. Domen, *J. Phys. Chem. C*, 2007, **111**, 18853.
[43] E. J. McDermott, E. Z. Kurmaev, T. D. Boyko, L. D. Finkelstein, R. J. Green, K. Maeda, K. Domen and A. Moewes, *J. Phys. Chem. C*, 2012, **116**, 7694.
[44] K. Maeda, K. Teramura, N. Saito, Y. Inoue and K. Domen, Journal of Catalysis, 2006, **243**, 303.
[45] K. Maeda, N. Sakamoto, T. Ikeda, H. Ohtsuka, A. Xiong, D. Lu, M. Kanehara, T. Teranishi, and K. Domen, *Chem. Eur. J.*, 2010, **16**, 7750.
[46] K. Maeda, K. Teramura, N. Saito, Y. Inoue, H. Kobayashi and K. Domen, *Pure Appl. Chem.*, 2006, **78**, 2267.
[47] F. Dionigi, P.C.K. Vesborg, T. Pedersen, O. Hansen, S. Dahl, A. Xiong, K. Maeda, K. Domen and I. Chorkendorff, *Energy Environ. Sci.*, 2011, **4**, 2937.
[48] T. Hisatomi, K. Maeda, K. Takanabe, J. Kubota and K. Domen, *J. Phys. Chem. C*, 2009, **113**, 21458.
[49] K. Maeda, K. Teramura, H. Masuda, T. Takata, N. Saito, Y. Inoue and K. Domen, *J. Phys. Chem. B*, 2006, **110**, 13107.
[50] N. Agmon, *Chem. Phys. Lett.*, 1995, **244**, 456.
[51] J. M. Spurgeon and N. S. Lewis, *Energy Environ. Sci.*, 2011, **4**, 2993.
[52] I. Chorkendorff and H. Niemantsverdriet, *Concepts of Modern Catalysis and Kinetics*, Wiley-VCH, Weinheim, 2007, 456 pages, ISBN 3-527-31672-4.
[53] S.Brunauer, P. H. Emmett and E.Teller, *J.Am.Chem. Soc.*, 1938, **60**, 309.
[54] M. I. Tejedor-Tejedor, F. M. Vichi and M. A. Anderson, *J. Porous Mat.*, 2005, **12**, 201.
[55] S. Nakabayashi, A. Fujishima and K. Honda, *Chem. Phys. Lett.,* 1983, **102**, 464.
[56] R. Baba, S. Nakabayashi, A. Fujishima and K. Honda, *J. Phys. Chem.*, 1985, **89**, 1902.
[57] D. Wang, A. Pierre, M. G. Kibria, K. Cui, X. Han, K. H. Bevan, H. Guo, S. Paradis, A.- R. Hakima and Z. Mi, *Nano Lett*., 2011, **11**, 2353.
[58] F. Dionigi, P. C. K. Vesborg, T. Pedersen, O. Hansen, S. Dahl, A. Xiong, K. Maeda, K. Domen and I. Chorkendorff, *Journal of Catalysis*, 2012, **292,** 26.

[59] K. Maeda, K. Teramura, D. Lu, N. Saito, Y. Inoue and K. Domen, *J. Phys. Chem. C*, 2007, **111** 7554.
[60] K. Maeda, K. Teramura, D. Lu, N. Saito, Y. Inoue and K. Domen, *Angew. Chem. Int. Ed.*, 2006, **45**, 7806.
[61] S. Trasatti, *J. Electroanal. Chem.*, 1972, **39**, 163.
[62] J. K. Nørskov, T. Bligaard, A. Logadottir, J. R. Kitchin, J.G. Chen, S. Pandelov and U. Stimming, *J. Electrochem. Soc.*, 2005, **152**, J23.
[63] B. Hellsing, B. Kasemo and V.P. Zhdanov, *J. Catal.*, 1991, **132**, 210.
[64] E. M. Larsson, C. Langhammer, I. Zoric and B. Kasemo, *Science*, 2009, **326**, 1091.
[65] K. Domen, A. Kudo and T. Onishi, *J. Phys. Chem.*, 1986, **90**, 292.
[66] R. Abe, K. Sayama and H. Arakawa, *Chemical Physics Letters*, 2003, **371**, 360.
[67] K. Sayama and H. Arakawa, *J. Chem. Soc., Faraday T rans.*, 1997, **93**, 1651.
[68] Y. Sasaki, A. Iwase, H. Kato and A. Kudo, *Journal of Catalysis*, 2008, **259**, 133.
[69] M. Yoshida, K. Takanabe, K. Maeda, A. Ishikawa, J. Kubota, Y. Sakata, Y. Ikezawa and K. Domen, *J. Phys. Chem. C*, 2009, **113**, 10151.
[70] F. H. B. Lima, J. Zhang, M. H. Shao, K. Sasaki, M. B. Vukmirovic, E. A. Ticianelli and R. R. Adzic, *J. Phys. Chem. C*, 2007, **111**, 404.
[71] J. K. Nørskov, J. Rossmeisl, A. Logadottir, L. Lindqvist, J. R. Kitchin, T. Bligaard and H. Jonsson, *J. Phys. Chem. B*, 2004, **108**, 17886.
[72] M. Szklarczyk and J. O'M. Bockris, *J. Phys. Chem. C*, 1984, **88**, 5241.
[73] A. Fujishima, X. Zhang and D.A. Tryk, *Surf. Sci. Rep.*, 2008, **63**, 515.
[74] V.P. Zhdanov, *Surf. Sci.*, 1993, **296**, 261.
[75] P. C. K. Vesborg, J. L. Olsen, T. R. Henriksen, I. Chorkendorff and O. Hansen, *J. Chem. Eng.*, 2010, **160**, 738.
[76] I. E. Castelli, T. Olsen, S. Datta, D. D. Landis, S. Dahl, K. S. Thygesen and K. W. Jacobsen, *Energy Environ. Sci.*, 2012, **5**, 5814.

Included papers

Energy & Environmental Science

Cite this: *Energy Environ. Sci.*, 2011, **4**, 2937

www.rsc.org/ees

PAPER

Gas phase photocatalytic water splitting with $Rh_{2-y}Cr_yO_3$/GaN:ZnO in μ-reactors†

Fabio Dionigi,[a] Peter C. K. Vesborg,[a] Thomas Pedersen,[b] Ole Hansen,[ab] Søren Dahl,[a] Anke Xiong,[c] Kazuhiko Maeda,‡[c] Kazunari Domen[c] and Ib Chorkendorff*[a]

Received 28th February 2011, Accepted 26th April 2011
DOI: 10.1039/c1ee01242h

$Rh_{2-y}Cr_yO_3$/GaN:ZnO has been tested for gas phase overall photocatalytic water splitting by dosing water vapor. The sample has been deposited in a μ-reactor and evolves hydrogen and oxygen under illumination of solar light. This experiment proves the possibility to study solar active materials and the mechanism of the water splitting reaction with gas phase experiments. The high impact of the relative humidity on the activity has been shown by changing the water partial pressure and the reactor temperature.

1. Introduction

Water splitting under visible light is considered one of the most challenging and interesting reactions for storing solar energy as chemical energy. The production of hydrogen by photocatalytic water splitting occurs without CO_2 emission and the sun provides us with roughly 10 000 times the energy that humanity spends on an annual basis.[1] For these reasons the reaction is a clean and renewable way to obtain hydrogen fuel.

Many semiconductor materials have been developed since Fujishima–Honda demonstrated the occurrence of the reaction in 1972.[2] However, almost all these materials work only with UV light and either in the presence of a sacrificial reagent or with an applied external bias when using photoelectrodes.[3] During the past decades researchers have tried to develop materials which can absorb visible light ($\lambda > 420$ nm) and split (pure) water into oxygen and hydrogen. However, to our knowledge, only very few successes have been reported in the literature, due to the strict requirements necessary for the design of a potentially efficient and stable semiconductor material.[4,5] Indeed the band gap must be substantially smaller than 3 eV, but at the same time the potential of the conduction band edge must be negative enough to reduce protons to hydrogen and the potential of the valence band edge positive enough to oxidize water to oxygen. Currently, the most active material for water splitting (with visible light) is a GaN:ZnO solid solution with a band gap of 2.68 eV when loaded with appropriate co-catalysts (the quantum efficiency being reported to be 5.1% at $\lambda = 410$ nm).[6] This material also exhibits good stability and reproducibility.[7] The solid solution has been reported to work with RuO_2, $Rh_{2-y}Cr_yO_3$ and Rh/Cr_2O_3 core–shell co-catalysts, and among these ones the most active is $Rh_{2-y}Cr_yO_3$.[8]

So far all the activity measurements reported for this material were carried out in an aqueous solution. This is understandable since the design of a future device working with liquid water and

[a]*CINF, Department of Physics, Technical University of Denmark, DTU, Building 312, Fysikvej, DK-2800 Kgs. Lyngby, Denmark. E-mail: ibchork@fysik.dtu.dk*
[b]*Department of Micro- and Nanotechnology, Nanotech, Technical University of Denmark, DTU, Building 345 East, DK-2800 Kgs. Lyngby, Denmark*
[c]*Department of Chemical System Engineering, The University of Tokyo, 7-3-1 Hongo, Bunkyo-ku, Tokyo, 113-8656, Japan*
† Electronic supplementary information (ESI) available. See DOI: 10.1039/c1ee01242h
‡ Precursory Research for Embryonic Science and Technology (PRESTO), Japan Science and Technology Agency (JST), 4-1-8 Honcho Kawaguchi, Saitama 332-0012, Japan.

Broader context

Solar hydrogen production from water is a promising reaction to store the energy from the sun in a clean and renewable way. Semiconductor particulate photocatalysts loaded with cocatalysts have been shown to work for this reaction in an aqueous media with UV and visible light. However, in the present situation, their solar efficiency is too low to make them a viable commercial option in the energy market. Therefore fundamental studies are necessary to find which factors can enhance this efficiency. In this work we show that $Rh_{2-y}Cr_yO_3$/GaN:ZnO is able to perform photocatalytic gas phase water splitting with solar light and we show how the activity is strongly dependent on the relative humidity. This material has been tested in liquid phase water splitting, but this is the first time that it is reported to work for water splitting employing only gas phase water. The use of a μ-reactor, *i.e.* a reactor with channel dimensions in the micrometre range, is shown to be a practical way to make mechanistic studies.

colloidal suspension of the particles has already been considered.[9] It is, however, also interesting to understand the behavior when water vapor is used instead of liquid water. It may be considered to utilize the relatively high partial pressure of water which is always present in the air, even in the deserts despite otherwise dry conditions and lack of liquid water. During the summer time, for example, the deserts of south-western USA, have a dew point of 5–10 °C (278–283 K) corresponding to a partial water pressure of 10–12 mbar, which is relatively constant. This is, as we shall see a substantial amount. However, the *relative* humidity changes substantially during the day as it in a dry environment decreases strongly with increasing temperature.[10] Gas phase reactions furthermore have the advantage that bubble formation, which leads to light reflection, is avoided.

Mechanistic information such as the reaction order for the reactant (water) and the rate of the backreaction may be easier to obtain by carrying out the reaction in the gas phase. Indeed, photocatalytic decomposition of water vapor has previously been performed with metal oxide photocatalysts, *e.g.* Ni loaded $SrTiO_3$,[11] but never with oxynitrides or with visible light.

In this work we demonstrate for the first time that overall photocatalytic water splitting in gas phase works in visible light using the state of the art photocatalyst (GaN:ZnO powder loaded with $Rh_{2-y}Cr_yO_3$ co-catalyst). The μ-reactor platform used here allows for activity tests with fast response and for studying the dependence of the water partial pressure.

2. Experimental

2.1 Preparation of catalysts

$(Ga_{1-x}Zn_x)(N_{1-x}O_x)$ solid solution ($x \approx 0.19$) was prepared by heating a mixture of β-Ga_2O_3 (0.73 g) and ZnO (1.27 g) powders under NH_3 flow (250 mL min^{-1}) at 1123 K for 10 h according to the method described previously.[12,13] The band gap energy of the as-obtained $(Ga_{1-x}Zn_x)(N_{1-x}O_x)$ is *ca.* 2.65 eV, as estimated from the onset of the diffuse reflectance spectrum. The specific surface area determined by nitrogen adsorption at 77 K was *ca.* 8–9 m^2 g^{-1}. The as-synthesized $(Ga_{1-x}Zn_x)(N_{1-x}O_x)$ powder was then subjected to post-calcination in a static air atmosphere at 873 K for 1 h.[14] In this manuscript, the as-prepared $(Ga_{1-x}Zn_x)(N_{1-x}O_x)$ is referred to as GaN:ZnO for simplicity.

2.2 Modification with nanoparticulate cocatalysts

Nanoparticulate Rh–Cr mixed-oxide ($Rh_{2-y}Cr_yO_3$), a cocatalyst assisting H_2 evolution, was loaded onto the as-prepared $(Ga_{1-x}Zn_x)(N_{1-x}O_x)$ catalyst according to the method described previously.[4,15] Briefly, 0.1 g of $(Ga_{1-x}Zn_x)(N_{1-x}O_x)$ powder and 3–4 mL of distilled water containing an appropriate amount of $Na_3RhCl_6 \cdot nH_2O$ (Rh 17.8 wt%) and $Cr(NO_3)_3 \cdot 9H_2O$ were placed in an evaporating dish over a water bath. The suspension was stirred using a glass rod to complete evaporation. The resulting powder was collected and heated in air at 623 K for 1 h to convert Rh and Cr species to $Rh_{2-y}Cr_yO_3$.[15]

2.3 Gas phase photocatalytic reactions in μ-reactor

Photocatalytic reactions were carried out in a μ-reactor. This device is a flow reactor. It is described in previous publications[16,17] and has proven useful for characterization of photocatalysts.[18] In short; the μ-reactor consists in a 350 μm thick silicon chip with an area of 16 by 20 mm^2. Channels that allow the gas to flow are etched in the silicon as well as a circular (diameter = 10 mm) 3 μm deep reaction chamber (240 nl total volume). The catalyst is dispersed, sonicated in water solution and dropped in the chamber using a circular mask of 8 mm in diameter and allowed to dry. The maximum amount of $Rh_{2-y}Cr_yO_3$/GaN:ZnO that can be deposited in the reactor chamber is estimated to be ~200 μg, since the packaging density of the catalyst is measured to be ~836 g l^{-1}. However, for practical reasons, only 20 ± 10 μg of catalyst were deposited. After catalyst deposition the wafer is bonded to a Pyrex lid. The Pyrex lid is basically transparent at wavelengths $\lambda > 300$ nm. The chip presents two inlets and two outlets. One of the outlets is connected to a quadrupole mass spectrometer (QMS) by a flow limiting capillary (the magnitude of the flow conductance is $\sim 5 \times 10^{15}$ molecules s^{-1} at 1 bar). The two inlet channels mix on the chip into a main channel. The major part of the flow of the main channel goes through the second outlet where a pressure controller sets the pressure (1 bar in the experiments presented here) while the other part goes into the reaction chamber. The water vapor is obtained by bubbling helium carrier gas through pure, liquid water. This water-saturated helium flows in the first inlet channel while pure, dry helium flows in the second inlet channel. Each flow is regulated by conventional flow controllers and the humidity adjusted *via* control of the ratio of dry to water saturated helium. The temperature of the μ-reactor is monitored by a thermocouple and controlled by a heating band and a thermo-electric (Peltier) cooling element. Thermo-grease is used to assure good heat conductivity to the back-side of the reactor. The calibration procedure to convert the raw ion currents measured by the QMS to units of molecules s^{-1} is described in a previous publication.[19] In this work we used the following light sources: a high-power UV LED (Hamamatsu model LC-L2) assembled with a focusing lens (Hamamatsu L10561-220), able to produce an average irradiance on the sample area of ~460 mW cm^{-2}, as measured using a photodiode (Thorlabs model S120VC). The irradiance can be tuned electronically down to 10% of the full value and neutral density ND1.0 filter was used when a further reduction was needed. The peak wavelength is $\lambda \approx 367$ nm and the FWHM is ~9 nm. The second light source used is a 1 kW Xe-arc source (Newport model 66 924) equipped with a water filter to eliminate unwanted long-wave light and an ND0.5 filter plus an AM1.5 filter to simulate the solar spectrum in the wavelength range of interest. The third light source is an array of 4 blue/violet laser diodes (Sharp GH04P21A2GE) with wavelength $\lambda = 406$ nm and FWHM of ~1 nm.

2.4 Liquid phase photocatalytic reactions

The apparent quantum yield (AQY) for liquid-phase water splitting was measured using the same experimental setup described previously,[4,15] except for the addition of a band pass filter ($\lambda = 350 \pm 10$ nm), and was estimated as:

$$\text{AQY}\ (\%) = (A \times R/I) \times 100 \quad (1)$$

where A, R, and I represent coefficients based on the reactions (H_2 evolution, 2; O_2 evolution, 4), the H_2 or O_2 evolution rate, and the rate of incident photons, respectively. The rate of incident

photons (*ca.* 2.68×10^{19} photons h^{-1}) was measured using a calibrated silicon photodiode. The evolved gases were analyzed by gas-chromatography with an Ar carrier and a TCD detector.

3. Results

3.1 Solar driven gas phase water splitting

The sample clearly evolves hydrogen and oxygen when illuminated with the Xe-arc lamp that has been filtered in order to simulate the solar spectral irradiance. A set of three light on–light off cycles is shown in Fig. 1. The light is on for two minutes and off for other two minutes for each cycle. The lamp irradiance is close to the global total spectral irradiance of the sun facing a 37° tilted surface for an absolute air mass of 1.5 as defined by American Society for Testing and Materials (ASTM-G173) for wavelengths $\lambda < 480$ nm (Fig. S1†). The integrated irradiance from 300 nm to 462 nm (= 2.68 eV) is equal to 126 W m^{-2} for the solar spectrum and 132 W m^{-2} for our lamp. The wavelengths considered are the ones involved in the photocatalytic reaction, since the band gap is roughly estimated to be ~2.6 to 2.8 eV (corresponding to $\lambda \approx 477$–443 nm) from the absorption onset in diffuse reflectance measurements.[8] The temperature is fixed at 22 °C (295 K) and the water partial pressure is 21 mbar. The decrease in water signal is barely visible in this case of moderate light intensity. The drop is much more evident when UV light is used due to the higher intensity of the UV LED (Fig. 2). The correlation of the water consumption and the production of hydrogen and oxygen presented here can hardly be obtained with a conventional liquid batch reactor, unless very lengthy experiments are performed, making them essentially unpractical. To investigate if the material is active with visible light we also performed an experiment with a blue/violet light source with wavelength of 406 nm. The measurements confirm the results reported in literature showing that the material evolves both hydrogen and oxygen when illuminated with only visible light (Fig. S2†).

3.2 Water partial pressure dependence

In Fig. 3 the hydrogen and oxygen QMS signals are converted into the corresponding rates using the scheme discussed by Vesborg *et al.*[19] and the evolution rates are plotted as a function of the water partial pressure. The different values of water pressure, p_{H_2O}, are obtained by mixing a flow of helium which is saturated with water vapor at the bubbler temperature of 20.3 °C (293.5 K) (p_{H_2O} = 23 mbar) in the first input channel with a flow of dry helium in the second input channel. The temperature of the μ-reactor is kept constant at 25 °C (298 K). The dependence is linear for both hydrogen and oxygen in the range of water partial pressure measured and it is notable that a finite activity can be detected even at the water pressure of $p_{H_2O} \approx 2$ mbar.

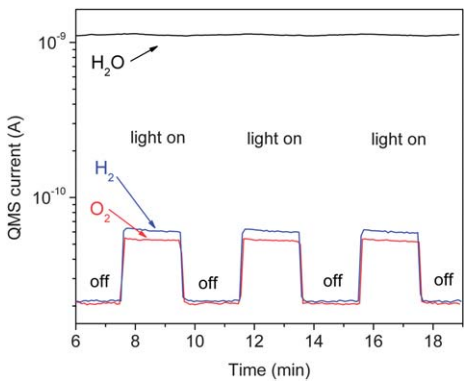

Fig. 1 QMS current for hydrogen molecules ($m/z = 2$), oxygen molecules ($m/z = 32$) and water molecules ($m/z = 18$) as a function of time. Three cycles are shown in which the light was on for 2 minutes and then off for 2 minutes. The temperature was fixed at 22 °C (295 K) and the water partial pressure was 21 mbar. The lamp used simulates the solar spectral irradiance for AM 1.5 for $\lambda < 462$ nm. H_2 and O_2 evolve when light is on.

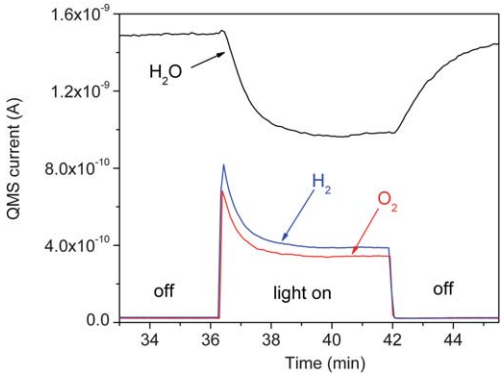

Fig. 2 QMS current for hydrogen molecules ($m/z = 2$), oxygen molecules ($m/z = 32$) and water molecules ($m/z = 18$) as a function of time ([$T = 25$ °C (298 K)], UV LED, $\lambda \approx 367$ nm, ~460 mW cm^{-2}, ~6 minutes light on).

3.3 Temperature dependence

Fig. 4 shows the activity for water splitting as a function of the temperature in the range from 25 °C to 55 °C (298 to 328 K), where the measurements are done increasing the temperature in steps of 5 °C (5 K) and stabilizing it with a Peltier element. Since the condensation of water on the catalyst creates a more complex system than a conventional gas phase reaction and our reactor is designed for gas phase experiments, we limit our study to temperatures of the μ-reactor where bulk condensation of water does not occur. The evolution rate of both hydrogen and oxygen

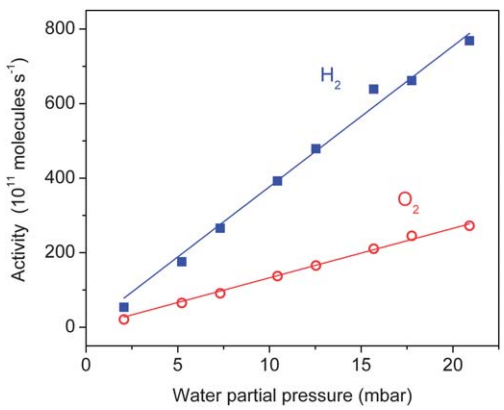

Fig. 3 Initial H_2 and O_2 evolution rate for gas-phase water splitting as a function of the water partial pressure. Temperature of 25 °C (298 K), UV LED at $\lambda \approx 367$ nm (~460 mW cm^{-2}).

decrease with increasing temperature when the sample is illuminated with nearly monochromatic UV light at $\lambda \approx 367$ nm and a light intensity of 230 mW cm^{-2}. The water partial pressure is 21 mbar. This figure shows why it is very important to keep the temperature constant in the previously presented experiments.

3.4 Light intensity dependence

A fraction of the incident photons are absorbed by the catalyst and excite electrons from the valence to the conduction band creating electron–hole pairs responsible of the catalytic reaction. The high power available from the UV LED makes it possible to measure activity as a function of light intensity over a wide range. To study this, the power of the UV LED was adjusted electronically between 100% and 10% and by inserting an ND1.0 filter between the LED and the μ-reactor the 10% to 1% interval was probed. In this way activity data were recorded over two decades, from 100% to 1% of the full power of the UV LED, with cycles of 5 minutes with light on and 5 minutes with light off. The gas evolution undergoes a slow variation during the 5 minutes, as shown in Fig. 2. Fig. 5 shows the hydrogen evolution rate (Fig. 5a), the oxygen evolution rate (Fig. 5b) and the water conversion in percent (Fig. 5c). The circle is used for the value at the end of the 5 min long illumination period, when the signal is stable, while the triangle is used for the value measured right at the beginning of the illumination period, when a distinct peak is observed both in the oxygen and in the hydrogen signal. This peak decays to the stable value within a time of ~30 s. In part, this decay is caused by the output intensity of the lamp which decreases as a function of time due to self-heating of the LED. We measured this decrease to be ~15% at full power under worst case conditions. In Fig. 5, the x-value of the steady state points have been re-scaled taking into account the decrease in the power of the LED as a function of time. This correction, in fact, is the reason why the steady state points in Fig. 5 are not plotted at exactly the same power values as the peak points. Even with this correction, however, there remains a difference between the peak values and the stable values. The peak values of both hydrogen and oxygen show a linear behavior as a function of light intensity, while the stable value tends to level off at high intensity. It is notable that a high conversion of water (up to ~43%) was achieved when illuminating at the maximum irradiance (460 mW cm^{-2}) as shown in Fig. 5c.

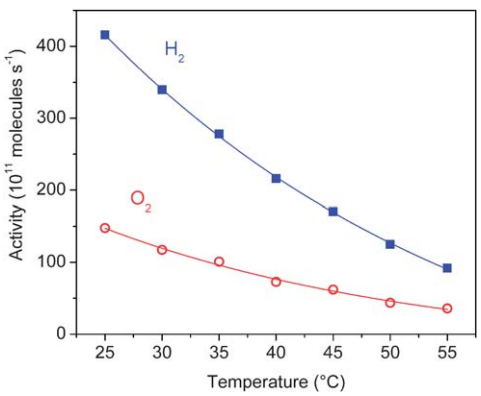

Fig. 4 Initial H_2 and O_2 evolution rates for gas phase water splitting as a function of temperature (298–328 K). The temperatures were measured with a thermocouple and kept constant with a Peltier element (UV LED, $\lambda \approx 367$ nm, ~230 mW cm^{-2}, 21 mbar).

4. Discussion

Fig. 3 shows that the rates of hydrogen and oxygen evolution are proportional to the water partial pressure, $r \propto p_{H_2O}$ when the μ-reactor is at the temperature of 25 °C and in the range of water partial pressure between 2 and 23 mbar. A plausible reason for this behavior would be that the change in water partial pressure affects the coverage of water molecules on the surface of the photocatalyst, which directly affects the reaction rate. A linear relationship between the amount of molecule adsorbed and the relative humidity, $p_{H_2O}/p^{eq}{}_{H_2O}$, is predicted in the BET adsorption model in the intermediate relative humidity range, where the coverage of the surface is more than one monolayer. This range is the central part of the s-shaped isotherm between a concave part at low pressure and a convex one at higher pressure respect to the pressure axis.[20,21]

To test this hypothesis further, in Fig. 6 the hydrogen and oxygen evolution rates are plotted as a function of the relative humidity which is determined by dividing the water pressure, p_{H_2O}, by the equilibrium vapor pressure of water, $p^{eq}{}_{H_2O}$, at the temperature of the μ-reactor. Three sets of data are shown in the figure corresponding to three different experiments where the

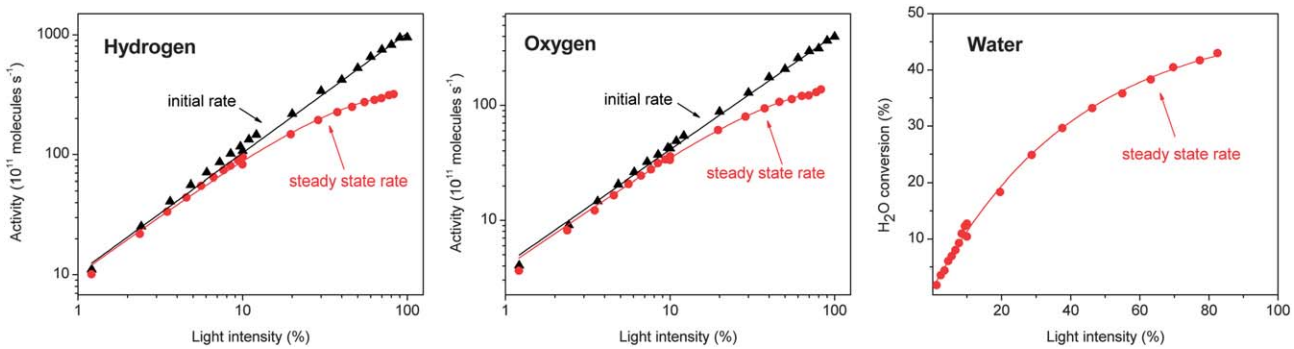

Fig. 5 Rate of hydrogen (a) and oxygen (b) evolution for gas phase water splitting as a function of light intensity (UV, $\lambda \approx 367$ nm) [$T = 22$ °C (295 K)]. The initial rate (triangles) and the rate achieved after 5 minutes of illumination (circles) are plotted for both the products. The corresponding water conversion percentage is plotted (c). 100% of light intensity corresponds to an irradiance of ~460 mW cm^{-2}.

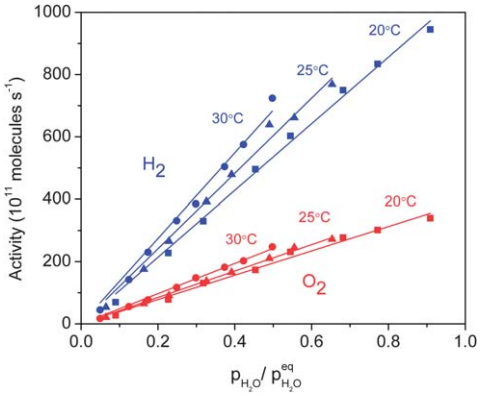

Fig. 6 Initial H_2 and O_2 evolution rate for gas-phase water splitting partial pressure divided by the water equilibrium vapor pressure. Three sets of data point are plotted corresponding to experiments made at the temperature of 20 °C (293 K) (squares, $p^{eq}{}_{H_2O} = 23$ mbar), 25 °C (298 K) (triangles, $p^{eq}{}_{H_2O} = 32$ mbar) and 30 °C (303 K) (circles, $p^{eq}{}_{H_2O} = 42$ mbar). (UV LED, $\lambda \approx 367$ nm, ~460 mW cm^{-2}.)

temperature of the μ-reactor is 20 °C, 25 °C and 30 °C (293, 298 and 303 K). The corresponding $p^{eq}{}_{H_2O}(T)$ are 23 mbar, 32 mbar and 42 mbar, respectively. The three sets of data, corresponding to different temperatures, lie very close to the same line when plotted *versus* the relative humidity. This result can be expressed in the formula for the reaction rate r:

$$r(t) \propto \frac{p_{H_2O}(t)}{p^{eq}_{H_2O}(T)} \quad (2)$$

where for the reaction rate r and the water partial pressure p_{H_2O} the time dependence t has been explicitly indicated. The equation does not hold for values of the relative humidity close to unity, since close to the dew point condensation of water in small pores starts to occur.

In order to find out if the fact that $p^{eq}{}_{H_2O}$ increases with the temperature is describing the temperature dependence observed in Fig. 4 the normalized reaction rate $r \times (p^{eq}{}_{H_2O}/p_{H_2O})$ is calculated for all the data points and it turns out that the temperature dependence of the proportionality factor in eqn (2) is weak (Fig. S3†). In summary, the temperature behavior of the rate under the conditions of our experiments can be explained with eqn (2) showing that the important parameter is not the absolute water pressure but the relative humidity. This is naturally unfortunate for a catalyst operating in a desert environment.

The temperature dependence of the rate of H_2 and O_2 in liquid phase has been reported by Hisatomi *et al.* in the range of temperature between 2 °C (275 K) and 48 °C (321 K).[22] They found an increase in the activity with increasing temperature and calculated an apparent activation energy of 7.6 ± 2.4 kJ mol^{-1}. If we consider the normalized rate $r \times (p^{eq}{}_{H_2O}/p_{H_2O})$ in the temperature range between 25 °C and 45 °C, that is included in the one studied by Hisatomi *et al.*, we noticed that we also have a weak increase in the activity as a function of temperature (Fig. S3†). This tendency is also observed for the stable values after 5 min of irradiation. Constructing an Arrhenius plot from the data in Fig. S3†, we find an apparent activation energy of 8.0 ± 1.4 kJ mol^{-1} in the temperature interval 25 °C to 45 °C (close to the result of Hisatomi *et al.*), but clearly the temperature dependence deviates from Arrhenius behavior above about 40 °C, so this value is just a rough estimate valid only for lower temperatures. In particular, at higher temperatures (50 °C and 55 °C) the activity decreases slowly as the temperature is raised. This could be due to an increasing electron–hole recombination rate at the surface of the photocatalyst when the temperature is increased.

The difference in behavior between the initial rate values and the stabilized ones after 5 minutes in Fig. 5a and b can also be explained considering the equilibrium coverage of H_2O on the active sites. As the reaction proceeds, we move from the limit of zero conversion of water, where the water coverage is Θ, to an equilibrium water coverage $\Theta' < \Theta$ determined by the rate of conversion of water (due to the drop in local water partial pressure). This equilibrium water coverage decreases at high light intensity where the reaction significantly lowers the water partial pressure in the reactor as shown in Fig. 5c. In this way the phenomenon can also be explained by eqn (2) and an attempt to correct the decay of the signals of H_2 and O_2 is shown in Fig. S4†. The signals have been multiplied by the ratio of the currents H_2O^{dark}/H_2O^{light} and further by the ratio of light intensity $\Phi(t = 0)/\Phi(t)$, with t the time during which the light is on. The behavior of the peak values shows that the dependence of the activity *versus* the light intensity is linear until this high power intensity. We can combine this result with eqn (2) and write:

$$r(t) = k(\lambda, T)\Phi(t)\frac{p_{H_2O}(t)}{p^{eq}_{H_2O}(T)} \quad (3)$$

Where r is the reaction rate, $k(\lambda,T)$ is a constant dependent on wavelength (and possibly also temperature) and $\Phi(t)$ is the light irradiance. The linear relationship between the gas evolution rate and the light intensity has been observed in liquid phase for the same catalyst for low intensity up to 1×10^{22} photons h^{-1}.[22] Hisatomi *et al.* calculated the number of particles used in their experiment to be roughly 1.2×10^{13} that leads to 10^5–10^6 photons s^{-1} $particle^{-1}$. Our result is in good agreement with the one reported since our maximum intensity is 4.4×10^{20} photons h^{-1}, the maximum number of particles calculated using the same procedure of Hisatomi *et al.* is 2.3×10^{10} and so the rate of photon absorption per particle is roughly 10^6 photons s^{-1} $particle^{-1}$.

The ratio between hydrogen and oxygen is almost stoichiometric in the liquid phase experiments while it is higher than 2 and equal to ~2.5 in the gas phase. This deviation can arise if there is something which could be oxidized in the μ-reactor *i.e.* the holes oxidize the nitrogen in the catalyst to N_2 or if extra hydrogen is produced by reforming of hydrocarbons. Indeed this catalyst is able to steam reform hydrocarbon such as ethanol and at the first test of the sample CO_2 ($m/z = 44$) and CH_4 ($m/z = 15$) are evolved under illumination. However, these signals disappear relatively fast so that only negligible traces of CO_2, N_2, CH_4 and CO are observed which presently cannot explain the discrepancy. Similarly, considerable efforts have been dedicated to find the source of the discrepancy and the possibility of H_2O_2 production has also been investigated. Although a small amount of mass 34 was found, this could be explained by the natural abundance of ^{18}O. The catalyst was also exposed to light for extended time and no degradation indicating that oxidation of the catalyst took place was found.

The quantum efficiency, defined as the number of electrons that contribute to the reaction divided by the number of photons

absorbed, has been calculated at $\lambda = 367$ nm, $p_{H_2O} = 21$ mbar and $T = 25\ ^\circ C$ (298 K). The H_2 evolution rate, multiplied by 2 to take into account that 2 electrons are necessary to make one hydrogen molecule, has been divided by the absorbed photon flux. The fraction of absorbed photons is estimated to be 29% of the incident ones from transmission and diffuse reflectance measurements on the same catalyst deposited on a Pyrex lid before bonding. The value obtained for the quantum efficiency is 0.16%. This value is lower than the one obtained in liquid phase using the same catalyst under 350 ± 10 nm irradiation: 5.5 ± 0.2%.

There are several significant differences in between the two experiments such as: (1) the phase of water. In particular the quantum efficiency is a function of p_{H_2O} and follows the trend in Fig. 3 since in that measurement the H_2 rate changes without changing the light intensity. (2) The catalyst is suspended in liquid water in one case while in the other one it is deposited on the lid and covered with a monolayer or more of water in relation to the relative humidity. (3) The rate is dependent on pH in liquid phase but in gas phase the pH is not defined.[23]

All these macroscopic observations can find a microscopic explanation if the phenomenon that limits the quantum efficiency in the gas phase is the surface conduction of protons, H^+, to the H_2 molecules evolution sites. It is known that the H_2 molecules evolution site of our catalyst is the $Rh_{2-y}Cr_yO_3$ co-catalyst, while H^+ is formed at the surface of the GaNZnO from an adsorbed H_2O* molecule or other intermediates (OH^{-*}, OOH*, …).[23] The conduction of the H^+ from the GaNZnO surface to the co-catalyst is easier in an acid pH solution, since this provides a reservoir of H^+. Increasing the relative humidity in the gas phase is beneficial, since the creation of a more connected film of water covering the nanoparticles increases the mobility of the H^+. The observed small activation energy is in good agreement with the activation energy observed for proton mobility in water.[24] (Please note that when extracting the apparent activation energy the effect of relative humidity has been taken out and the value is valid for a continuous water film.) However, as mentioned earlier great care should be exercised here since this is an apparent activation energy which may also contain contribution from many effects such as the transport and annihilation of electron–hole pairs, the detailed reaction mechanism of splitting water, and the oxygen and hydrogen evolution processes. We have also investigated the isotope effect and the reaction is clearly in favor of splitting H_2O compared to D_2O. The reported linear dependence of the relative humidity here merely reflects the amount of catalyst that is available for the water splitting process due to connecting water films.

5. Conclusion

GaN:ZnO powder loaded with $Rh_{2-y}Cr_yO_3$ co-catalyst is able to decompose water vapor and evolve hydrogen and oxygen when illuminated with (simulated) solar light. The dependence of the rate of water splitting *versus* the irradiance at 367 nm is linear from a moderate intensity (~4.6 mW cm^{-2}) to a high intensity (~460 mW cm^{-2}). At this maximum irradiance the conversion of water was ~43%. It is found that the activity is proportional to the relative humidity of the gas. This dependence explains why the activity *versus* the water vapor partial pressure is found to be linear (first order kinetics in water partial pressure). Furthermore it explains why the activity measured at 367 nm decreases significantly as temperature is increased. The quantum efficiency measured is 0.16% at $\lambda = 367$ nm, $p_{H_2O} = 21$ mbar and $T = 25\ ^\circ C$ (298 K). It is proposed that the strong dependence of humidity is due to limited proton conductivity in the thin water layers from the reaction centers oxidizing water to the hydrogen evolution centers ($Rh_{2-y}Cr_yO_3$).

Acknowledgements

Center for Individual nanoparticle Functionality (CINF) is financed by the Danish National research Foundation. This was also financed by the Research and Development in a New Interdisciplinary Field Based on Nanotechnology and Materials Science program of the Ministry of Education, Culture, Sports, Science and Technology (MEXT) of Japan, and The KAITEKI Institute, Inc. This project was furthermore funded by "Catalysis for Sustainable Energy" (CASE) research initiative, which is funded by the Danish Ministry of Science, Technology and Innovation.

References

1 M. Gratzel, *Nature*, 2001, **414**, 338.
2 A. Fujishima and K. Honda, *Nature*, 1972, **238**, 37.
3 A. Kudo and Y. Miseki, *Chem. Soc. Rev.*, 2009, **38**, 253.
4 K. Maeda, K. Teramura, D. Lu, T. Takata, N. Saito, Y. Inoue and K. Domen, *Nature*, 2006, **440**, 295.
5 Y. Lee, H. Terashima, Y. Shimodaira, K. Teramura, M. Hara, H. Kobayashi, K. Domen and M. Yashima, *J. Phys. Chem. C*, 2007, **111**, 1042.
6 K. Maeda and K. Domen, *J. Phys. Chem. Lett.*, 2010, **1**, 2655.
7 K. Maeda and K. Domen, *Chem. Mater.*, 2010, **22**, 612.
8 K. Maeda, K. Teramura, N. Saito, Y. Inoue, H. Kobayashi and K. Domen, *Pure Appl. Chem.*, 2006, **78**, 2267.
9 http://www1.eere.energy.gov/hydrogenandfuelcells/pdfs/pec_technoeconomic_analysis.pdf.
10 C. D. Ahrens, *Essential of Meteorology: an introduction to the Atmosphere*, Thomson Learning Inc., 5th edn, 2008, ISB: 10 0-945-11558-4.
11 K. Domen, S. Nalto, T. Onlshl, K. Tamaru and M. Soma, *J. Phys. Chem.*, 1982, **86**, 3657.
12 K. Maeda, T. Takata, M. Hara, N. Saito, Y. Inoue, H. Kobayashi and K. Domen, *J. Am. Chem. Soc.*, 2005, **127**, 8286.
13 K. Maeda, K. Teramura, T. Takata, M. Hara, N. Saito, K. Toda, Y. Inoue, H. Kobayashi and K. Domen, *J. Phys. Chem. B*, 2005, **109**, 20504.
14 K. Maeda, K. Teramura and K. Domen, *J. Catal.*, 2008, **254**, 198.
15 K. Maeda, K. Teramura, D. Lu, T. Takata, N. Saito, Y. Inoue and K. Domen, *J. Phys. Chem. B*, 2006, **110**, 13753.
16 T. R. Henriksen, J. L. Olsen, P. C. K. Vesborg, I. Chorkendorff and O. Hansen, *Rev. Sci. Instrum.*, 2009, **80**, 124101.
17 P. C. K. Vesborg, J. L. Olsen, T. R. Henriksen, I. Chorkendorff and O. Hansen, *Rev. Sci. Instrum.*, 2010, **81**, 016111.
18 P. C. K. Vesborg, J. L. Olsen, T. R. Henriksen, I. Chorkendorff and O. Hansen, *Chem. Eng. J.*, 2010, **160**, 738.
19 P. C. K. Vesborg, S.-I. In, J. L. Olsen, T. R. Henriksen, B. L. Abrams, Y. Hou, A. Kleiman-Shwarsctein, O. Hansen and I. Chorkendorff, *J. Phys. Chem. C*, 2010, **114**, 11162.
20 I. Chorkendorff and H. Niemantsverdriet, *Concepts of Modern Catalysis and Kinetics*, Wiley-VCH, Weinheim, 2007, 456 pages, ISBN 3-527-31672-4.
21 S. Brunauer, P. H. Emmett and E. Teller, *J. Am. Chem. Soc.*, 1938, **60**, 309.
22 T. Hisatomi, K. Maeda, K. Takanabe, J. Kubota and K. Domen, *J. Phys. Chem. C*, 2009, **113**, 21458.
23 K. Maeda, K. Teramura, H. Masuda, T. Takata, N. Saito, Y. Inoue and K. Domen, *J. Phys. Chem. B*, 2006, **110**, 13107.
24 N. Agmon, *Chem. Phys. Lett.*, 1995, **244**, 456.

Journal of Catalysis 292 (2012) 26–31

Contents lists available at SciVerse ScienceDirect

Journal of Catalysis

journal homepage: www.elsevier.com/locate/jcat

Suppression of the water splitting back reaction on GaN:ZnO photocatalysts loaded with core/shell cocatalysts, investigated using a μ-reactor

Fabio Dionigi [a], Peter C.K. Vesborg [a], Thomas Pedersen [b], Ole Hansen [a,b], Søren Dahl [a], Anke Xiong [c], Kazuhiko Maeda [c,d], Kazunari Domen [c], Ib Chorkendorff [a,*]

[a] CINF, Department of Physics, Building 312, Fysikvej, Technical University of Denmark, DTU, DK-2800 Kgs. Lyngby, Denmark
[b] Department of Micro- and Nanotechnology, Nanotech, Building 345 East, Technical University of Denmark, DTU, DK-2800 Kgs. Lyngby, Denmark
[c] Department of Chemical System Engineering, The University of Tokyo, 7-3-1 Hongo, Bunkyo-ku, Tokyo 113-8656, Japan
[d] Precursory Research for Embryonic Science and Technology (PRESTO), Japan Science and Technology Agency (JST), 4-1-8 Honcho Kawaguchi, Saitama 332-0012, Japan

ARTICLE INFO

Article history:
Received 31 January 2012
Revised 8 March 2012
Accepted 23 March 2012
Available online 3 May 2012

Keywords:
Photocatalysis
Hydrogen
Core/shell
Water splitting
GaN:ZnO
Hydrogen oxidation

ABSTRACT

Using silicon-based μ-reactors, we have studied the photocatalytic water splitting reaction and the catalytic back reaction on the same catalysts. GaN:ZnO without cocatalyst and loaded with Rh, Pt, Cr_2O_3/Rh, Cr_2O_3/Pt, and Rh–Cr mixed oxide has been tested for gas-phase photocatalytic water splitting. The results confirm the high activity observed in liquid-phase experiments with Cr_2O_3/Rh and Rh–Cr mixed oxide as cocatalysts. To investigate the reason of this enhanced activity, the back reaction was studied by reacting stoichiometric H_2/O_2 and monitoring the water molecules produced. The comparison of the two experiments shows that the suppression of the back reaction with the core/shell cocatalysts and the Rh–Cr mixed oxide corresponds to an increase in the net photocatalytic water splitting activity. The fact that the back reaction is not completely suppressed with Cr_2O_3/Pt compared to Cr_2O_3/Rh may be the cause of the higher net activity of the Cr_2O_3/Rh.

1. Introduction

Photocatalytic water decomposition into hydrogen and oxygen using solar light is a clean and renewable way to store energy from the sun as chemical energy. Several approaches have been studied in order to find a catalytic system able to perform this highly desirable reaction in an efficient way [1,2]. One of the promising systems consists of a powder catalyst made of a semiconductor photocatalyst (i.e., a metal oxide or an oxynitride) with the surface decorated by smaller cocatalyst nanoparticles. Photocatalytic water splitting using this kind of catalyst is illustrated in Fig. 1a. This system has several advantages originating basically from its simplicity: there is only one photocatalyst material, there are no wire connections, and a powder catalyst has a high surface-area-to-mass ratio. However, it also presents some technical challenges. Hydrogen and oxygen are produced in the same environment, and they can back react to form water. This is an unfortunate event because it implies a loss of products and thus a loss of energy/efficiency. In order to achieve high efficiency, this back reaction must be avoided. In this work, we show through direct experiments how the water formation reaction (water splitting back reaction) can be suppressed by cocatalyst modification. The photocatalyst that we have used for this purpose is GaN:ZnO loaded with five different cocatalysts: two noble metals, Pt and Rh, their corresponding core/shell modification (the noble metal particles covered by a Cr_2O_3 shell), and the mixed oxide $Rh_{2-y}Cr_yO_3$. They have previously been synthesized and tested in liquid phase by Maeda et al., and the same authors have shown that the chromia shell improves the activity for photocatalytic liquid-phase water splitting [3,4]. So far, the GaN:ZnO with a band gap of 2.6–2.7 eV is the photocatalyst with the highest reported activity in the visible region for overall water splitting (5.1% at $\lambda = 410$ nm when loaded with $Rh_{2-y}Cr_yO_3$) [4]. For this reason, we focus the study of the chromia core/shell cocatalyst on this photocatalyst. However, the positive effect of the chromia shell is not limited to GaN:ZnO. For example, it has been shown recently that overall water splitting can be observed when GaN nanowires are loaded with a Cr_2O_3/Rh cocatalyst, while no measurable activity has been observed when only Rh was loaded [5]. Electrochemical experiments using electrodes to model the cocatalyst nanoparticles showed that the reason for the enhanced activity when a chromia shell is used to protect the noble metals is the suppression of the water splitting back reaction [6]. In this work, the water splitting back reaction rate is analyzed directly measuring the catalytic water formation from a stoichiometric 2:1 flow of H_2 and O_2 and on the same systems used for photocatalytic water splitting (cocatalyst deposited

* Corresponding author. Fax: +45 4593 2399.
E-mail address: ibchork@fysik.dtu.dk (Ib Chorkendorff).
URL: http://dcwww.fys.dtu.dk/~ibchork/ (Ib Chorkendorff).

0021-9517/$ - see front matter © 2012 Elsevier Inc. All rights reserved.
http://dx.doi.org/10.1016/j.jcat.2012.03.021

on photocatalyst powder). This experiment is similar to hydrogen oxidation experiments that have been extensively studied in heterogeneous catalysts on model system, that is, Pt single crystals and Pt nanoparticles on oxide support [7,8]. Thanks to those experiments, a lot of information is available on surface coverage and kinetics for this reaction. Differing from these experiments, our purpose is not to study the fundamental aspects of the H_2/O_2 reaction, but to perform the H_2/O_2 reaction on photocatalysts at conditions similar to photocatalytic water splitting conditions (presence of stoichiometric H_2/O_2 mixture, room temperature, 1 bar). Finally, we compare those results with the photocatalytic activities obtained for gas-phase water splitting using the same catalysts.

2. Experimental

2.1. Preparation of the GaN:ZnO photocatalyst

$(Ga_{1-x}Zn_x)(N_{1-x}O_x)$ solid solution ($x \approx 0.12$) was prepared by heating a mixture of β-Ga_2O_3 (1.08 g) and ZnO (0.94 g) powders under NH_3 flow (200 ml min^{-1}) at 1098 K for 13.5 h according to a similar method we have reported previously [9,10]. The as-synthesized $(Ga_{1-x}Zn_x)(N_{1-x}O_x)$ powder was then subjected to post-calcination in a static air atmosphere at 873 K for 5 h [11]. The effects of preparation parameters on the physicochemical properties of GaN:ZnO have been discussed in our previous papers [10,12] and are reported briefly in the present study as supporting information. XRD analysis confirms that the as-prepared sample exhibits a single hexagonal wurtzite phase (Fig. S1). The sample has a featureless morphology (Fig. S2) with a specific surface area of 7–8 $m^2 g^{-1}$ determined by nitrogen adsorption at 77 K. As shown in Fig. S3, the band gap of the material is estimated to be ca. 2.7 eV. In this manuscript, the as-prepared $(Ga_{1-x}Zn_x)(N_{1-x}O_x)$ is referred to as GaN:ZnO for simplicity.

2.2. Deposition of cocatalyst nanoparticles

The Rh- and Pt-loaded GaN:ZnO was first prepared by a photodeposition method from Na_3RhCl_6 and H_2PtCl_6 solution, respectively, in which 1 wt.% metal was dissolved in each case. Using the as-prepared metal-loaded samples, photodeposition of K_2CrO_4 was done. Considering the self-limiting nature of Cr_2O_3 photodeposition, it is expected that ~0.3 wt.% Cr is deposited [13].

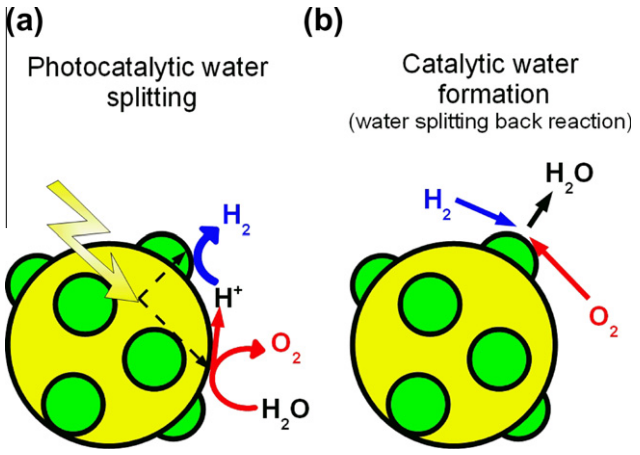

Fig. 1. Photocatalytic water splitting and catalytic formation of water on a photocatalyst (yellow) loaded with a cocatalyst (green). (For the interpretation of the references to color in this figure legend, the reader is referred to the web version of this article.)

Nanoparticulate Rh–Cr mixed oxide ($Rh_{2-y}Cr_yO_3$), a cocatalyst assisting H_2 evolution, was loaded onto the as-prepared $(Ga_{1-x}Zn_x)(N_{1-x}O_x)$ catalyst according to the method described previously [14,15]. Briefly, 0.1 g of $(Ga_{1-x}Zn_x)(N_{1-x}O_x)$ powder and 3–4 ml of distilled water containing an appropriate amount of $Na_3RhCl_6{\cdot}nH_2O$ (Rh 17.8 wt.%) and $Cr(NO_3)_3{\cdot}9H_2O$ were placed in an evaporating dish over a water bath. The suspension was stirred using a glass rod to complete the evaporation. The resulting powder was collected and heated in air at 623 K for 1 h to convert Rh and Cr species to $Rh_{2-y}Cr_yO_3$ [15]. Rh and Cr were loaded at rates of 1 and 1.5 wt.% (metallic content), respectively.

2.3. Gas-phase photocatalytic water splitting reaction and back reaction in μ-reactors

Both the photocatalytic water splitting reactions and the dark back reactions (water formation) were performed using silicon-based μ-reactor technology [16]. The μ-reactor used for this work is a flow reactor and consists in a 350-μm-thick silicon chip with an area of 16 mm by 20 mm. Channels that allow the gas to flow are etched in the silicon as well as a circular (diameter = 10 mm) 3-μm-deep reaction chamber (240 nl total volume). The catalyst is dispersed, sonicated in water solution, dropped in the chamber, and allowed to dry using a circular mask of 8 mm in diameter. The amount of material deposited is ~60 μg for each catalyst. After catalyst deposition, the wafer is bonded to a Pyrex lid by the cold bonding technique [17]. The Pyrex lid is basically transparent at wavelengths $\lambda > 300$ nm, and thus, it allows photocatalytic experiments with solar light [18]. The chip presents two inlets and two outlets. One of the outlets is connected to a quadrupole mass spectrometer (QMS) by a flow-limiting capillary (the magnitude of the flow conductance is $\sim 5 \times 10^{15}$ molecule/s at 1 bar reactor pressure) and defines the flow through the reaction chamber. The two inlet channels mix on the chip into a main channel. The major part of the flow of the main channel goes through the second outlet where a pressure controller sets the pressure (1 bar in the experiments presented here). The water vapor used in the photocatalytic experiments is obtained by bubbling helium carrier gas (AGA, scientific quality 6.0) through pure, liquid water (Millipore, 18.2 MΩ cm). This water-saturated helium flows in the first inlet channel, while pure, dry helium flows in the second inlet channel. Each flow is regulated by conventional flow controllers and the humidity adjusted via control of the ratio of dry to water-saturated helium. For the back reaction experiments, He is flowing in the first input channel, while H_2 (or O_2) is flowing in channel 2. Then, O_2 (or H_2) is introduced in channel 1. Both H_2 and O_2 are of scientific quality 6.0 (AGA). The temperature of the μ-reactor is monitored by a thermocouple and controlled by a heating band and a thermo-electric (Peltier) cooling element. Thermo-grease is used to assure good heat conductivity between the back side of the reactor and the cooling element. The calibration procedure to convert the raw ion currents measured by the QMS into molecule/s is described in a previous publication [19]. The light source used in the photocatalytic experiments is a high-power UV LED (Hamamatsu model LC-L2) assembled with a focusing lens (Hamamatsu L10561-220), able to produce an average irradiance on the sample area of ~460 mW/cm^2, as measured using a photodiode (Thorlabs model S120VC). The peak wavelength is $\lambda \sim 367$ nm, and the FWHM is ~9 nm. This light source has been used instead of visible light in order to have a better signal-to-noise ratio, even if all the cocatalyst-loaded samples were tested to be active with a 1-kW Xe-arc source with a longpass 420-nm cutoff filter. The LED was used at 20% (92 mW/cm^2) of its full power for all the photocatalytic water splitting experiments.

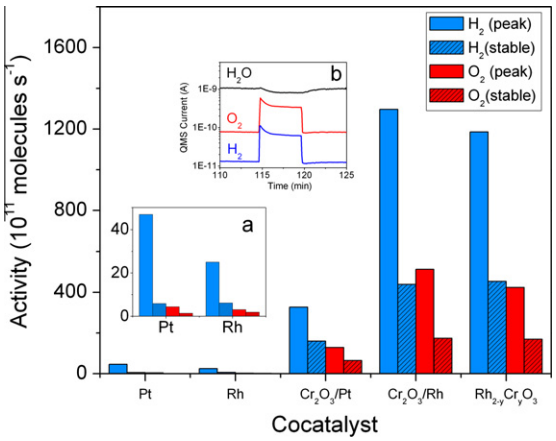

Fig. 2. Hydrogen and oxygen evolution rates for overall photocatalytic water splitting with GaN:ZnO loaded with different cocatalysts. Relative humidity 85%. UV LED at $\lambda \sim 367$ nm ($I \sim 92$ mW/cm^2). The inset a is an enlargement of the results for Pt and Rh. In the histogram, the values of the initial rate (the peak that can be seen in the time evolution of the QMS currents in inset b appearing immediately after the light is switched on) are shown with full colored columns, while the values of the stable rate obtained after 5 min of illumination are shown with hatched colored columns. (For interpretation of the references to color in this figure legend, the reader is referred to the web version of this article.)

3. Results

3.1. Photocatalytic gas-phase water splitting

GaN:ZnO with no cocatalyst and GaN:ZnO with five different cocatalysts were tested for gas-phase overall water splitting using an UV LED (~367 nm) as light source. In a previous publication, we have shown that if the relative humidity, and thus the adsorption of water on the catalyst, is increased, the activity also increases [20]. It has been proposed that the increase in adsorbed water can facilitate surface proton conduction, a necessary reaction step for the water splitting mechanism. As a consequence, relative humidity is an important parameter for gas-phase water splitting and its value has been kept constant at ~85% (constant water partial pressure ~27.3 mbar and temperature of the reactor ~25 °C, 298 K) in all the tests. No hydrogen and oxygen photocatalytic evolution could be detected with GaN:ZnO powder without a cocatalyst. All the other samples were active for gas-phase water splitting, and the comparison of their activities is shown in Fig. 2. Both the initial peak value and the stable value for both hydrogen and oxygen obtained after 5 min of irradiation are shown for every sample. The ratio between the evolved H_2 and O_2 is ~2.5 for the samples loaded with the Cr_2O_3/Rh, Cr_2O_3/Pt, and $Rh_{2-y}Cr_yO_3$ for both the initial and stable values. The noble metal–loaded samples show a stronger departure from the stoichiometric ratio for the initial activity rate, while the ratio decreases during illumination. The GaN:ZnO samples loaded with only noble metals have the lowest activity, while the samples where Cr is present have a higher activity. In particular, the Cr_2O_3 shell improves the activity of both the Pt sample and the Rh sample. Cr_2O_3/Rh has a higher activity than Cr_2O_3/Pt and comparable to $Rh_{2-y}Cr_yO_3$. Apart from $Rh_{2-y}Cr_yO_3$/GaN:ZnO, none of the materials have previously been reported in the literature to work in gas phase for photocatalytic overall water splitting. The activity of $Rh_{2-y}Cr_yO_3$/GaN:ZnO is similar to what has been reported in our previous study for the same catalyst obtained with slightly different preparation conditions [20]. The presented experiments have been repeated several times, and the reproducibility of the results with the optimized catalysts is usually within 10–15%. Possible sources of error can be attributed to small differences in the concentration of the catalysts in the solution from which the catalyst is drop-casted on the lid and errors in the estimation of the relative humidity.

3.2. Water splitting back reaction

Water formation from the catalytic reaction of H_2 and O_2 has been measured for all the samples. This experiment consists in measuring the amount of water evolved as detected by a QMS. Since this reaction evolves high amount of energy, it can be dangerous to perform in a macroscopic reactor. In our case, however, the reactor chamber is only 240 nl in volume, essentially eliminating the safety issues. We have performed the experiments at room temperature (25 °C, 298 K), diluting the H_2 (2 ml/min)/O_2 (1 ml/min) flow mixture with 15 ml/min of He and at 1 bar of total pressure. Fig. 3a and b presents typical examples of a back reaction experiment. In Fig. 3a, the raw data of an experiment with the reactor loaded with Pt/GaN:ZnO are shown. At the beginning of the experiment, only O_2 and He are flowing through the reactor. A local minimum in the O_2 occurs instantly after the H_2 flow in the He channel is started (~90 min after we have mounted the reactor into the gas manifold). At the same time, a peak in the He is measured. These features are due to the sudden increase in the flow of channel 1 (passing from 15 ml/min of He to 17 ml/min (15 of He and 2 of H_2)) and therefore not related to any catalytic activity (the same feature is observed in Fig. 3b). After the introduction of hydrogen, the water signal increases. At the same time, the oxygen is consumed, confirming the occurrence of the back reaction:

$$2H_2 + O_2 \rightarrow 2H_2O \quad (1)$$

for the Pt-loaded sample (Fig. 1b). Notice that this spontaneous reaction ($\Delta G < 0$) occurs without the need of photoexcited carriers, but it is facilitated by the catalytic properties of the surface of the Pt nanoparticles. The dominant mechanism is a Langmuir–Hinshelwood type, involving the dissociative adsorption of hydrogen and oxygen. In Fig. 3b, the experiment has been repeated for $Rh_{2-y}Cr_yO_3$/GaN:ZnO. In this case, the introduction of hydrogen does not cause any noticeable evolution of water or consumption of oxygen, meaning that the back reaction is strongly suppressed with the $Rh_{2-y}Cr_yO_3$ cocatalyst. Notice that this second experiment shows also that if reaction 1 occurs on the hot filament in the QMS, the rate is negligible and below our detection limit. Thus, there is no need to repeat the experiment with an empty reactor.

This experiment was repeated for all the other samples including the GaN:ZnO without cocatalyst. In this latter case, no back reaction activity is observed. The highest back reaction activity is observed for Pt cocatalyst. Both core/shell cocatalyst exhibited less catalytic activity for the back reaction than their respective pure noble metal. A similar back reaction experiment was also performed for all the samples by changing the order of introduction of H_2 and O_2. In this experiment, the initial flow is H_2 and O_2 is introduced later. So in this experiment, the sample is in a dry H_2 atmosphere when O_2 is injected, while in the experiments discussed before it was in a dry O_2 atmosphere when H_2 was injected. The results of the two kinds of back reaction experiments are summarized in Fig. 4 together with the photocatalytic water splitting results. For the latter, only the H_2 evolution is shown not to overload the plot with information, while for the back reactions experiment, the water formation rate measured after 30 min from the introduction of the second reactant gas (H_2 or O_2) is shown. All the raw data are available as Supplementary information. In the case when O_2 is introduced last, the water signal for the samples that have a finite back reaction rate presents an initial peak (with the maximum at ~4 min after the introduction of O_2). After that, the signal reaches a lower steady state. We noticed that neither the peak value nor the steady state is equal to the steady state of

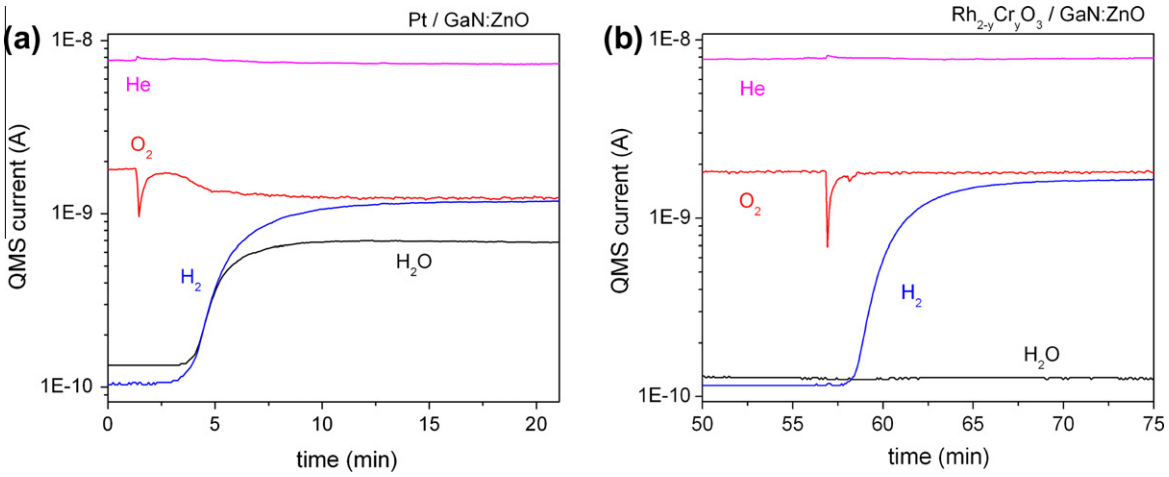

Fig. 3. QMS current for hydrogen molecules ($m/z = 2$), oxygen molecules ($m/z = 32$), water molecules ($m/z = 18$), and helium ($m/z = 4$) as a function of time for a water splitting back reaction experiment. The flow of H_2 is 2 ml/min, of O_2 1 ml/min, and of He 15 ml/min. Water is evolved in the case of Pt/GaN:ZnO. No water could be detected with $Rh_{2-y}Cr_yO_3$/GaN:ZnO.

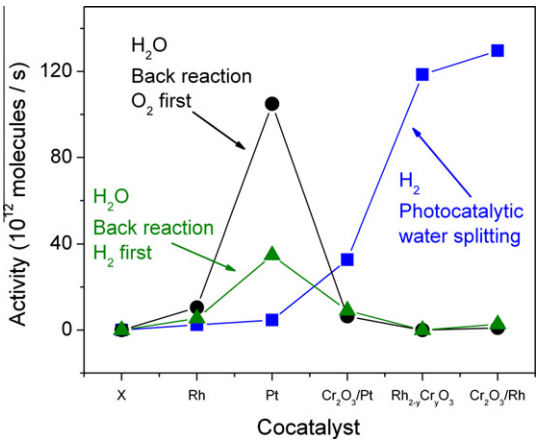

Fig. 4. Initial hydrogen evolution rate for overall photocatalytic water splitting (blue squares) and water evolution rate for the dark back reaction experiments starting with H_2 (green triangles) or O_2 (black circles) diluted in He. Notice that the 3 set of data are taken from three different kinds of experiments, as indicated in the labels. For the two back reaction experiments, H_2 and O_2 are mixed in the stoichiometric ratio. In the *x*-axis is indicated the cocatalyst loaded on the GaN:ZnO. The X indicates the bare GaN:ZnO powder without cocatalyst. (For the interpretation of the references to color in this figure legend, the reader is referred to the web version of this article.)

the other case, when O_2 is flowing as first reactant gas and H_2 is introduced later.

As previously mentioned, the reactions are carried out in the dark so the water formed in these experiments is not the result of light excitation of the catalyst. However, to study the effect of light, we have illuminated the sample with the UV LED light source used in the photocatalytic water splitting experiment with the maximum power (~460 mW/cm^2) before the second reactant gas is introduced and after at least 30 min of this introduction (Figs. S4–S15). In the case of light exposure when only one of the reactant gases was present, we have performed that experiment first of all to clean eventually small amount of dirt accumulated on the surface from the air and second to have a reference to compare the light effect in the stoichiometric mixture. No effect of light can be seen for the GaN:ZnO without cocatalysts. The same holds for all the experiments with the Rh-based catalyst. If the light has an effect with these samples, it is negligible. It is noticeable that in the case of pure GaN:ZnO and GaN:ZnO loaded with Cr_2O_3/Rh and $Rh_{2-y}Cr_yO_3$, no back reaction rate can be detected even in the presence of light. A different situation occurs with Pt and Cr_2O_3/Pt cocatalysts. With these samples, an increase in the water evolution rate can be detected under illumination when the system is exposed to the stoichiometric H_2/O_2 mixture. This effect is particularly strong with Pt when we start flowing H_2. In that case, the water signal increases to a value approximately equal to the maximum of the initial peak and a new steady state is reached. To check whether this effect is due to a cleaning of the surface of Pt, from , that is, hydrocarbons contamination, we have repeated the back reaction experiment with Pt immediately after the first experiment, without dismounting the chip (Fig. S16). The sample showed exactly the same behavior, which rules out the hypothesis of photo-induced cleaning of the surface from contamination. We have noticed that in both the experiments just described, mass 28 is increased when the light is on under stoichiometric H_2/O_2 mixture together with a small CO_2 ($m/z = 44$) evolution. Since the time evolution of mass 28 is different than the one of mass 44, we assigned this signal mainly to N_2 (instead of CO) and thus to photocorrosion of the surface of the catalysts. This attribution is also supported by the ratio of the measured mass 14 and 28 (equal to 0.15). Notice, however, that these signals are two orders of magnitude smaller than the water signal. This small but detectable photocorrosion is also present with the Pt sample when the back reaction experiment starts with O_2, but no evidence of photocorrosion has been seen during the photocatalytic water splitting experiments or with other samples.

4. Discussion

The trend of photocatalytic activities in Fig. 2 for the gas-phase water splitting reaction is in agreement with what has been reported for liquid phase [3,21]. In liquid-phase experiments, stoichiometric H_2 and O_2 production has been measured with GaN:ZnO loaded with Rh–Cr mixed oxide and core/shell cocatalysts, while in the reported gas-phase experiments, the ratio of H_2 and O_2 slightly exceeds the stoichiometric value. This behavior has been also reported and discussed in a previous publication about gas-phase water splitting with $Rh_{2-y}Cr_yO_3$/GaN:ZnO and could not be associated with any substantial amount of hydrocarbon contamination or H_2O_2 formation [20]. As shown in Fig. 2, overall photocatalytic water splitting was observed with all the samples loaded with cocatalysts but not with the GaN:ZnO alone. This fact shows

the importance of the cocatalyst in the photocatalytic production of H_2 and O_2 from pure water. The reason for this is that the cocatalyst improves catalytic kinetics at the surface and helps separating the photoelectrons from the photoholes, that otherwise would recombine. Following these considerations, one of the aims of this work is to obtain a better understanding of different cocatalysts and how their positive effect can be optimized. By comparing the different activities for photocatalytic overall water splitting, we can observe that there are marked differences between GaN:ZnO loaded with bare Pt and Rh and their modifications. Both Pt and Rh are known as good hydrogen evolution reaction (HER) catalysts, while the surface of GaN:ZnO acts as the oxygen evolution site (Fig. 1a). It is known by the experimental work of Trasatti for electrochemical hydrogen evolution [22] and by the theoretical study using DFT calculations of Nørskov et al. that Pt is a very good catalyst for HER [23]. The same holds for Rh. Even if the activity of Rh is lower than that of Pt, it is still one of the best catalysts for this reaction, as can be seen in the volcano plots obtained in the aforementioned works. On the other hand, Cr_2O_3 has not been reported to be a good HER catalyst. These considerations are not enough to explain the trend in Fig. 2, since the activity of both Pt and Rh is smaller than those of Cr_2O_3/Pt, Cr_2O_3/Rh, and $Rh_{2-y}Cr_yO_3$. However, we will show how the experimental results can be justified by the presence of O_2, formed by the splitting of water, close to the HER cocatalyst. This situation is different from the case of an electrochemical cell, where the HER and the oxygen evolution reaction (OER) occur in separated compartments. Instead in the system studied, H_2 and O_2 evolve in the same environment. If we consider the comparison between the noble metal and their core/shell modification shown in Fig. 5, we can see how the Cr_2O_3 shell has the simultaneous effect of suppressing the back reaction and enhancing the detected amount of H_2 and O_2. This is in agreement with what was found for the model electrodes, and explained by the fact that Cr_2O_3 can block O_2 from reaching the surface of the noble metal nanoparticle cocatalysts while H^+ can still get through. The latter can penetrate the shell, react with the photoelectrons on the noble metal surface, and pass back through the shell again as H_2, due to its smaller molecular radius compared to O_2. In this way, the oxygen reduction reaction (ORR):

$$4H^+ + 4e^- + O_2 \rightarrow 2H_2O \quad (2)$$

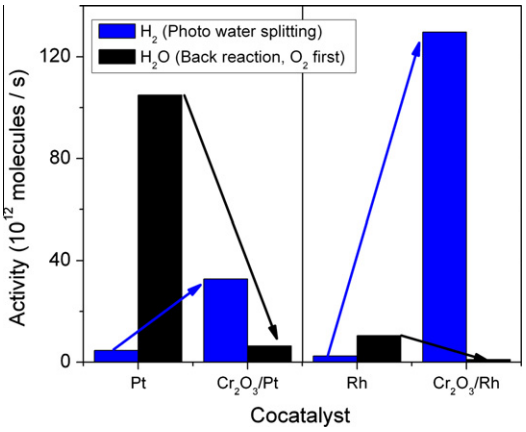

Fig. 5. Comparison between the two noble metals tested as cocatalysts and their core/shell modification. The cocatalysts were deposited on GaN:ZnO. In the figures, the initial hydrogen evolution rate for overall photocatalytic water splitting (blue) and the water evolution rate for the dark back reaction experiments starting with O_2 (black) are shown. The arrows further underline the opposite tendency between the H_2 detected in the water splitting experiments and the H_2O evolved in the back reaction. (For the interpretation of the references to color in this figure legend, the reader is referred to the web version of this article.)

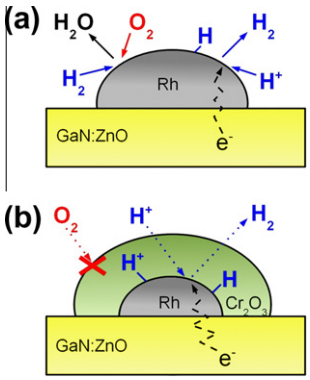

Fig. 6. Oxygen blocking by the proton- and hydrogen-permeable Cr_2O_3 shell. In the absence of Cr_2O_3, the O_2 can react on the Rh cocatalyst and recombine with the hydrogen to form water (water splitting back reaction) (a). In the case of Cr_2O_3/Rh cocatalyst, the shell prevents the O_2 to reach the Rh, while protons can penetrate the shell and react with the photoelectrons on the Rh core forming hydrogen (b).

as well as the catalytic reaction between H_2 and O_2 (reaction Fig. 1b) is strongly suppressed. So the Cr_2O_3 acts as an oxygen-blocking proton/hydrogen membrane (Fig. 6a and b). The fact that Pt and Rh show high activity for the back reaction is well known in fuel cell literature [24], where ORR is studied, and it is also illustrated in the volcano plot for ORR calculated using DFT by Nørskov et al. [25]. It can be seen from the comparison of the two volcano plots that even if the two noble metals, Pt especially, are very good for HER, they are also very good for ORR. So the trend shown in Fig. 2 is a trade-off between these two phenomena. If oxygen is able to reach the HER cocatalyst, this one needs to be a very bad ORR cocatalyst in order not to reduce it. It is very difficult to find a single material that has both these properties. It is probably a better approach to try and protect the HER catalyst with a membrane, like it has been done in the case with the Cr_2O_3 shell that separates it from the O_2 produced at the OER active sites.

The proposed explanation that the observed back reaction rates are the main cause of the deviation from the HER trend implies that the rate-determining step is the charge transfer at the cocatalyst molecules and not the one at the photocatalyst–cocatalyst (where possible different Schottky barriers can be thought to play a role). Indeed, Szklarczyk and Bockris have reported that the photocatalytic evolution of H_2 with a photocathode of p-InP coated with islets of different metals (Pb, Cd, Co, Au, Ni, Pt) correlates very well with the dark electrocatalytic evolution of H_2 from the bulk metal electrodes [26]. From this comparison, the authors conclude that the charge transfer at the photocatalyst–cocatalyst interface is not the step that determines the photoelectrochemical evolution of H_2 in the case of a semiconductor cover with metal islets. This conclusion is in agreement with the characteristic times for primary processes in TiO_2 photocatalysis reported by Fujishima et al. in a recent review [27]. From the comparison between the characteristic times, it is clear how in Pt-loaded TiO_2 the electron transfer from TiO_2 to the Pt clusters is much faster than the interfacial charge transfer to adsorbates.

The behavior of $Rh_{2-y}Cr_yO_3$ cocatalyst is more difficult to explain than the one of the core/shell cocatalysts. The experiments show that the chromia mixed with Rh is still preventing O_2 to be reduced. According to our previous study using XPS and XAFS, the valence state of Rh species in $Rh_{2-y}Cr_yO_3$ is trivalent, which remains unchanged even after water splitting reaction [28]. However, it is still not clear how the Rh species in the cocatalyst work during the working state of water splitting.

Comparing the results of the two kinds of back reaction experiments where the order of H_2 and O_2 introduction is changed, one can notice that they basically show the same trend: Pt has the

highest rate of back reaction, the back reaction rate from Cr_2O_3/Pt is reduced with respect to Pt, and the one from Cr_2O_3/Rh and $Rh_{2-y}Cr_yO_3$ is strongly suppressed with respect to the one of Rh. However, even if they present the same trend, there are some differences between the two kinds of back reaction experiments. In particular for Pt and Rh, the steady-state reaction rate reached when the sample is subject to an initial H_2 flow is lower in intensity than the one when O_2 is flown first. This difference could arise from different surface coverages of oxygen and hydrogen on the cocatalyst nanoparticles. Indeed, it is known that at low temperatures, as the one in our experiment, hydrogen has the effect of poisoning the surface due to the weak temperature dependence of its sticking coefficient with respect to the exponential temperature dependence of desorption. A hysteresis cycle with two different steady-state reaction rates has been reported for Pt, in agreement with our results [8,29]. The steady state reached after illumination in the case of Pt and Cr_2O_3/Pt can also be due to a different surface coverage, this time induced by the interaction of the adsorbates with the photoexcited carriers. Another difference that can be noticed comparing the two types of back reaction experiments is that the suppression of the back reaction due to the chromia shell seems to be stronger when the experiments start with O_2 instead of H_2. A possible explanation for this difference in behavior may be a partial reduction of the chromia under the initial hydrogen atmosphere. However, this case is less interesting than the one starting with oxygen since in typical water splitting experiments the catalyst is transferred from air to liquid water, so it is not subjected to a reducing hydrogen atmosphere. From Figs. 4 and 5, it is clear that the water formation rate is higher for the Cr_2O_3/Pt than for the Cr_2O_3/Rh, where it is basically negligible. This fact can likely be the cause for the higher net forward photocatalytic activity observed for the Cr_2O_3/Rh system compared to the Cr_2O_3/Pt system. Furthermore, this observation suggests that if Pt can somehow be protected more efficiently, then this system would have a higher activity, potentially even higher than protected Rh. This consideration agrees with the fact that the back reaction activity for the bare Pt is much higher than the one for the Rh, as expected from the ORR volcano plot, while their photocatalytic water splitting activity is comparable.

5. Conclusion

Gas-phase photocatalytic water splitting experiments show, in agreement with liquid-phase analogs, that $Rh_{2-y}Cr_yO_3$/GaN:ZnO and Cr_2O_3/Rh/GaN:ZnO have a superior activity for this reaction compared to Rh/GaN:ZnO, Pt/GaN:ZnO and Cr_2O_3/Pt/GaN:ZnO. The experiments also show that Cr_2O_3/Pt/GaN:ZnO has a higher activity than Pt/GaN:ZnO and Rh/GaN:ZnO. The results of the photocatalytic experiments find a correlation with the ones from the water splitting back reaction (stoichiometric H_2 oxidation). The sample with the Pt cocatalyst has the highest rate of back reaction and the Cr_2O_3 shell deposited on the Pt reduces this rate. In a similar way, the water formation rate for Cr_2O_3/Rh and $Rh_{2-y}Cr_yO_3$ is strongly suppressed and negligible compared to the one for Rh. The combination of the photocatalytic water splitting and its catalytic back reaction clearly shows the positive effect of the Cr_2O_3 shell in suppressing the water formation from H_2/O_2 back reaction, thereby enhancing the net production of H_2 and O_2 from water splitting.

Acknowledgments

Center for Individual Nanoparticle Functionality (CINF) is financed by the Danish National Research Foundation. This was also financed by the Research and Development in a New Interdisciplinary Field Based on Nanotechnology and Materials Science program of the Ministry of Education, Culture, Sports, Science and Technology (MEXT) of Japan, and The KAITEKI Institute, Inc. This project was further funded by the "Catalysis for Sustainable Energy" (CASE) research initiative, which is funded by the Danish Ministry of Science, Technology and Innovation.

Appendix A. Supplementary material

Supplementary data associated with this article can be found, in the online version, at http://dx.doi.org/10.1016/j.jcat.2012.03.021.

References

[1] A. Kudo, Y. Miseki, Chem. Soc. Rev. 38 (2009) 253.
[2] M.G. Walter, E.L. Warren, J.R. McKone, S.W. Boettcher, Q. Mi, E.A. Santori, N.S. Lewis, Chem. Rev. 110 (2010) 6446.
[3] K. Maeda, K. Teramura, D. Lu, N. Saito, Y. Inoue, K. Domen, Angew. Chem. Int. Ed. 45 (2006) 7806.
[4] K. Maeda, K. Domen, J. Phys. Chem. Lett. 1 (2010) 2655.
[5] D. Wang, A. Pierre, M.G. Kibria, K. Cui, X. Han, K.H. Bevan, H. Guo, S. Paradis, A.-R. Hakima, Z. Mi, Nano Lett. 11 (2011) 2353.
[6] M. Yoshida, K. Takanabe, K. Maeda, A. Ishikawa, J. Kubota, Y. Sakata, Y. Ikezawa, K. Domen, J. Phys. Chem. C 113 (2009) 10151.
[7] B. Hellsing, B. Kasemo, V.P. Zhdanov, J. Catal. 132 (1991) 210.
[8] E.M. Larsson, C. Langhammer, I. Zoric, B. Kasemo, Science 326 (2009) 1091.
[9] K. Maeda, T. Takata, M. Hara, N. Saito, Y. Inoue, H. Kobayashi, K. Domen, J. Am. Chem. Soc. 127 (2005) 8286.
[10] K. Maeda, K. Teramura, T. Takata, M. Hara, N. Saito, K. Toda, Y. Inoue, H. Kobayashi, K. Domen, J. Phys. Chem. B 109 (2005) 20504.
[11] K. Maeda, K. Teramura, K. Domen, J. Catal. 254 (2008) 198.
[12] K. Maeda, K. Domen, Chem. Mater. 22 (2010) 612.
[13] K. Maeda, K. Teramura, D. Lu, N. Saito, Y. Inoue, K. Domen, J. Phys. Chem. C 111 (2007) 7554.
[14] K. Maeda, K. Teramura, D. Lu, T. Takata, N. Saito, Y. Inoue, K. Domen, Nature 440 (2006) 295.
[15] K. Maeda, K. Teramura, D. Lu, T. Takata, N. Saito, Y. Inoue, K. Domen, J. Phys. Chem. B 110 (2006) 13753.
[16] T.R. Henriksen, J.L. Olsen, P.C.K. Vesborg, I. Chorkendorff, O. Hansen, Rev. Sci. Instrum. 80 (2009) 124101.
[17] P.C.K. Vesborg, J.L. Olsen, T.R. Henriksen, I. Chorkendorff, O. Hansen, Rev. Sci. Instrum. 81 (2010) 016111.
[18] P.C.K. Vesborg, J.L. Olsen, T.R. Henriksen, I. Chorkendorff, O. Hansen, Chem. Eng. J. 160 (2010) 738.
[19] P.C.K. Vesborg, S.-I. In, J.L. Olsen, T.R. Henriksen, B.L. Abrams, Y. Hou, A. Kleiman-Shwarsctein, O. Hansen, I. Chorkendorff, J. Phys. Chem. C 114 (2010) 11162.
[20] F. Dionigi, P.C.K. Vesborg, T. Pedersen, O. Hansen, S. Dahl, A. Xiong, K. Maeda, K. Domen, I. Chorkendorff, Energy Environ. Sci. 4 (2011) 2937.
[21] K. Maeda, K. Teramura, N. Saito, Y. Inoue, H. Kobayashi, K. Domen, Pure Appl. Chem. 78 (2006) 2267.
[22] S. Trasatti, J. Electroanal. Chem. 39 (1972) 163.
[23] J.K. Nørskov, T. Bligaard, A. Logadottir, J.R. Kitchin, J.G. Chen, S. Pandelov, U. Stimming, J. Electrochem. Soc. 152 (2005) J23.
[24] F.H.B. Lima, J. Zhang, M.H. Shao, K. Sasaki, M.B. Vukmirovic, E.A. Ticianelli, R.R. Adzic, J. Phys. Chem. C 111 (2007) 404.
[25] J.K. Nørskov, J. Rossmeisl, A. Logadottir, L. Lindqvist, J.R. Kitchin, T. Bligaard, H. Jonsson, J. Phys. Chem. B 108 (2004) 17886.
[26] M. Szklarczyk, J.O'M. Bockris, J. Phys. Chem. C 88 (1984) 5241.
[27] A. Fujishima, X. Zhang, D.A. Tryk, Surf. Sci. Rep. 63 (2008) 515.
[28] K. Maeda, K. Teramura, H. Masuda, T. Takata, N. Saito, Y. Inoue, K. Domen, J. Phys. Chem. B 110 (2006) 13107.
[29] V.P. Zhdanov, Surf. Sci. 296 (1993) 261.

Supplementary information

GaN:ZnO characterization

Fig. S1. Powder XRD pattern of GaN:ZnO showing hexagonal wurtzite phase.

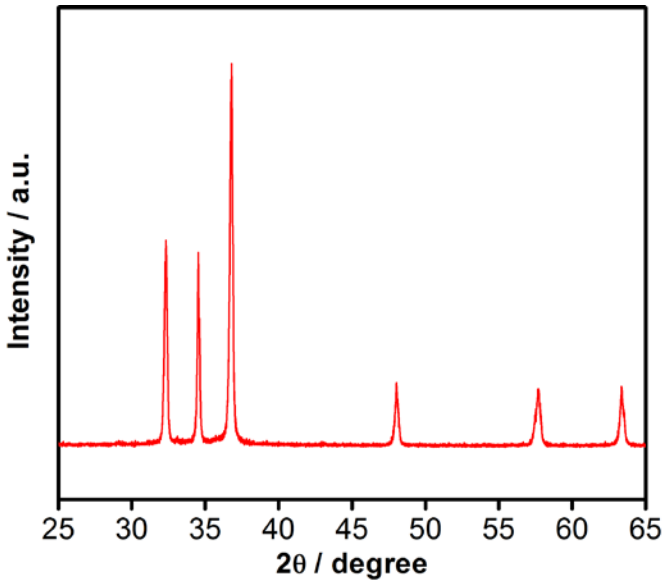

Fig. S2. SEM image of GaN:ZnO.

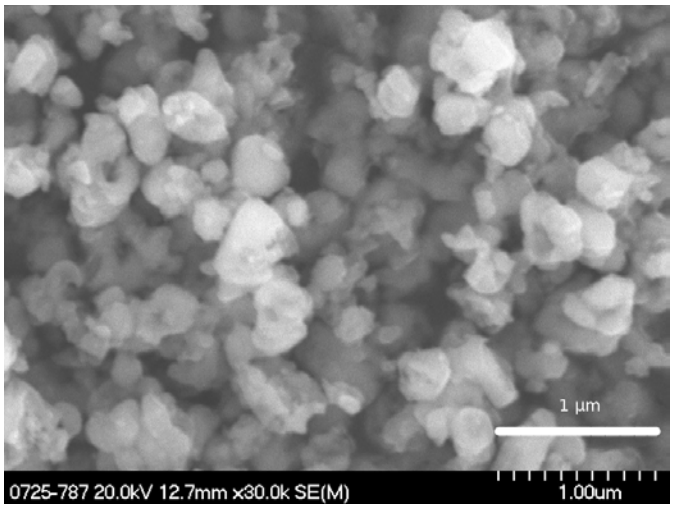

Fig. S3. UV visible diffuse reflectance spectra of GaN:ZnO.

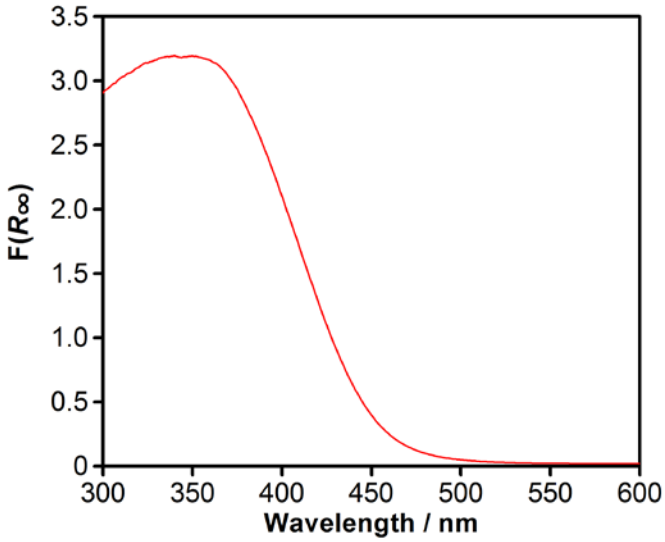

Water splitting back reaction starting with oxygen

Fig. S4. QMS current for H_2 (m/z = 2), O_2 (m/z = 32), H_2O (m/z = 18), He (m/z =4), CO_2 (m/z=44) and CO/N_2 (m/z=28) as a function of time for a water splitting back reaction experiment with GaN:ZnO. Initially the sample is exposed only to O_2 (1 ml/min) and He (15 ml/min). At ~90 min H_2 (2 ml/min) is dosed. The grey shaded area before and after the introduction of H_2 indicate time intervals when chopped light was on (3 light cycles of 180 s light on and 180 s light off, UV LED at λ ~ 367 nm and I ~ 460 mW/cm^2). The water signal has been fitted in the time interval before the introduction of H_2 and the fit extended to the following times (dashed red line).

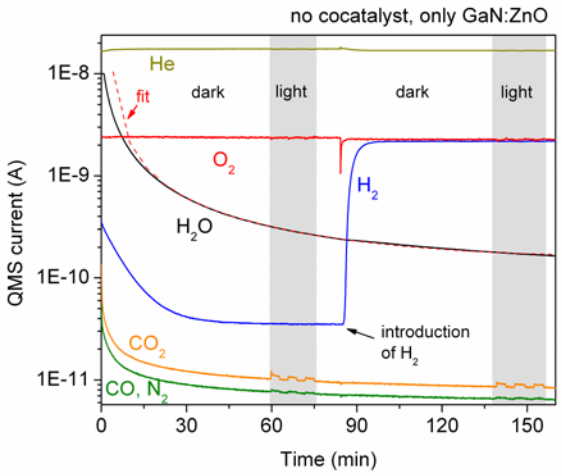

Fig. S5. QMS current for H_2 (m/z = 2), O_2 (m/z = 32), H_2O (m/z = 18), He (m/z =4), CO_2 (m/z=44) and CO/N_2 (m/z=28) as a function of time for a water splitting back reaction experiment with $Rh_{2-y}Cr_yO_3$/GaN:ZnO. Initially the sample is exposed only to O_2 (1 ml/min) and He (15 ml/min). At ~100 min H_2 (2 ml/min) is dosed. The grey shaded area indicate time intervals when chopped light was on (5 light cycles of 180 s light on and 180 s light off before the introduction of H_2 and 3 cycles after, UV LED at λ ~ 367 nm and I ~ 460 mW/cm^2). The water signal has been fitted in the time interval before the introduction of H_2 and the fit extended to the following times (dashed red line). Weak photocatalytic H_2 evolution is observed when light is incident on the sample and only O_2 and He is flown. It is possible that the H_2 comes from water splitting from some water molecules adsorbed on the surface since the sample before testing was exposed to air.

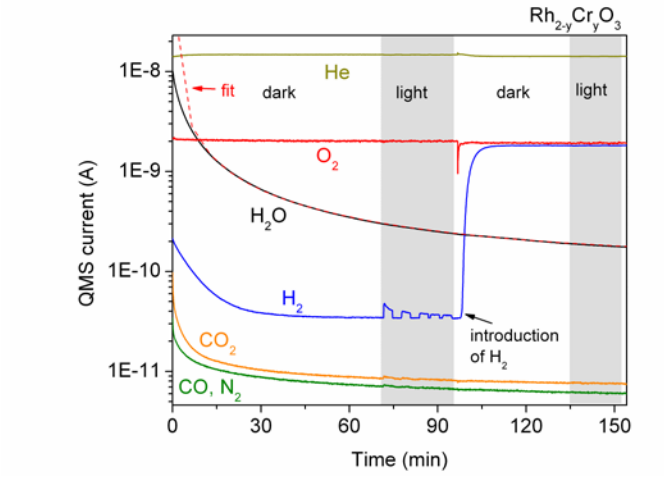

Fig. S6. QMS current for H_2 (m/z = 2), O_2 (m/z = 32), H_2O (m/z = 18), He (m/z =4), CO_2 (m/z=44) and CO/N_2 (m/z=28) as a function of time for a water splitting back reaction experiment with Rh/GaN:ZnO. Initially the sample is exposed only to O_2 (1 ml/min) and He (15 ml/min). At ~105 min H_2 (2 ml/min) is dosed. The grey shaded area before and after the introduction of H_2 indicate time intervals when chopped light was on (3 light cycles of 180 s light on and 180 s light off, UV LED at λ ~ 367 nm and I ~ 460 mW/cm^2). The water signal has been fitted in the time interval before the introduction of H_2 and the fit extended to the following times (dashed red line).

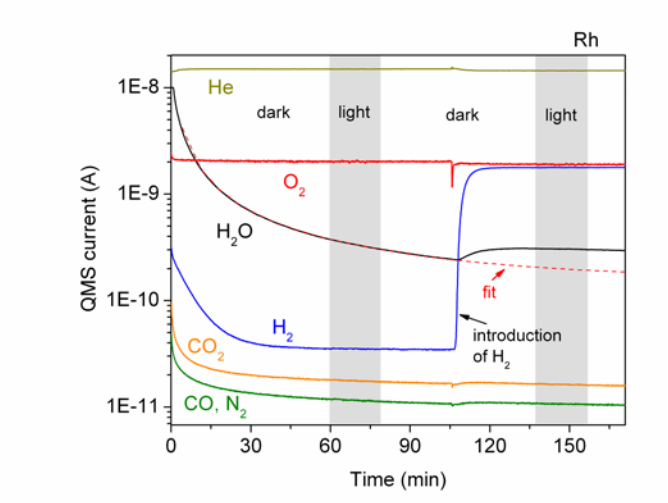

Fig. S7. QMS current for H_2 (m/z = 2), O_2 (m/z = 32), H_2O (m/z = 18), He (m/z =4), CO_2 (m/z=44) and CO/N_2 (m/z=28) as a function of time for a water splitting back reaction experiment with Cr_2O_3/Rh/GaN:ZnO. Initially the sample is exposed only to O_2 (1 ml/min) and He (15 ml/min). At ~100 min H_2 (2 ml/min) is dosed. The grey shaded area before and after the introduction of H_2 indicate time intervals when chopped light was on (3 light cycles of 180 s light on and 180 s light off, UV LED at λ ~ 367 nm and I ~ 460 mW/cm^2). The water signal has been fitted in the time interval before the introduction of H_2 and the fit extended to the following times (dashed red line).

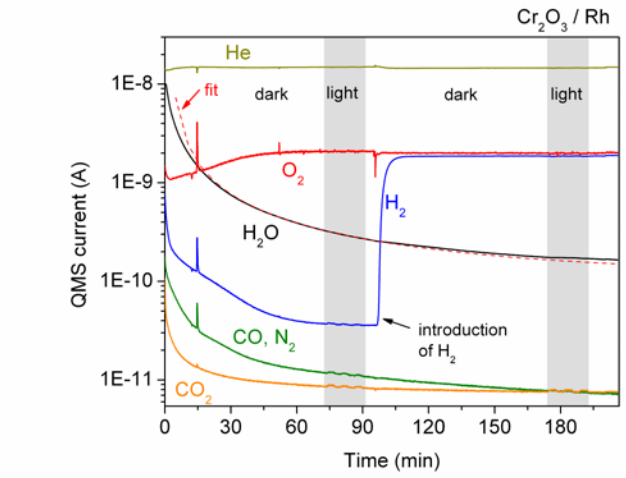

Fig. S8. QMS current for H_2 (m/z = 2), O_2 (m/z = 32), H_2O (m/z = 18), He (m/z =4), CO_2 (m/z=44) and CO/N_2 (m/z=28) as a function of time for a water splitting back reaction experiment with Pt/GaN:ZnO. Initially the sample is exposed only to O_2 (1 ml/min) and He (15 ml/min). At ~100 min H_2 (2 ml/min) is dosed. The grey shaded area indicate time intervals when chopped light was on (3 light cycles of 180 s light on and 180 s light off before the introduction of H_2 and 8 cycles after, UV LED at λ ~ 367 nm and I ~ 460 mW/cm^2). The water signal has been fitted in the time interval before the introduction of H_2 and the fit extended to the following times (dashed red line).

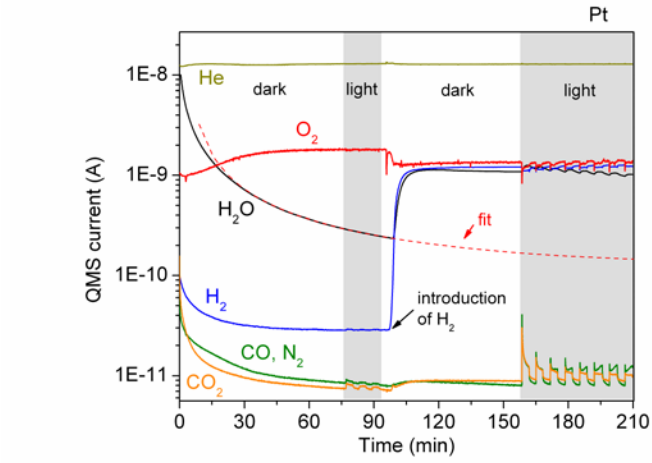

Fig. S9. QMS current for H_2 (m/z = 2), O_2 (m/z = 32), H_2O (m/z = 18), He (m/z =4), CO_2 (m/z=44) and CO/N_2 (m/z=28) as a function of time for a water splitting back reaction experiment with Cr_2O_3/Pt/GaN:ZnO. Initially the sample is exposed only to O_2 (1 ml/min) and He (15 ml/min). At ~80 min H_2 (2 ml/min) is dosed. The grey shaded area before and after the introduction of H_2 indicate time intervals when chopped light was on (3 light cycles of 180 s light on and 180 s light off, UV LED at λ ~ 367 nm and I ~ 460 mW/cm^2). The water signal has been fitted in the time interval before the introduction of H_2 and the fit extended to the following times (dashed red line).

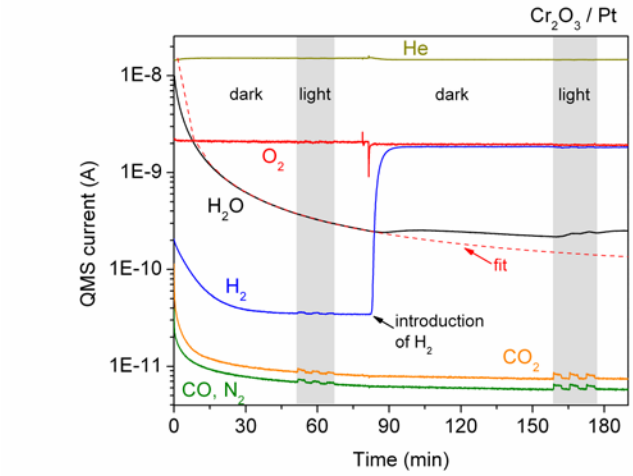

Water splitting back reaction starting with hydrogen

Fig. S10. QMS current for H_2 (m/z = 2), O_2 (m/z = 32), H_2O (m/z = 18), He (m/z =4), CO_2 (m/z=44) and CO/N_2 (m/z=28) as a function of time for a water splitting back reaction experiment with GaN:ZnO. Initially the sample is exposed only to H_2 (2 ml/min) and He (15 ml/min). At ~70 min O_2 (1 ml/min) is dosed. The grey shaded area before and after the introduction of O_2 indicate time intervals when chopped light was on (3 light cycles of 180 s light on and 180 s light off, UV LED at λ ~ 367 nm and I ~ 460 mW/cm^2). The water signal has been fitted in the time interval before the introduction of O_2 and the fit extended to the following times (dashed red line).

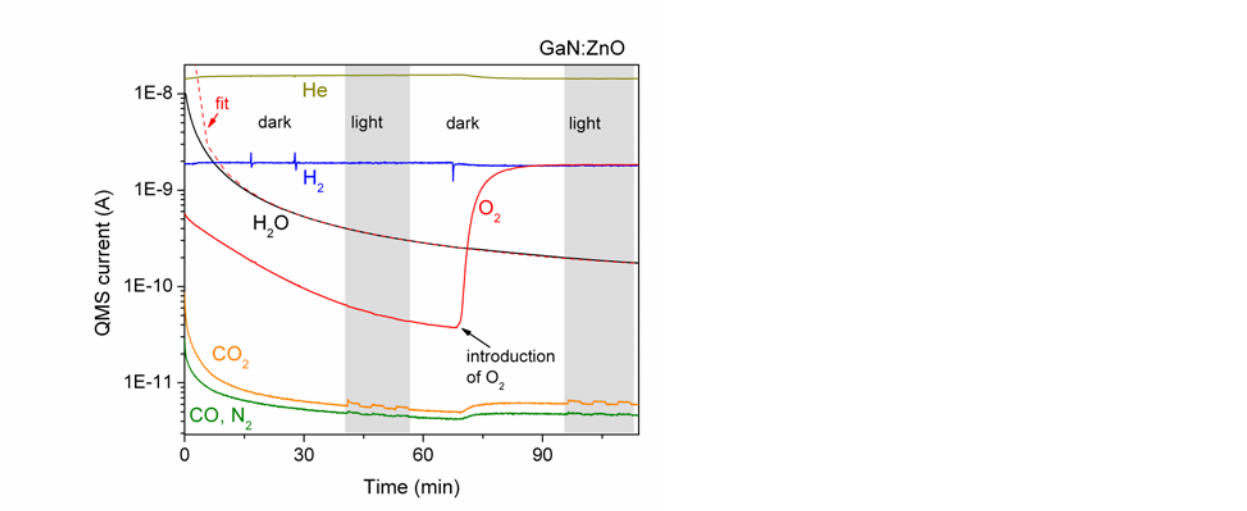

Fig. S11. QMS current for H_2 (m/z = 2), O_2 (m/z = 32), H_2O (m/z = 18), He (m/z =4), CO_2 (m/z=44) and CO/N_2 (m/z=28) as a function of time for a water splitting back reaction experiment with $Rh_{2-y}Cr_yO_3$/GaN:ZnO. Initially the sample is exposed only to H_2 (2 ml/min) and He (15 ml/min). At ~80 min O_2 (1 ml/min) is dosed. The grey shaded area before and after the introduction of O_2 indicate time intervals when chopped light was on (3 light cycles of 180 s light on and 180 s light off, UV LED at λ ~ 367 nm and I ~ 460 mW/cm^2). The water signal has been fitted in the time interval before the introduction of O_2 and the fit extended to the following times (dashed red line).

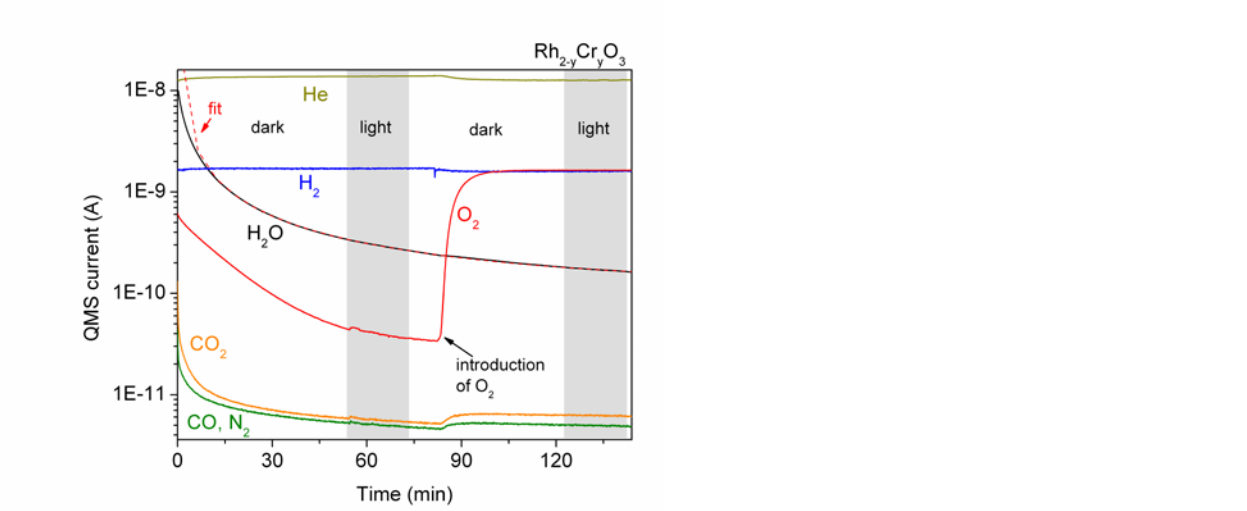

Fig. S12. QMS current for H_2 (m/z = 2), O_2 (m/z = 32), H_2O (m/z = 18), He (m/z =4), CO_2 (m/z=44) and CO/N_2 (m/z=28) as a function of time for a water splitting back reaction experiment with Rh /GaN:ZnO. Initially the sample is exposed only to H_2 (2 ml/min) and He (15 ml/min). At ~100 min O_2 (1 ml/min) is dosed. The grey shaded area before and after the introduction of O_2 indicate time intervals when chopped light was on (3 light cycles of 180 s light on and 180 s light off, UV LED at λ ~ 367 nm and I ~ 460 mW/cm^2). The water signal has been fitted in the time interval before the introduction of O_2 and the fit extended to the following times (dashed red line).

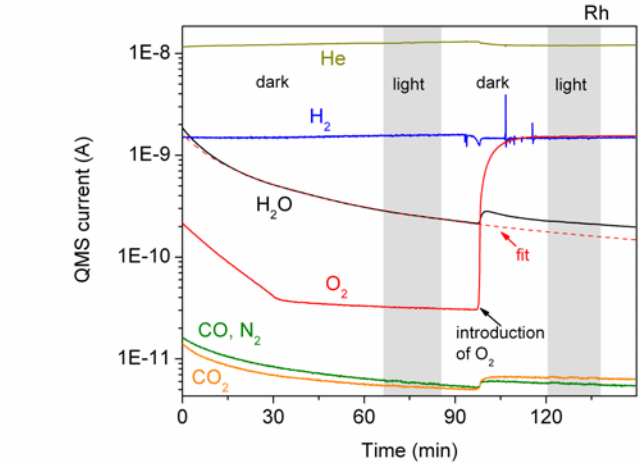

Fig. S13. QMS current for H_2 (m/z = 2), O_2 (m/z = 32), H_2O (m/z = 18), He (m/z =4), CO_2 (m/z=44) and CO/N_2 (m/z=28) as a function of time for a water splitting back reaction experiment with Cr_2O_3/Rh/GaN:ZnO. Initially the sample is exposed only to H_2 (2 ml/min) and He (15 ml/min). At ~100 min O_2 (1 ml/min) is dosed. The grey shaded area before and after the introduction of O_2 indicate time intervals when chopped light was on (3 light cycles of 180 s light on and 180 s light off, UV LED at λ ~ 367 nm and I ~ 460 mW/cm^2). The water signal has been fitted in the time interval before the introduction of O_2 and the fit extended to the following times (dashed red line).

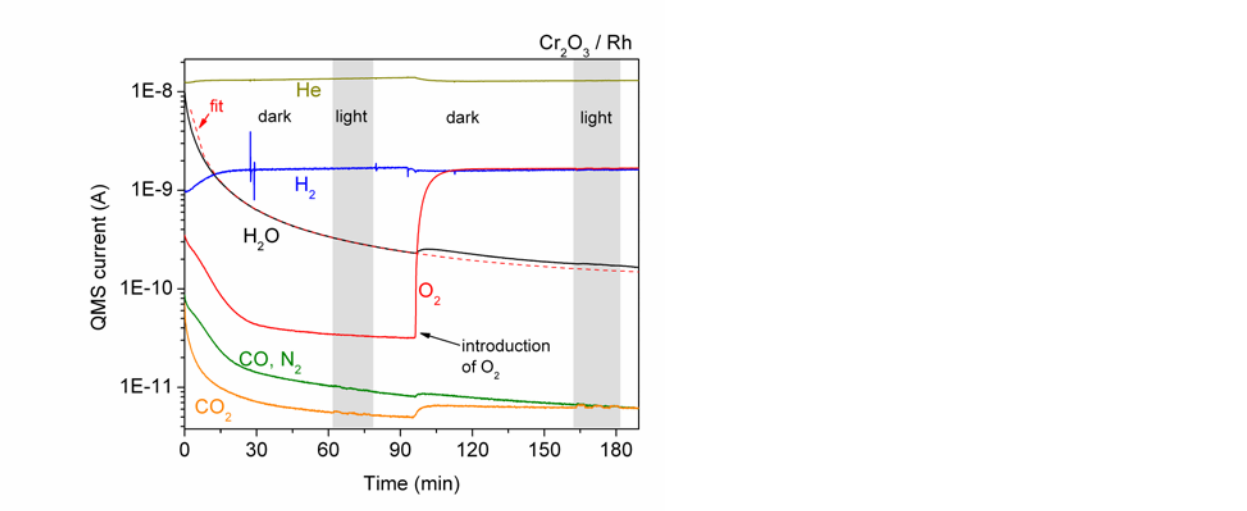

Fig. S14. QMS current for H_2 (m/z = 2), O_2 (m/z = 32), H_2O (m/z = 18), He (m/z =4), CO_2 (m/z=44) and CO/N_2 (m/z=28) as a function of time for a water splitting back reaction experiment with Pt /GaN:ZnO. Initially the sample is exposed only to H_2 (2 ml/min) and He (15 ml/min). At ~90 min O_2 (1 ml/min) is dosed. The grey shaded area before and after the introduction of O_2 indicate time intervals when chopped light was on (3 light cycles of 180 s light on and 180 s light off, UV LED at λ ~ 367 nm and I ~ 460 mW/cm^2). The water signal has been fitted in the time interval before the introduction of O_2 and the fit extended to the following times (dashed red line).

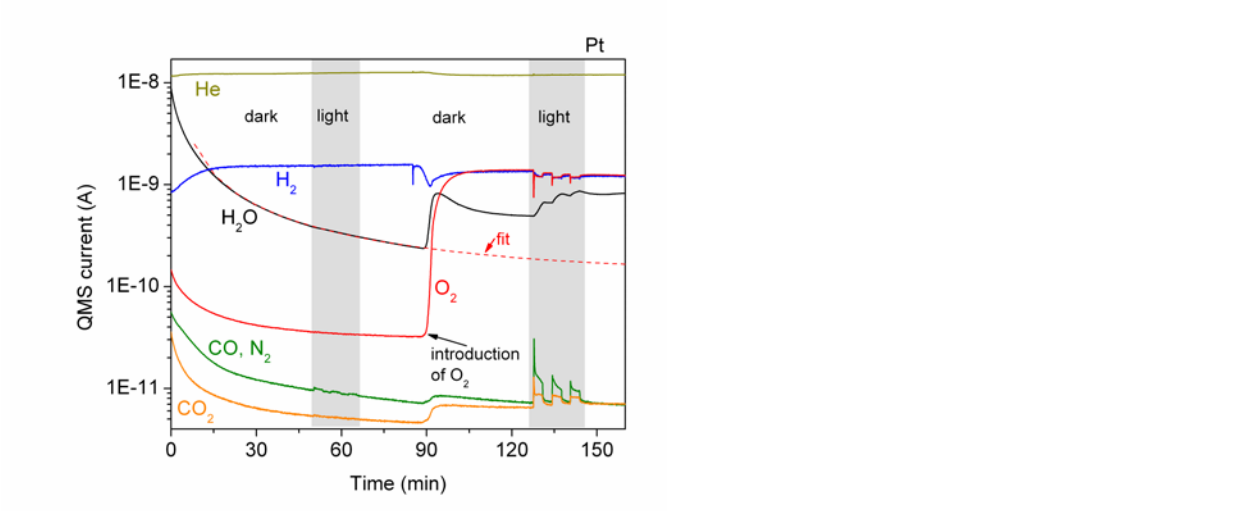

Fig. S15. QMS current for H_2 (m/z = 2), O_2 (m/z = 32), H_2O (m/z = 18), He (m/z =4), CO_2 (m/z=44) and CO/N_2 (m/z=28) as a function of time for a water splitting back reaction experiment with Cr_2O_3/Pt/GaN:ZnO. Initially the sample is exposed only to H_2 (2 ml/min) and He (15 ml/min). At ~90 min O_2 (1 ml/min) is dosed. The grey shaded area before and after the introduction of O_2 indicate time intervals when chopped light was on (3 light cycles of 180 s light on and 180 s light off, UV LED at λ ~ 367 nm and I ~ 460 mW/cm^2). The water signal has been fitted in the time interval before the introduction of O_2 and the fit extended to the following times (dashed red line).

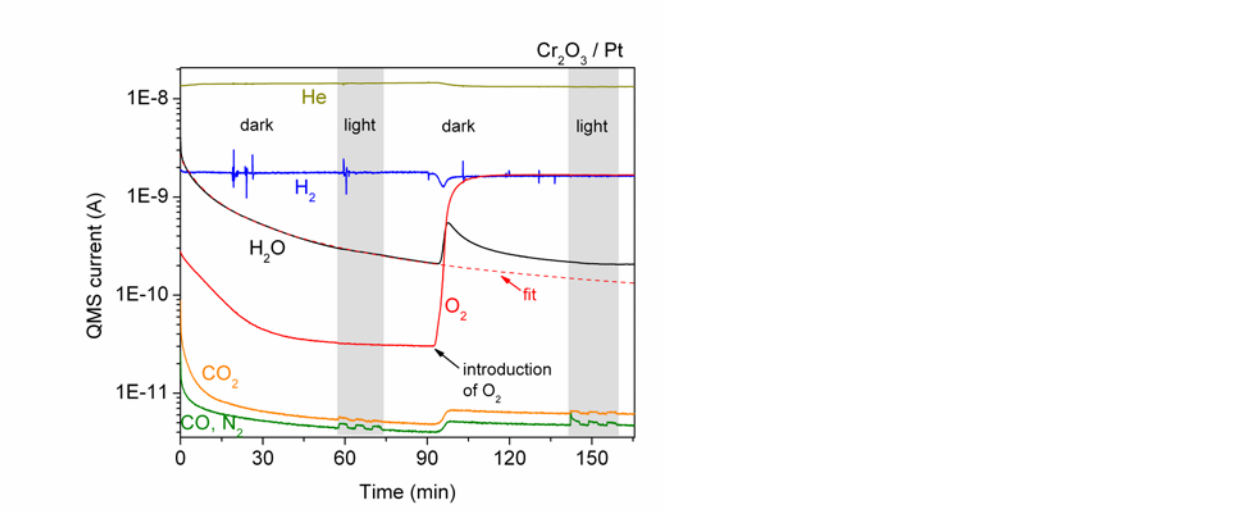

Fig. S16. QMS current for H_2 (m/z = 2), O_2 (m/z = 32), H_2O (m/z = 18), He (m/z =4), CO_2 (m/z=44) and CO/N_2 (m/z=28) as a function of time for a water splitting back reaction experiment with Pt/GaN:ZnO. Initially the sample is exposed only to H_2 (2 ml/min) and He (15 ml/min). At ~90 min O_2 (1 ml/min) is dosed. The O_2 flow is switched off at ~180 min and turned on again at ~225 min. The grey shaded area indicate time intervals when chopped light was on (3 light cycles of 180 s light on and 180 s light off at ~50 min, 3 cycles at ~125 min, 1 cycle at 168 min, 3 cycles at 250 min, UV LED at λ ~ 367 nm and I ~ 460 mW/cm^2). The water signal has been fitted in the time interval before the introduction of O_2 and the fit extended to the following times (dashed red line).

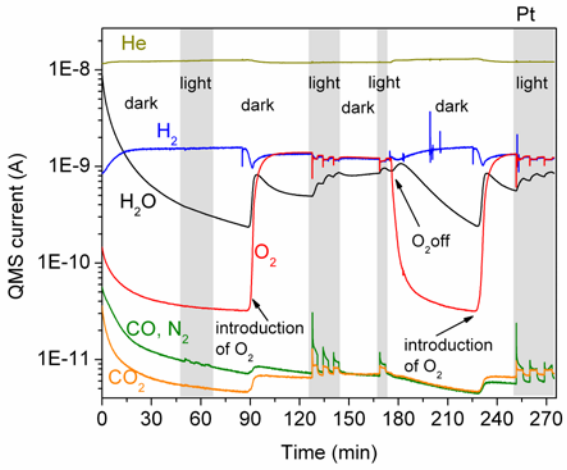
Pt
He
1E-8
1E-9
1E-10
1E-11
QMS current (A)
dark
light
dark
light
dark
light
dark
light
H2
H2O
O2
O2off
CO, N2
CO2
introduction of O2
introduction of O2
0
30
60
90
120
150
180
210
240
270
Time (min)

JOURNAL OF CHEMICAL EDUCATION

Laboratory Experiment

pubs.acs.org/jchemeduc

Electrochemical Hydrogen Evolution: Sabatier's Principle and the Volcano Plot

Anders B. Laursen,*[,†] Ana Sofia Varela,[†] Fabio Dionigi,[†] Hank Fanchiu,[‖] Chandler Miller,[‖] Ole L. Trinhammer,[§] Jan Rossmeisl,[‡] and Søren Dahl[†]

[†]CINF and [‡]CAMD, and [§]Department of Physics, Technical University of Denmark, 2800 Kgs. Lyngby, Denmark

[‖]Cal Energy Corps, University of California, Berkeley, California 94720, United States

Supporting Information

ABSTRACT: The electrochemical hydrogen evolution reaction (HER) is growing in significance as society begins to rely more on renewable energy sources such as wind and solar power. Thus, research on designing new, inexpensive, and abundant HER catalysts is important. Here, we describe how a simple experiment combined with results from density functional theory (DFT) can be used to introduce the Sabatier principle and its importance when designing new catalysts for the HER. We also describe the difference between reactivity and catalytic activity of solid surfaces and explain how DFT is used to predict new catalysts based on this. Suited for upper-level high school and first-year university students, this exercise involves using a basic two-cell electrochemical setup to test multiple electrode materials as catalysts at one applied potential, and then constructing a volcano curve with the resulting currents. The curve visually shows students that the best HER catalysts are characterized by an optimal hydrogen binding energy (reactivity), as stated by the Sabatier principle. In addition, students may use this volcano curve to predict the activity of an untested catalyst solely from the catalyst reactivity. This exercise circumvents the complexity of traditional experiments while it still demonstrates the trends of the HER volcano known from literature.

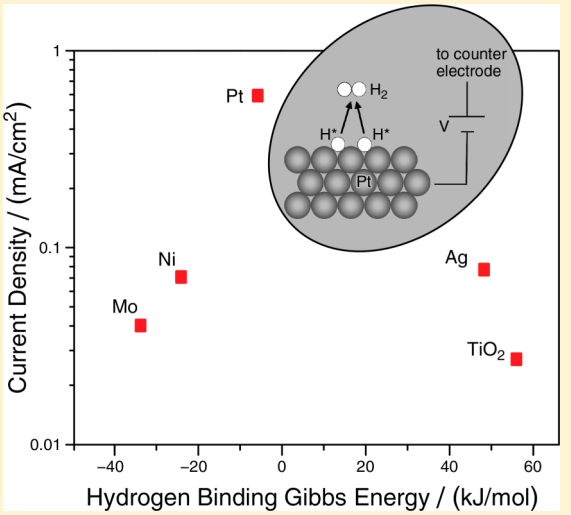

KEYWORDS: *High School/Introductory Chemistry, First-Year Undergraduate/General, Laboratory Instruction, Laboratory Instruction, Physical Chemistry, Hands-On Learning/Manipulatives, Catalysis, Electrolytic/Galvanic Cells/Potentials, Metals, Surface Science*

Electrochemistry gains ever more attention as the need for sustainable energy, often electrical, increases. It is therefore important to introduce students to electrocatalysis. A novel way of introducing students to the Sabatier principle (also see the laboratory exercise in ref 1) is presented and can be used to understand trends in catalytic activity in combination with density functional theory (DFT). This is achieved through a simple exercise using the classic electrochemical reaction for the hydrogen evolution reaction (HER) from water electrolysis:[2,3]

$$2H^+(aq) + 2e^- \leftrightarrow H_2(g) \quad (1)$$

Through this exercise, students test the HER activity of Mo, Ni, Ag, Pt, and TiO_2 and use these activities to understand the way in which DFT calculations and practical electrochemical experiments are used together to predict new catalysts for electrocatalytic reactions.

THEORY

It has been shown that the binding energy of the intermediates in a reaction determines how well a catalyst works. Generally, in catalysis, the unlikely situation of more than two molecules colliding simultaneously in the gas phase is circumvented by the binding of the reagents to a surface—thereby dividing the collisions into several sequential steps. That is, the first molecule will collide with the surface resulting in a bound intermediate and the second molecule then collides with the intermediate and reacts and so forth for additional steps. When this occurs, the reagents' internal bonds may be weakened due to the interaction with the catalyst, thereby lowering the energy barrier for a reaction. Hence, a catalyst should bind strongly to the reagents and intermediates so that they are likely to adsorb to the surface, allowing the reaction to occur. However, if the catalyst binds the intermediates or products too strongly, the products formed on the catalyst cannot desorb, leaving the catalyst inhibited. Thus, the Sabatier principle states that the optimal catalyst binds a key intermediate strongly enough so

dx.doi.org/10.1021/ed200818t | J. Chem. Educ. XXXX, XXX, XXX−XXX

that the reagents will likely bind and react, but weakly enough so that the product will easily desorb.

When the activity of catalyst materials are plotted versus reactivity, a peak-shaped curve known as the Sabatier plot or volcano curve is obtained.[4] This plot clearly illustrates the difference between the reactivity and activity of various catalysts. Reactivity, given by the binding energy of the key intermediate, indicates how much the catalyst interacts with the reactants—positive values indicate a weak interaction and vice versa. Reactivity is in this work obtained from DFT. Activity, which depends on reactivity, is the measured rate of the catalytic reaction and is usually described per unit surface area. In this work, the measured rate is the current per area of the electrode from electrochemical experiments, as this is a direct measure of the electrons consumed in the HER, and the data from the DFT calculations are provided to the students.

EXPERIMENT

Experimental Overview

In the experiments, the students use different materials for the working electrode and measure the current obtained at a given potential to assess the activity of the metal. The measurements are carried out in a simple two-electrode compartment setup described below.

Electrode Preparation

The following electrodes were used:

- Molybdenum foil (Sigma-Aldrich) 3 × 0.5 × 0.05 cm,
- Nickel foil (Goodfellow) 3 × 0.5 × 0.05 cm,
- Silver foil (Goodfellow) 1.5 × 0.5 × 0.05 cm,
- Titanium foil (Sigma-Aldrich) 3 × 0.5 × 0.025 cm,
- Platinum wire (Goodfellow) 1.5 (length) × 0.05 (diameter) cm,
- One carbon rod (Ted Pella, Inc.) 4 cm (length) × 0.25 in. (diameter).

To make the surface of the titanium foil into a thick oxide layer, the foil was sanded and then put in a muffle oven at 200 °C in air for 20 min. All electrodes were masked with nail polish to allow more accurate measurements of the exposed surface areas. To ensure that only a clean nonoxidized metal was exposed to the electrolyte, each electrode, *except* titanium, was sanded with the same type of fine-grade sandpaper on the area exposed to the electrolyte. All circuit contact points were sanded, regardless of the material. The sanding was done immediately prior to starting each measurement.

Experimental Procedure

The two-electrode setup consisted of two 100 mL beakers filled with 0.1 M H_2SO_4 as an electrolyte and connected by a KNO_3 salt bridge (Figure 1). One beaker contained the foil or wire to be measured (working electrode) and was connected to the negative outlet. Nitrogen or argon (AGA technical purity) was bubbled through the solution and the beaker covered with plastic film (household or Parafilm). This kept the beaker with the working electrode essentially free of oxygen, preventing the competing oxygen reduction reaction. The other beaker contained a graphite rod (counter electrode) and was connected to the positive outlet of the power supply. The electrodes were connected to two multimeters: one in parallel with the power supply to measure the applied potential and the other in series between the counter electrode and the power supply to measure the current.

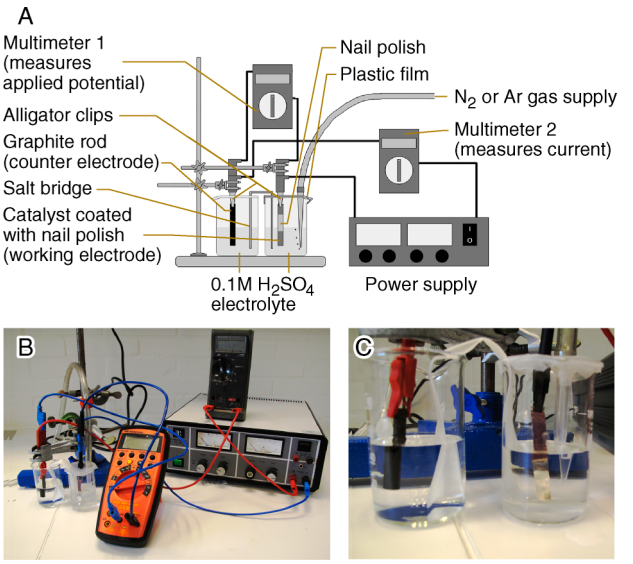

Figure 1. The experimental setup as a (A) schematic drawing, (B) photo of setup, and (C) close-up photo of the electrochemical cell.

With the power supply turned on, the potential was gradually raised to 3 V, held for 3 min, and then lowered to 1.7 V, at which point the current was recorded after the second decimal place had stabilized for 10 s. To ensure accuracy, both the current and potential were measured and adjusted to two decimal places precision, respectively. After the measurement, the working electrode was changed to a new material, and the procedures were repeated.

The precautions for the potentials were taken to ensure that the electrode surface was reduced to the metallic state and not an oxide and that any oxygen introduced by the electrode was completely removed by oxygen reduction. Furthermore, the potential was increased slowly to prevent overloading the multimeters.

Data Processing

Data processing was done by dividing each measured current by the surface area exposed to the electrolyte to obtain the current density. The electrode area is obtained by considering each foil as two rectangular surfaces or the wire as a cylinder. As all electrodes were sanded with the same grade sandpaper, each surface roughness was approximately the same. The resulting values were plotted on a base-10 logarithmic axis versus the corresponding DFT-calculated hydrogen binding Gibbs energy (linear axis) to obtain the Sabatier plot. The exercise required approximately 1 h and 45 min in total: 30 min for setup, 45 min for measurements, and 30 min for data treatment.

HAZARDS

As with all lab experiments, standard safety procedures should be obeyed. Goggles, gloves, and lab coats should be worn at all times. Concentrated sulfuric acid is corrosive and contact can cause severe damage to skin and eyes. The power supplies used here was limited to deliver no more than 10 V and 14 mW.

DENSITY FUNCTIONAL THEORY

To calculate the binding Gibbs energy of the key intermediate for any given reaction, one must know or assume the reaction mechanism. In the case of the HER, there are two proposed reaction mechanisms: the Volmer–Tafel mechanism

dx.doi.org/10.1021/ed200818t | J. Chem. Educ. XXXX, XXX, XXX–XXX

$$2(H^+(aq) + e^- + *) \leftrightarrow 2H* \leftrightarrow H_2(g) + 2* \quad (2)$$

and the Volmer–Heyrovsky mechanism

$$2H^+(aq) + e^- + * \leftrightarrow H* + H^+ \leftrightarrow H_2(g) + * \quad (3)$$

where the asterisk (*) indicates an empty active site and the H* indicates a hydrogen atom bound to the active site (Figure 2). Both reactions give the overall reaction shown in eq 1.

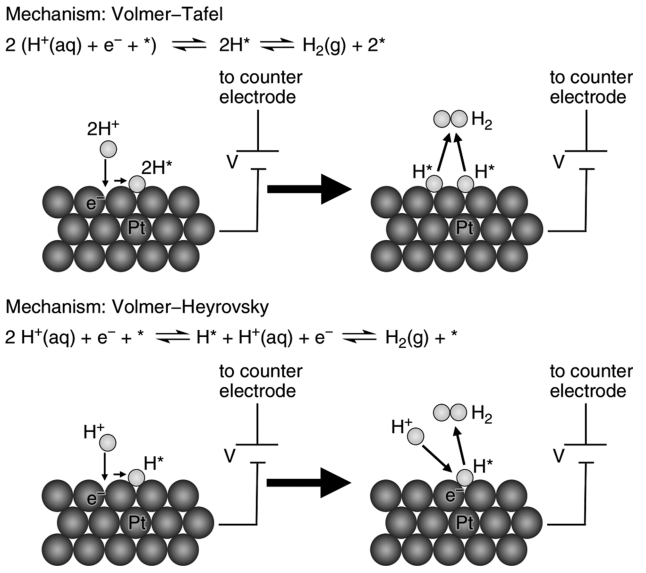

Figure 2. Two mechanisms for the HER reaction: the Volmer–Tafel mechanism and the Volmer–Heyrovsky mechanism on platinum surfaces. The asterisk (*) represents a free active site, whereas H* indicates that the hydrogen atom is bound to the active site.

Regardless of the mechanism, hydrogen is the only intermediate binding to the catalyst and DFT is used to calculate the binding Gibbs energy of hydrogen to the investigated catalysts. The DFT calculation uses the atomic position of the nuclei and the atomic charge to calculate the total energy of a system. In this case, the binding energy of the hydrogen atom to the surface is obtained by subtracting the energy of surface-bound hydrogen from the energy of the clean surface and half the energy of a free hydrogen molecule. Then, using simple estimates for entropy and zero-point energy, the Gibbs energy of binding hydrogen at standard conditions is obtained.[5] This simple method allows the screening of many catalyst systems for HER as for other catalytic reactions. The surfaces investigated in this study with their hydrogen binding Gibbs energies are listed in Table 1.

Table 1. DFT-Calculated Binding Energies for the Bonding of Hydrogen to the Surface of Molybdenum, Nickel, Silver, Titanium Dioxide, and Platinum

Catalyst Material	Binding Gibbs Energy/ (kJ/mol)	Experimental Current/ (mA/cm^2)
Mo	−33.8	0.025
Ni	−24.1	0.045
Ag	48.2	0.082
TiO_2	56.0	0.016
Pt	−5.8	0.500

RESULTS

The experiment gives a set of currents at a fixed potential for several electrode materials. The resulting current density is plotted versus the hydrogen binding Gibbs energy obtained using DFT calculation. Data generated from the instructor is shown in Figure 3A and by the students in Figure 3B.

As expected, the catalyst electrodes lie on a volcano curve when plotted against the hydrogen bonding Gibbs energies, obtained from theoretical calculations.[6] The peak of the volcano is close to the hydrogen binding Gibbs energy ΔG_H = 0 kJ/mol, in accordance with predictions from literature.[6,7] Furthermore, platinum is located near the top, as it is the best material known for the HER. This illustrates that our simple experimental setup gives the activity behavior expected from more detailed studies.[8]

It should be noted that the potential for this comparison is not chosen arbitrarily. Using lower potentials than the one stated results in currents that are too small for precise measurement in this setup. By contrast, using larger potentials causes the activity of the electrode to be limited by the diffusion of protons to, and gas away from, the electrode. Unavoidable electrical resistances in the circuit will also influence the result if the measurements are done at larger currents.

In Figure 3B, the data obtained from a group of students are plotted versus the hydrogen binding energy from Table 1. It was observed that some students sanded the TiO_2 electrode surface, thereby removing the oxide layer and exposing the pure metallic titanium. Some students also did not sand the electrode contact point. Both gave rise to erroneous results (Not shown in Figure 3B). Additionally, one group experienced decreased activity, likely due to the electrode oxidizing in the electrolyte. It is therefore emphasized that the students should polish the electrodes immediately before submerging them into the electrolyte and that the current is recorded after the second decimal place of the current measurement stabilizes. Usual student data varied with around 6–69% from the data shown here. However, the discrepancy does not significantly affect the logarithmic trends of the Sabatier plot and is thus an indication of the robustness of the experimental procedure.

DISCUSSION

Electrolysis is a well-known method for producing hydrogen from water using electrical energy, and is expected to gain more importance in the future when we have to rely more on renewable energy. The HER is the cathodic half-reaction occurring during electrolysis[9] and is well understood in terms of trends in activity. From the previously stated reaction schemes, eqs 2 and 3, for catalytic hydrogen production, it can be concluded that hydrogen bound to the electrode surface is a key intermediate, regardless which mechanism applies. Hence, this is the key intermediate binding energy calculated in this study, as well as in literature in general.

In literature, one may find Sabatier curves for the HER where the exchange current density is plotted as a function of hydrogen's binding energy.[5,10] However, the measurement of the exchange current density is cumbersome and the concept is above the introductory level intended here. Figure 3 shows that the obtained experimental results also produce a volcano curve similar to that observed in literature, signifying that this simple exercise gives reasonably accurate results. The advantage of this experiment is that, through a simple exercise, students are able to make Sabatier plots and predict the peak to be at least close

dx.doi.org/10.1021/ed200818t | J. Chem. Educ. XXXX, XXX, XXX–XXX

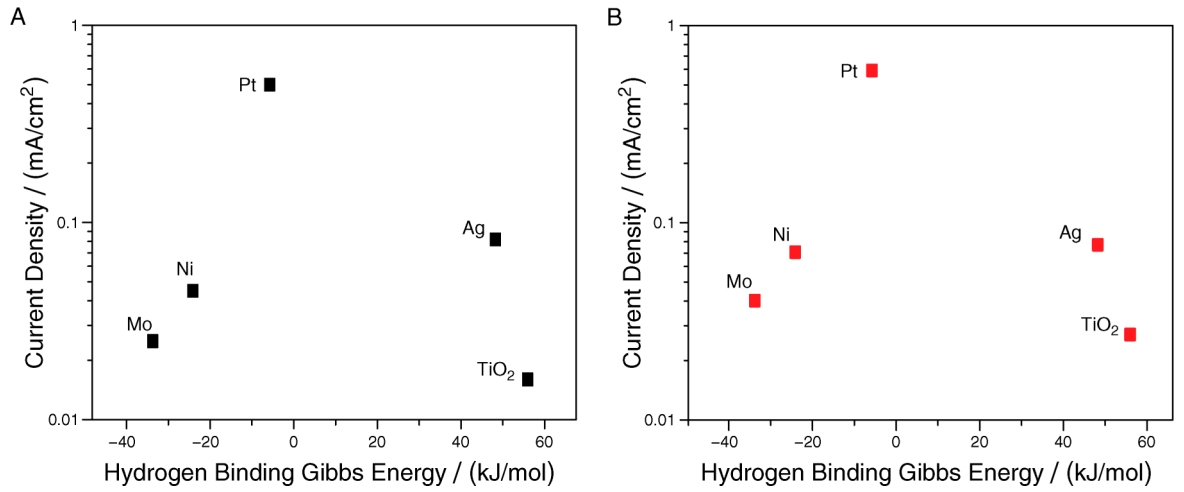

Figure 3. Sabatier plot of the activity of the measured catalysts (A) by the instructors and (B) by students versus the reactivity described by the DFT calculated hydrogen binding energy. Potential: 1.7 V.

to ΔG_H = 0 kJ/mol, which according to previous DFT studies is the top of the volcano.[5,10]

In addition, this experiment effectively demonstrates the difference in electrocatalytic activity obtained using different metals, thereby revealing the reason why platinum is so commonly used in electrolysis units. A discussion with the students on what criteria a catalyst should fulfill is encouraged. Factors such as cost, activity, abundance, and toxicity should be noted.

To demonstrate how the volcano may be used, students were asked to locate the top of the volcano by linear regression, using the measurements for molybdenum and nickel to obtain the left side and silver and titanium dioxide to obtain the right side. Figure 4 shows the resulting volcanoes for the instructor

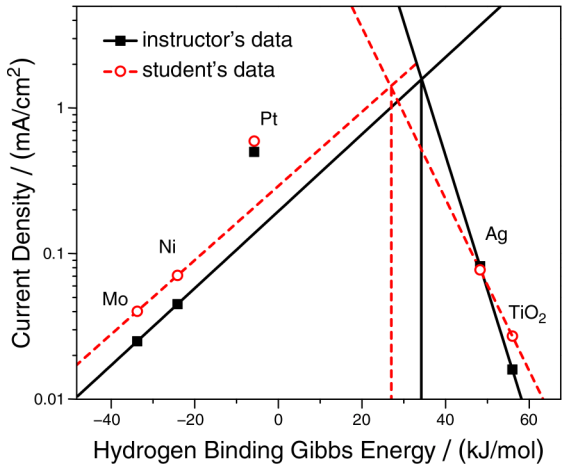

Figure 4. Results of predicting the volcano top by linear regression for the instructor data (square) and for the student data (circle). Potential: 1.7 V.

data and for student data. The two predictions fall within 40 kJ/mol from the known peak at 0 kJ/mol. Even though the prediction is not 0 kJ/mol, it is rare that a perfect volcano is found for any Sabatier plot and even rarer that it holds for such a simple experimental setup. This is what makes this experiment a powerful demonstration of how theory and experiments may be used together.

EXPERIMENTAL VARIATIONS

As a variation of this experiment, students can be suggested to test only the Mo, Ni, Ag, and TiO_2 electrodes and to predict the activity of Pt when given the corresponding hydrogen binding energy. The instructor should then measure the activity of Pt as a demonstration, and students should discuss how the measurement compares with their predictions. This exercise would allow students to understand the predicting power of the Sabatier plot. In addition, there would be a decrease in cost, as only one Pt electrode is needed.

Another experiment could be to measure the potential needed to obtain a current density of approximately 2 mA/cm^2. This resembles a working electrolysis unit more closely, as the current is constant and the potential varied. A volcano is also obtained in this case, when plotting the potential on the logarithmic y axis versus the hydrogen Gibbs binding energy. This affords an understanding of how the electrode material greatly affects the potential and energy required to drive the hydrogen production. The difficulty is that students should know the electrode area before measuring to calculate the actual current they need.

CONCLUSION

A simple and inexpensive way of allowing students to have hands-on experience with electrochemical measurements has been devised. Not only does the exercise demonstrate the Sabatier principle through experiments and theoretical calculations, it also shows how the latter is translated into a Sabatier plot. Experimenting with cost-effective and non-hazardous materials such as Ni, Mo, Ag, and TiO_2, students can understand the predictive power of DFT calculations using the Sabatier plot. In addition, the experiment is easy to conduct and requires minimal equipment and preparation. A group of 9th grade students successfully completed and understood the exercise. However, for full benefit, this exercise is recommended for upper-level high school students and undergraduate students.

ASSOCIATED CONTENT

Supporting Information

Notes for the instructor and student instructions. This material is available via the Internet at http://pubs.acs.org.

dx.doi.org/10.1021/ed200818t | J. Chem. Educ. XXXX, XXX, XXX−XXX

AUTHOR INFORMATION

Corresponding Author

*E-mail: ablaursen.chemistry@gmail.com.

Notes

The authors declare no competing financial interest.

ACKNOWLEDGMENTS

We gratefully acknowledge the Danish Ministry of Science for funding the CAtalysis for Sustainable Energy (CASE) initiative and Mårten Björketun for the DFT calculations.

REFERENCES

(1) Laursen, A. B.; Man, I. C.; Trinhammer, O. L.; Rossmeisl, J.; Dahl, S. *J. Chem. Educ.* **2011**, *88*, 1711−1715.
(2) Eberhardt, W. H. *J. Chem. Educ.* **1927**, *4*, A591.
(3) Heidman, S. *J. Chem. Educ.* **1986**, *63*, 809−810.
(4) Bligaard, T.; Nørskov, J. K.; Dahl, S.; Matthiesen, J.; Christensen, C. H.; Sehested, J. *J. Catal.* **2004**, *224*, 206−217.
(5) Nørskov, J. K.; Bligaard, T.; Rossmeisl, J.; Christensen, C. H. *Nat. Chem* **2009**, *1*, 37−46.
(6) Nørskov, J. K.; Bligaard, T.; Logadottir, A.; Kitchin, J. R.; Chen, J. G.; Pandelov, S.; Stimming, U. *J. Electrochem. Soc.* **2005**, *152*, J23−J26.
(7) Parsons, R. *Trans. Faraday Soc.* **1958**, *54*, 1052−1063.
(8) Trasatti, S. *J. Electroanal. Chem.* **1972**, *39*, 163−184.
(9) While the hydrogen evolution reaction is taking place at the cathode, an oxidation reaction is occurring at the anode. If we consider that the process taking place is the water electrolysis, the expected anodic reaction is oxygen evolution reaction (OER):

$$2H_2O \rightarrow O_2 + 4H^+ + 4e^-$$

This reaction generates the protons used in the cathode for the HER and completes the water splinting into hydrogen and oxygen. In this case, we can consider that the overall process is

$$2H_2O \rightarrow H_2 + O_2$$

However, there is also the possibility that the carbon of the counter electrode is being oxidized evolving CO_2 instead of O_2. This will occur following the equation:

$$C + 2H_2O \rightarrow CO_2 + 4H^+ + 4e^-$$

Here, as in the case of OER, protons are formed too, while the split water is used to slowly oxidize the graphite electrode.
(10) Skulason, E.; Tripkovic, V.; Bjorketun, M. E.; Gudmundsdottir, S.; Karlberg, G.; Rossmeisl, J.; Bligaard, T.; Jonsson, H.; Nørskov, J. K. *J. Phys. Chem. C* **2010**, *114*, 18182−18197.